Effect of Support Compliance on the Resonant Behavior of Microcantilever-Based Sensors in Viscous Fluids

Rabin Maharjan
Marquette University

Recommended Citation

Maharjan, Rabin, "Effect of Support Compliance on the Resonant Behavior of Microcantilever-Based Sensors in Viscous Fluids" (2013). *Dissertations (1934 -)*. 275.
https://epublications.marquette.edu/dissertations_mu/275

EFFECT OF SUPPORT COMPLIANCE ON THE RESONANT BEHAVIOR OF MICROCANTILEVER-BASED SENSORS IN VISCOUS FLUIDS

by

Rabin Maharjan, B.E., M.S.

A Dissertation submitted to the Faculty of the Graduate School,
Marquette University,
in Partial Fulfillment of the Requirements for
the Degree of Doctor of Philosophy

Milwaukee, Wisconsin

May 2013

ABSTRACT

EFFECT OF SUPPORT COMPLIANCE ON THE RESONANT BEHAVIOR OF MICROCANTILEVER-BASED SENSORS IN VISCOUS FLUIDS

Rabin Maharjan, B.E., M.S.

Marquette University, 2013

Resonant microcantilevers are often considered for use in chemical sensing and biosensing applications. However, when excited in the conventional transverse flexural mode, their performance in liquids is severely compromised. Theoretical and experimental studies have shown that the detrimental effects of the liquid may be mitigated by operating the microcantilever in lateral flexure, especially for microbeams having smaller length-to-width (L/b) ratios. However, for these most promising geometries the predictions of existing models tend to diverge from experimental data for resonant frequency (f_{res}) and quality factor (Q). A likely reason for these discrepancies is support compliance, which has been neglected in existing models. Thus, the derivation of an analytical model for the lateral-mode dynamic response of a microcantilever in a viscous fluid, including the effects of support compliance, is warranted and is the focus of this dissertation.

Analytical solutions for natural frequency and Q are first obtained for the free-vibration case, followed by solutions for the forced-vibration response when the cantilever is excited by an imposed harmonic relative rotation near the support (simulating electrothermal actuation). Values of f_{res} and Q are extracted from the response spectra for the tip deflection and the bending strain near the support. The support compliance (required as model input) is analytically related to device dimensions by employing dimensional analysis and 3-D FEA. The analytical results for the resonant characteristics are also related to sensor performance metrics (sensitivity and limit of detection), thus permitting one to exploit the potential of lateral-mode microcantilever-based liquid-phase sensors. The impact of support compliance, fluid resistance, and beam dimensions on the free- and forced-vibration response are explored, as are the differences associated with the two output signals. Comparisons of results with experimental data show a marked improvement over the previous rigid-support models for smaller L/b values. For the practical ranges of parameters considered the model indicates that, at smaller L/b values, support compliance may reduce Q by up to ~14% and f_{res} and mass sensitivity (S_m) by up to ~21%. Conversely, for L/b>15 the support compliance effects are no more than 2% on Q and 4% on f_{res} and S_m.

ACKNOWLEDGMENTS

Rabin Maharjan, B.E., M.S.

This dissertation has been made possible with the guidance, help, patience, and support of many individuals. I owe my deepest gratitude to them all who in one way or another contributed to the completion of this work.

I would like to sincerely thank my advisor, Dr. Stephen Heinrich, for his guidance, instruction, understanding, patience, encouragement, and providing me with excellent and flexible atmosphere for research work. I am amazed by his dedication, motivation, thoroughness, diligence, and relentless pursuit of excellence which has left a great impression on my heart and mind. I would also like to thank him for always being there for me through the toughest and the happiest time in my life.

I would like to extend my thanks to my dissertation committee members, Dr. Isabelle Dufour, Dr. Christopher Foley, Dr. Fabien Josse, and Dr. Nicholas Nigro. I am privileged to have worked with this excellent interdisciplinary team of researchers. This work has been made much better because of their thoughtful observations, suggestions and recommendations. I am also grateful to Dr. Oliver Brand and Dr. Luke A. Beardslee for sharing experimental data generated at Georgia Tech as part of the broader research program within which the dissertation project was executed.

I would like to thank my parents Macha Kaji and Dash Maya Maharjan, my elder sister Mandira Maharjan and my younger brother Nabin Maharjan for their love, support and encouragement. It must have been difficult for them to let their loved one go nearly eight thousands miles away from home to pursue his goal.

I would also like to thank my lovely wife, Reena, for believing in me, being patient with me, and encouraging and motivating me throughout this tough academic journey. I also thank her for standing by me through the good times and the bad times. I also must thank her for being a great mom and taking good care of our son while I was busy writing the dissertation.

Finally, I must thank my son, Lakas, who was born a few months before this dissertation was completed. He does not know why his father was not often there playing with him and must have missed me, but he always greeted me with an innocent smile when I came home from school. His smile made me forget all the stresses of the dissertation. A mere thank you is not enough for him. I am sorry, my son, for not being able to spend more time with you.

TABLE OF CONTENTS

LIST OF TABLES

LIST OF FIGURES

NOMENCLATURE

Symbols:

A_i = coefficients on the $\phi(\xi)$ equation;

b = width of rectangular beam cross-section (dimension along y-axis);

C_A = the ambient concentration of analyte;

$C(\ )$ = cosh( );

$c(\ )$ = cos( );

$\bar{c}_f$ = effective fluid damping coefficient per unit length;

$\bar{c} = b/2$ = distance from the neutral axis to the extreme fibers;

DMF_{tip} = dynamic magnification factor based on tip displacement;

d = decay parameter;

$\bar{d} \equiv \dfrac{d}{\omega_0}$ = dimensionless decay parameter;

E = Young's modulus of beam material along the x-direction;

$E_{eff.}$ = effective Young's modulus of cantilever considering coating layers;

f_{res} = resonant frequency [Hz];

$f_I(x,t)$ = inertial force at position x at time t;

h = thickness of rectangular beam cross-section (dimension along z-axis);

h_{nom} = nominal thickness of microcantilever specimen set;

h_{Si} = average silicon thickness of microcantilever specimen set;

$h_{pas.}$ = total thickness of passivation layer on microcantilever;

h_t = average total thickness of microcantilever specimen set;

I = second moment of area (moment of inertia) of beam cross-section about strong axis of bending;

i = imaginary unit, $\sqrt{-1}$;

K = partition coefficient of the particular coating/analyte combination and the particular operational medium;

k = rotational stiffness of support;

$\bar{k} \equiv \frac{kL}{EI}$ = dimensionless rotational stiffness of support;

L = length of beam (dimension along x-axis);

LOD = limit of detection;

L_0 = characteristic material length (constant for a given fluid and beam material);

M = bending moment applied over the end cross-section of beam in static 3-D finite-element modeling for determination of support stiffness;

$M(x,t)$ = bending moment in vibrating cantilever at position x at time t;

$\bar{m}_b$ = mass of beam per unit length;

$\bar{m}_f$ = effective fluid mass per unit length;

n = mode number;

P = pressure;

$p(x,t) = P(x)e^{i\omega t}$ = applied harmonic distributed force per unit length;

$P(x)$ = amplitude of applied distributed force per unit length;

Q = quality factor associated with viscous losses in surrounding fluid;

Q_n = quality factor associated with viscous losses in surrounding fluid for nth mode;

Q_1 = quality factor associated with viscous losses in surrounding fluid for first mode/ resonant peak;

$S(\ )$ = sinh( );

S_m = mass sensitivity;

S_c = chemical sensitivity;

$s(\ )$ = sin( );

t = time coordinate;

U_0 = amplitude of plate excitation velocity in *x*-direction;

u_x = displacement along *x*-axis in 3-D finite element model;

u_y = displacement along *y*-axis in 3-D finite element model;

u_z = displacement along *z*-axis in 3-D finite element model;

$\vec{u}_f$ = velocity field of the fluid;

$u_{x,plate}$ = velocity of plate along *x*-axis;

$u_{x,f}$ = fluid velocity along *x*-axis;

$u_{y,f}$ = fluid velocity along *y*-axis;

$u_{z,f}$ = fluid velocity along *z*-axis;

V_c = the volume of the chemically sensitive layer;

$V(x,t)$ = transverse shear force in beam at position *x* at time *t*;

W = work done by the bending stress σ_x at the beam-support interface;

W_{FEA} = work done by the bending stress σ_x at beam support interface calculated from finite element analysis;

x = spatial coordinate along the longitudinal (length) direction of the beam;

$\bar{x}$ = small distance from support to the point of application of the imposed rotation associated with the heating resistors;

y = spatial coordinate along the lateral (width) direction of the beam;

$y(x,t)$ = lateral deflection of beam at position x at time t;

$\bar{y}(\xi,\tau) \equiv \frac{y}{L}$ = dimensionless deflection of beam at dimensionless position ξ and dimensionless time τ;

z = spatial coordinate along the out-of-plane (thickness) direction of the beam;

Δf_{noise} = frequency noise of the system;

ρ_b = mass density of beam material;

ρ_f = mass density of fluid;

$\lambda_1 \equiv 1.875104$ = a constant associated with the mode-1 eigenvalue of a cantilever in vacuum;

ω = natural circular frequency (rad/s) in the presence of fluid in the case of free vibration; circular frequency of harmonic excitation in the case of forced vibration;

ω_0 = the natural circular frequency of the first lateral mode in vacuum for a perfectly clamped cantilever beam;

$\bar{\omega} \equiv \dfrac{\omega}{\omega_0}$ = dimensionless frequency;

$\bar{\omega}_{1,vac}$ = dimensionless first lateral-mode natural frequency in vacuum for a cantilever with compliant support;

$\Omega \equiv \omega + id$ = complex natural frequency;

$\bar{\Omega} \equiv \dfrac{\Omega}{\omega_0}$ = dimensionless complex natural frequency;

$\zeta \equiv \left[\dfrac{48\eta^2 \rho_f{}^2}{E \rho_f{}^3}\right]^{1/4} \dfrac{L}{h\sqrt{b}}$ = fluid resistance parameter;

η = dynamic viscosity of fluid;

$\tau \equiv \omega_0 t$ = dimensionless time coordinate;

$\xi \equiv \dfrac{x}{L}$ = dimensionless position coordinate;

ξ^* = viscous damping ratio of the equivalent SDOF system;

$\phi(x)$ = amplitude of $y(x,t)$;

$\phi(\xi)$ = amplitude of $\bar{y}(\xi,\tau)$;

$\theta(t) = \theta_0 e^{i\omega t}$ = imposed harmonic relative rotation near support;

θ_0 = amplitude of imposed harmonic relative rotation near support;

θ_e = effective rotation of the beam-support interface;

σ_x = bending stress along x-direction;

σ_y = bending stress along y-direction;

$\sigma_{max}(x,t)$ = maximum bending stress on the cross section at position x at time t;

$\varepsilon_{max,\ root}$ = amplitude of the maximum bending strain at the root of cantilever;

$\bar{\varepsilon}_{max,\ root}$ = normalized amplitude of the maximum bending strain at the root of cantilever;

ν = Poisson’s ratio of the beam material;

CHAPTER 1
INTRODUCTION

1.1 Background of Microcantilever-Based Sensors

In recent years microelectromechanical systems (MEMS) devices, in particular, microcantilever-based devices have been increasingly utilized in physical, chemical, and biochemical sensing applications. The interest in microcantilever-based sensors has increased mainly because of their estimated high sensitivity resulting from the large surface area-to-volume ratio [Dufour et al., 2012]. Other advantages associated with microcantilever-based sensors are label-free sensing, low cost, portability, fast sensing rate, and parallel sensing ability [Boisen et al., 2011]. Small size, simple structure and ability to operate in both liquid and gas make microcantilevers highly attractive sensing platforms [Finot et al., 2008]. Because of these many benefits, microcantilevers have generated interest in fields as diverse as medicine (specifically for the screening of diseases, blood glucose monitoring), in-situ environmental monitoring, and detection of chemical and biological warfare agents.

Microcantilevers were first used in atomic force microscopy (AFM) as a force sensor to image surfaces [Binnig et al., 1986]. The discovery that humidity, temperature and chemical adsorption influence the quasi-static deflection and resonant frequency of microcantilever probes in AFM led to the use of microcantilevers in chemical, physical, biological, and biochemical sensing applications [Thundat et al., 1994].

Microcantilever-based sensors consist of an inert base material as the main structure which is coated with a sensing layer or receptor [Lavrik et al., 2004] that sorbs specific analytes of interest from the ambient environment. Microcantilever-based sensors can be operated in either the static mode or the dynamic (resonant) mode [Lavrik et al., 2004; Finot et al., 2008]. In the static mode of operation the quasi-static deflection of the cantilever, due to analyte-induced surface effects, is measured, while in the dynamic mode the resonant frequency, affected by sorbed mass, is monitored. Any changes in deflection (static mode) or shifts in frequency (dynamic mode) may be used to quantify the concentration of analyte present in the operating environment. For the dynamic-mode sensors, the accurate measurement of resonant frequency and frequency shift greatly depends on the quality factor Q associated with the resonant peak of the system. Larger Q values represent sharper resonant peaks which can be measured easily, thus giving accurate readings for resonant frequency and frequency shifts. Smaller Q values correspond to broader resonant peaks from which it is difficult to measure resonant frequency and frequency shifts accurately. Therefore, achieving high-Q resonances is of paramount importance if a resonator is to be employed as an effective dynamic-mode sensor; indeed, this has been a major obstacle in the development of microcantilever-based sensors for liquid-phase detection. For this reason modeling the dynamic mode operation of microcantilevers in liquids will be a primary focus of the present work.

Different methods of measuring the cantilever deflection can be employed. Optical read-out using a laser [Lavrik et al., 2004; Boisen et al., 2011] and piezoresistive read-out [Beardslee et al., 2012] are two commonly used methods for measuring cantilever deflection. Optical read-out uses a laser to track the tip of the cantilever and thus determine its deflection response. As an example of the piezoresistive read-out method, the deflection may be indirectly measured using a piezoresistive Wheatstone bridge near the support. The bending strain will cause a change in resistance of the piezoresistors which in turn alter the bridge voltage. This change in voltage can then be related to the deflection of the microcantilever [Cox, 2011]. In the modeling efforts to be pursued in the present work, both read-out methods will be considered.

Dynamically driven microcantilevers can be excited in various modes: the transverse (out-of-plane) flexural mode, the lateral (in-plane) flexural mode, the torsional mode, and the axial mode. The most commonly used exciting mode for dynamic mode microcantilevers is the transverse mode mainly because it is the most flexible mode, i.e., the mode in which the beam “naturally” tends to vibrate. This mode of excitation has been successfully employed in many gas-phase sensing applications [e.g., Thundat et al., 1995; Lange et al., 2002; Rogers et al., 2003; Vancura et al., 2005; Tetin et al., 2010]. When the transverse mode is used for liquid phase sensing, however, the drastic drop in quality factor and resonant frequency compared to gas phase sensing makes liquid-phase sensing unfeasible [e.g., Dufour et al., 2007a; Vancura et. al., 2008]. This is mainly caused by the added mass and damping associated with the liquid [Dufour et al., 2007a; Dufour et al., 2012; Cox et al., 2012]. The cantilever drags a portion of the liquid with it as it vibrates, causing an increase in its effective mass and therefore a decrease in the resonant frequency. Also, the viscosity of the liquid increases the damping of the system (the dissipation of energy increases), which results in a severe decrease in the quality factor as well as a drop in resonant frequency. To overcome these detrimental effects of the liquid, the lateral mode of vibration can be utilized [Sharos et al., 2004; Dufour et al., 2004; Dufour et al., 2007a]. The lateral mode is stiffer than the fundamental transverse mode, but it involves less effective fluid mass and lower levels of viscous damping due to the more “streamelined” orientation (see Fig. 1-1), thus resulting in higher quality factors and resonant frequencies [Dufour et al., 2004; Dufour et al., 2007a]. Experimental investigations [Beardslee et al., 2010a-d; Beardslee et al., 2012] and theoretical studies [Heinrich et al., 2010a, b; Cox et al., 2012] have already explored in detail how the lateral mode of vibration may significantly improve the quality factor and resonant frequency of a microcantilever resonating in a liquid medium. These studies have also quantified the strong role that the dimensions of the microbeam have on the resonant characteristics of the device.

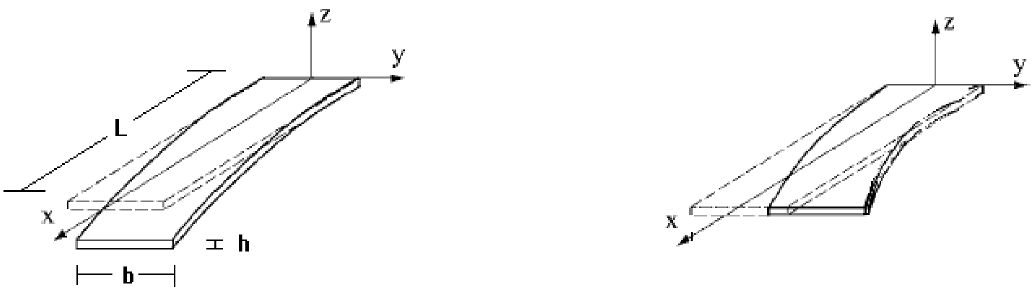

(a) (b)

Figure 1-1: Two flexural modes of a microcantilever device: (a) the conventional transverse (out-of-plane) bending mode; (b) the lateral (in-plane) bending mode.

1.2 Motivation for the Study

As noted in the previous section, the transverse flexural mode is not a viable option for liquid-phase microcantilever-based sensing because of the fluid inertia and the large energy losses that take place due to viscous dissipation in the liquid. The associated degradation of the resonant characteristics translates into poorer mass sensitivities and limits of detection when the microcantilever is used as a platform for sensing. Some recent studies by the Marquette University/Georgia Tech/University of Bordeaux

(MU/GT/UB) research team – in particular, the theoretical work by Heinrich et al., (2010a, b), which were based on Bernoulli-Euler beam theory for the perfectly fixed case, and the experimental work by Beardslee at el., (2010a-d) -- have shown that the most effective design for a microcantilever-based sensor vibrating in the lateral mode in a viscous fluid is a microcantilever that is short and wide. However, for short and wide beams the perfectly fixed beam model based on classical Bernoulli-Euler beam theory loses its accuracy likely due to (1) Timoshenko beam effects of shear deformation and rotatory inertia, and (2) support compliance effects. The influence of the Timoshenko beam effects has recently been studied in detail [Schultz et al., 2013a, b], but that model also assumes a “perfect clamp” boundary condition. For microcantilevers that are relatively short and wide and loaded in lateral flexure, the microcantilever is very stiff relative to the beam’s support structure. As a result, the conventional assumption that the support is perfectly “fixed” against rotation becomes questionable. This provides one of the major motivations for the present dissertation research, i.e., to understand the effects of support compliance on the resonant characteristics of lateral-mode microcantilevers. (While the present model will be based on Bernoulli-Euler beam theory and will therefore not account for the Timoshenko beam effects considered in Schultz et al. (2013a, b), the theoretical results obtained are expected to prove valuable in future extensions to Timoshenko beam models for the compliant support case.) An important second motivation is the need to account for the fluid effects in laterally vibrating beams because the energy dissipation resulting from fluid effects is large compared to other loss mechanisms like support losses, temperature effects, internal damping, etc.

1.3 Specific Objectives of the Study

The specific objectives of the present study are the following:

1) to derive a continuous-system model (i.e., having infinite degrees of freedom) for lateral (in-plane) vibrations of a microcantilever beam in a viscous fluid, incorporating the effects of support compliance and fluid properties.
2) to formulate boundary value problems (BVPs) for the in-fluid free vibration case and in-fluid forced vibration case caused by harmonic relative rotation imposed near the support.
3) to determine the solutions to the BVPs and use these solutions to obtain theoretical results for vibration characteristics of particular relevance in dynamic-mode sensor applications, i.e., the inherent system properties of natural frequency and quality factor corresponding to a free vibration and the frequency response, resonant frequency and quality factor for the forced vibration case.
4) to quantify the rotational stiffness of the support in terms of system parameters via 3-D finite element analysis and dimensional analysis.
5) to study the impact of fluid resistance and beam geometric parameters on the natural/resonant frequency and quality factor of the beam, including the influence of support compliance.
6) to compare theoretical frequency and quality factor predictions from the new model to the values predicted by previously derived models found in the literature and with those measured in experiments of laterally vibrating microcantilevers in water.

7) to relate the derived theoretical results to the performance of laterally excited microcantilever-based liquid-phase sensors.

1.4 Problem Statement

The primary objective of this research is to derive a mechanics-based, analytical model for lateral (in-plane) vibrations of a microcantilever beam in a viscous fluid incorporating the effects of support flexibility and fluid properties. Figure 1-2 shows the geometric and material parameters of such a system along with the reference axes. Parameters L, b, and h are length, width, and thickness of the microcantilever beam, respectively. The origin is at the center of the beam-support interface with the x-, y-, and z-axes in the directions shown. The lateral deflection (in the y-direction) is denoted by $y(x,t)$. The beam is assumed to be elastically supported (in a rotational sense), i.e., not perfectly clamped at $x = 0$, and "free" at $x = L$. The beam is made of a material with Young's modulus E and mass density ρ_b and is operating in a fluid having dynamic viscosity η and mass desnity ρ_f.

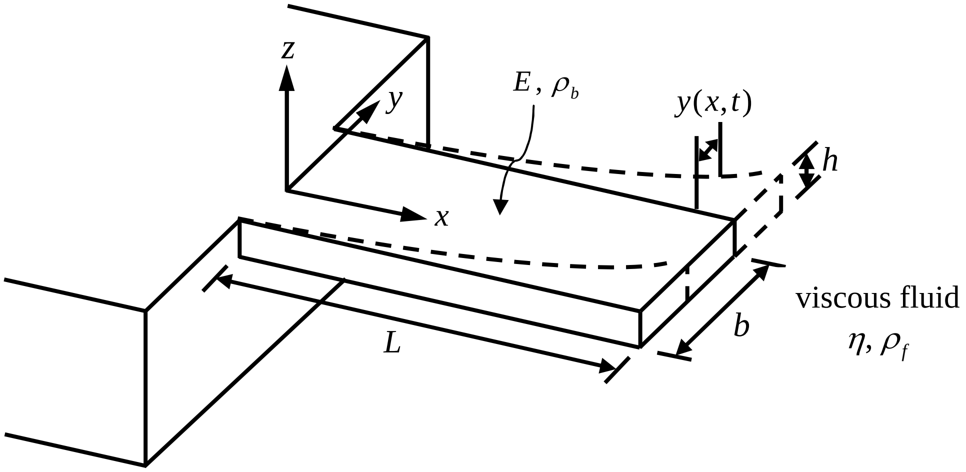

Figure 1-2: Schematic of a laterally vibrating microcantilever showing dimensions and material parameters.

The improved mathematical model to be derived in the dissertation research will involve the derivation and solution of two boundary value problems (BVPs) that account for a finite rotational support stiffness (i.e., an elastic rotational spring support) and will incorporate the fluid resistance via a “Stokes-type fluid assumption” [Heinrich et al., 2010 a, b] that utilizes the solution to Stokes’s second problem [Stokes, 1851]. Rigorous derivations and analytical solutions will be obtained for (a) the free vibration case and (b) a forced vibration caused by a harmonic relative rotation imposed at an infinitesimal distance from the spring support. The motivation behind choosing the loading of (b) is that it provides a kinematic means of simulating the electrothermal excitation utilized in recent experiments on devices that employed integrated heating resistors near the beam support [e.g., Beardslee et al., 2010a]. (See Fig. 1-3.) Such an equivalent load was introduced in a recent effort to model these devices under the assumption of infinite support stiffness [Heinrich et al., 2010b]; thus, the forced-vibration solution pursued in the present work represents an extension of the previous model to account for support compliance. For the free vibration case, the characteristic equation of the system is determined and from it the natural frequencies are determined and then the quality factors and mode shapes are determined. For the forced vibration case, the total tip displacement response and bending strain response at the root of the beam will be determined and from these responses the important dynamic characteristics associated with the harmonically excited system – namely, the resonant frequencies and resonant quality factors -- will be derived. These results for resonant/natural frequencies and quality factors will then be related to the sensor performance metrics of mass sensitivity, chemical sensitivity, and limit of detection (LOD).

For the forced vibration excitation via harmonic relative rotation near the support, the choice of the bending strain at the root of the beam as an output signal of interest is motivated by the devices tested previously [e.g., Beardslee et al., 2010a] which detect beam motion via piezoresistive elements near the cantilever support, i.e., beam motion is measured in terms of bending strain near the support. (See Fig. 1-3.) The total tip displacement response, also examined in the present work, is relevant for sensor applications that utilize an optical (laser) system to monitor total tip displacement/slope.

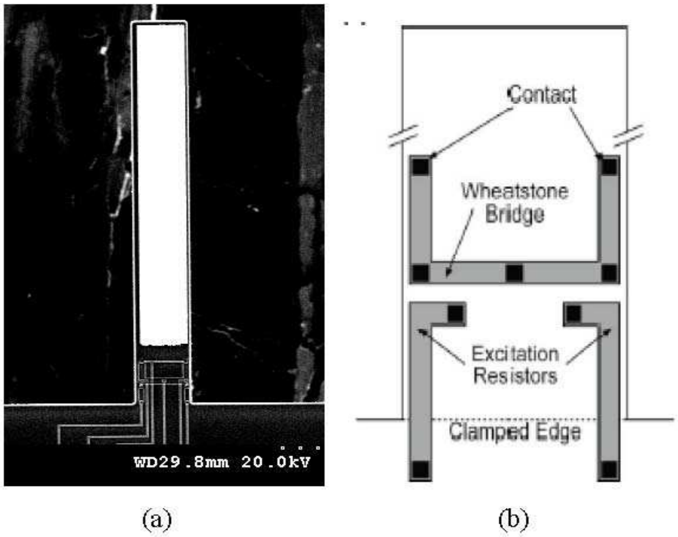

(a) (b)

Figure 1-3: Electrothermally excited microcantilever: (a) SEM image; (b) schematic of heating resistors and piezoresistive Wheatstone bridge for vibration detection [Beardslee et al., 2010b].

An important aspect of the proposed work that may perhaps have widespread applicability in the microcantilever/MEMS field is that a mechanics-based correlation study will be performed in order to relate the rotational spring constant of the support (support stiffness) to the geometric parameters (length *L*, width *b*, and thickness *h*) of the microcantilever for one of the most common support/beam interface topologies encountered in MEMS devices. This will result in analytical expressions, based on 3-D finite element analysis, which will accurately quantify rotational support stiffness in terms of *L*, *b*, and *h*.

Results of the study will be compared to other known models for particular limiting cases, including previous models and experimental data [Heinrich et al., 2010a,b; Beardslee et al., 2010a-d; Beardslee et al., 2011; Beardslee et al., 2012]. These comparisons will not only provide a verification of the new model, but will also lead to a better understanding of the effects of support flexibility and fluid properties on the lateral-mode vibration of microcantilever-based sensors operating in liquids.

1.5 Organization of Dissertation

This dissertation is organized into eight chapters. Following the present introductory chapter, which includes the background on microcantilever-based sensors, a review of relevant literature, the motivation and objective for the present study, and a statement of the problem to be investigated, a detailed review of relevant literature will be presented in Chapter 2. This review will include both transverse-mode and lateral-mode microcantilevers as well as a review of limited studies that attempt to theoretically model the effects of a compliant support on a vibrating microcantilever. In Chapter 3, the mathematical model for the lateral vibration of an elastically supported cantilever beam in a viscous fluid will be formulated as boundary value problems (BVPs) for two cases: in-fluid free vibration and in-fluid forced vibration caused by harmonic relative rotation imposed near the support. In Chapter 4, the solutions of the BVPs formulated in Chapter 3 will be obtained. Both exact and approximate analytical solutions will be derived for the in-fluid free vibration case. For in-fluid forced vibration via harmonic relative rotation near the support, the solution will be expressed in terms of the total tip displacement and the bending strain at the root. Chapter 5 will focus on the quantification of the rotational stiffness of the typical support type encountered in microcantilever applications. This stiffness will be expressed in terms of cantilever dimensions, i.e., L, b and h. This will be accomplished by using Finite Element Analysis (FEA), the results of which will be used in conjunction with a dimensional analysis based on the Buckingham Pi Theorem in order to rationally deduce a simple analytical expression for the dimensionless rotational support stiffness. In Chapter 6 parametric studies based on the results obtained in the previous chapters will be performed and discussed. These theoretical results will also be compared with recent theoretical and experimental results from the literature. In Chapter 7 the results for resonant frequencies and quality factors will be related to the performance characteristics of microcantilever-based sensors, namely, mass sensitivity, chemical sensitivity and limit of detection (LOD), and recommendations for achieving optimum cantilever geometries for sensing applications will be made. A summary of the study, including the main conclusions as well as recommendations for future work, will be given in Chapter 8.

CHAPTER 2
LITERATURE REVIEW OF RESONANT MICROCANTILEVERS

2.1 Introductory Remarks

In this chapter a literature review of analytical and experimental studies pertaining to resonant cantilevers and dynamic-mode microcantilever-based sensors, many having applications in the realm of chemical and biochemical sensing, is presented. The literature review begins by summarizing several of the important works on dynamically operated transverse-mode microcantilevers in both gas and liquid media. Previous analytical and experimental studies on resonating lateral-mode microcantilevers operating in fluid are then reviewed. These studies on lateral flexural vibrations were primarily motivated by the desire to overcome the detrimental effects of a surrounding liquid (fluid inertia and viscous energy dissipation) on the resonant characteristics of transverse-mode sensors. These studies have shown that the improvement in the in-liquid resonant characteristics are more pronounced for shorter and wider microcantilevers for which support compliance effects might be of significant importance, thereby providing the context for the present research whose primary objective is to quantify the effects of support comliance and liquid resistance on the resonant characteristics of microcantilevers and the associated performance of microcantilever-based sensors. Also, to place the present work in the proper context from a fundamental mechanics standpoint, some earlier papers published in the mechanics literature that explore support compliance and its effect on vibrating cantilever beams are discussed as the present study builds upon some of the approaches taken by prior researchers.

2.2 Transverse-Mode Microcantilevers

With the invention of atomic force microscope (AFM) in 1986, microcantilevers were utilized as imaging probes in AFM devices [Binnig et al., 1986]. In 1994, Thundat observed that relative humidity, temperature and vapor adsorption influenced the deflection and resonant frequency of microcantilever probes in AFM [Thundat et al., 1994]. This discovery, especially regarding the effect of vapor adsorption on deflection and resonant frequency, initiated the use of microcantilevers as the basis for novel chemical sensors in mid-1990s [Barnes et al., 1994; Thundat et al., 1994, 1995]. Ever since, transverse-mode microcantilevers operating in the dynamic (resonant) mode have been used in various gas-phase sensing applications, e.g., for detection of mercury vapor [Thundat et al., 1995; Rogers et al., 2003], carbon dioxide and helium [Tetin et al., 2010], and volatile organic compounds [Lange et al., 2002; Vancura et al., 2003, 2005]. These devices have also been used as chemical and biological sensors involving liquid-phase detection [e.g., Tamayo et al., 2001; Lavrik et al., 2004; Li et al., 2006]. However, transverse-mode microcantilevers operating dynamically in viscous liquids suffer severe reductions in resonant frequency and quality factor (relative to the in-vacuum or in-gas cases), thus decreasing their sensing capabilities [e.g., Schaffer et al., 1996; Chon et al., 2000; Basak et al., 2006; Dufour et al., 2007a; Vancura et. al., 2008]. This is mainly caused by the added mass and damping associated with the liquid [Dufour et al., 2007a, 2012; Ghatkesar et al., 2008; Cox et al., 2012].

With the resonant characteristics of a microcantilever being strongly dependent on the fluid in which it operates, detailed theoretical studies of the interaction of vibrating cantilevers and viscous fluids have been the subject of several studies in recent years. In

1998, Sader presented a theoretical analysis of the frequency response of a cantilever beam of arbitrary cross section, operating in a viscous fluid via an arbitrary driving force with practical relevance to AFM applications [Sader, 1998]. He incorporated the viscous fluid effects (hydrodynamic forces) by introducing a hydrodynamic function for an infinitely thin rectangular blade oscillating out-of-plane. His work was relevant to practical AFM devices which typically involve transversely vibrating cantilevers of thin rectangular cross section. To test the validity and accuracy of Sader's theoretical model, experimental investigations were made on the frequency response of AFM cantilever beams immersed in different fluids (air, acetone, CCL_4, water, and 1-butanol), demonstrating good agreement between the theory and the experimental data for all fluids tested [Chon et al., 2000]. Green and Sader (2005) extended Sader's earlier model by including the effects of a solid surface at an arbitrary distance from the vibrating cantilever. Subsequently, an investigation was done on the frequency response of rectangular cantilevers in viscous fluids for arbitrary transverse and torsional modes considering three-dimensional flows around the cantilever [Van Eysden and Sader, 2007]. Maali et al. (2005) experimentally investigated the influence of the fluid motion on the oscillating behavior of an AFM cantilever, considering up to 8 vibration modes, while also rewriting Sader's solution of 1998 in an alternative form. Ghatkesar et al. (2008) experimentally obtained in-liquid quality factor and resonant frequencies for the first 16 transverse modes using an array of 8 microcantilevers and compared the results with Sader's (1998) and Van Eysden and Sader's (2007) models. Both models compared well with the experimental results for quality factor. The frequency results were estimated well by the latter model, but the former model showed large deviation in estimating frequency due to its development being restricted to the fundamental mode. The quality factors obtained were relatively low but increased with higher modes (1 at mode 1 to 30 at mode 16), indicating that the fluid effects were less prominent at higher modes. The theoretical models used for comparison were based on homogeneous cantilevers, but in practical applications the substrate material may be coated with one or more layers, often including a sensing layer (possibly viscoelastic) to sorb particular analytes. Subsequent research has investigated the effect of the coating viscoelaticity (non-mass effect) and the fluid on the resonant frequency and quality factor [Sampath et al., 2006; Dufour et al., 2007b; Cox et al., 2008]. A recent generalization of the hydrodynamic function used in the 1998 Sader paper was made by Brumley et al. (2010), in which the effect of an arbitrary aspect ratio of the rectangular cross section was studied in detail, in addition to the effect of Reynolds number.

As noted earlier, the performance of dynamically operated transverse-mode microcantilever-based sensors in liquid-phase operation deteriorates due to the viscous dissipative and inertial effects of the liquid. To overcome this problem in liquid-phase sensing, recent research has examined alternative vibration modes in place of the transverse flexural mode. For example, torsional modes [e.g., Green and Sader, 2002, 2005; Johnson and Mutharasan, 2011; Cai et al., 2012] and axial (longitudinal) modes [e.g. Castille et al., 2010] have been investigated in the literature in an effort to improve liquid-phase sensing. One of these alternative modes that has been suggested in the recent literature is the lateral (in-plane) flexural mode, which is the main interest of the present study. This class of devices is therefore the focus of the following section.

2.3 Lateral-Mode Microcantilevers

With the aim of lowering the detrimental effects of fluids on the resonant frequencies and quality factors of microcantilever devices, the lateral flexural mode of vibration has been explored both experimentally and theoretically. Sharos et al. (2004) performed experiments on laterally vibrating microcantilevers and with the aid of finite element analysis showed potential improvements in mass sensitivity by an order of magnitude and significant improvements in the quality factor compared to the fundamental transverse mode of vibration. Dynamic-mode microcantilevers vibrating in the lateral direction have been experimentally investigated recently [Beardslee et al., 2010a-d, 2011, 2012]. These investigations also included geometric optimization for improved resonant frequency and quality factor [Beardslee et al., 2010a; Beardslee et al., 2012]. The lateral flexural mode has been shown to enhance the sensitivity and limit of detection of sensors for liquid-phase sensing [Beardslee et al., 2010c]. In all of these experiments, the microcantilever was excited electrothermally via heating resistors near the support and a piezoresistive detection method was used. (See Fig. 1-3.)

Recently, lateral mode microcantilevers operating in viscous fluid have been theoretically investigated [Dufour et al., 2004; Dufour et al., 2007a; Heinrich et al., 2010a, b; Cox et al., 2012]. Many of these studies were made in tandem with the aforementioned experimental studies. Approximate values of the in-liquid quality factor and resonant frequency for transverse and lateral mode vibrations of microcantilevers have been theoretically determined and compared by Dufour et al. (2004; 2007a) using Sader’s model [Sader, 1998]. Those papers indicated that the viscous losses were reduced for the lateral case due to the beam’s more streamlined orientation and, thus, the quality factor and resonant frequency were larger, improving the sensitivity and limit of detection of the device. The frequency also increased due to the increase in stiffness corresponding to strong-axis (in-plane) bending. However, the theoretical model that was employed in these studies ignored the shear stresses exerted by the fluid on the larger faces of the cantilever for the lateral-mode case. For this reason the advantages of the lateral mode may have been overestimated.

To improve the theoretical model for the lateral vibration mode, Heinrich et al., (2010a) modeled the cantilever as a single-degree-of-freedom (SDOF) system using as a shape function the fundamental mode shape of a perfectly fixed cantilever in vacuum and employing the assumption of Stokes-type fluid resistance. The cantilever was excited via a harmonic lateral tip force and closed-form analytical expressions for resonant frequency and quality factor were obtained. The results for quality factor (Q) were then compared to the experimental work of Beardslee et al. (2010a). The comparison showed that the SDOF model gave an excellent quantitative estimate of the experimental Q for relatively thin cantilevers; for thicker specimens the analytical formula provided an upper bound on the experimental Q (most likely due to the neglected drag on the smaller faces of the beam and the support deformation that was neglected), yet still provided a reasonable quantitative estimate.

It is to be noted that the actuation method employed in recent experimental studies on lateral-mode devices was based on electrothermal excitation via integrated heating resistors near the beam support [Beardslee et al., 2010a-d; 2011; 2012]. To accurately model this type of excitation, a continuous system analytical model was derived in which an equivalent imposed support rotation was used to simulate the electrothermal actuation [Heinrich et al., 2010b]. The support rotation loading is a more accurate, mechanics-based representation for thermal excitation near the support than is the tip load, although the latter may be a more appropriate representation for other applications. The analytical results for quality factor derived from this model verified the results obtained from the previous SDOF model with harmonic tip excitation, indicating the applicability of the SDOF results for thermally excited microcantilever devices using the fundamental lateral mode. In both of the analytical models [Heinrich et al., 2010a, b] the fluid-beam interaction was modeled using the classical solution of Stokes's second problem for an oscillating infinite plate [Stokes, 1851]. This assumes that the fluid resistance is due to shear stresses on the largest faces of the beam and that the pressure effects on the narrower sides are negligible. Therefore, both of these models are applicable only for sufficiently thin microcantilevers vibrating in-plane in liquid. Recently, Cox et al. (2012) investigated lateral-mode cantilevers vibrating in viscous liquids and included the effect of fluid resistance due to pressure on the smaller faces in addition to the edge effects that were neglected in the Stokes model employed in Heinrich et al. (2010a, b). In that study a semi-analytical expression was derived for the hydrodynamic function and utilized to calculate theoretical values of resonant frequency and quality factor. The results were then compared with experimental data as well as with results for transverse-mode vibration. The laterally vibrating microcantilevers were found to have higher resonant frequency and Q compared to their transversely vibrating counterparts of the same geometry. The theoretical lateral resonant frequency compared quite well for long and narrow beams but for shorter and wider beams (e.g., for L=200 μm, b= [45, 60, 75, 90] μm) the theoretical model of Cox et al. (2012) overestimated the experimental resonant frequencies. The authors attributed this deviation from experimental data at larger *b*/*L* values as the result of Timoshenko beam effects and support compliance effects, which were not considered in that study. In most cases the theoretical quality factor in that study underestimated the experimental results but followed similar trends.

Recent theoretical and experimental studies on resonant microcantilevers operating in the lateral mode in viscous liquids have shown that the quality factors and resonant frequencies are larger for shorter and wider cantilevers [Heinrich et al., 2010a, b; Beardslee et al., 2010a, 2012; Cox et al., 2012]. Thus, these geometries are the most promising for lateral-mode sensing application. However, the previously mentioned theoretical models [Heinrich et al., 2010a, b; Cox et al., 2012] are based on the assumptions of Bernoulli-Euler beam theory and the assumption of perfect fixity at the supported end of the microcantilever. For short and wide beams in lateral flexure, these assumptions become questionable. The fact that these various assumptions no longer hold for “stubbier” beams is supported by the fact that the theoretical estimates of resonant frequency and quality factor overestimate the experimental measurements when the specimens become shorter and wider [Heinrich et al., 2010a,b]. The validity of the Bernoulli-Euler assumptions becomes questionable due to the Timoshenko beam effects of shear deformation and rotatory inertia. These effects have recently been considered in a more general theoretical model [Schultz et al., 2013a, b], but the effect of support compliance in liquid-phase vibrations of lateral-mode devices has yet to be considered. The perfect-fixity assumption becomes especially suspect regarding the assumption of zero rotation at the support. Thus, the derivation of an analytical model for the lateral-mode dynamic response of a microcantilever in a viscous fluid, including the effects of rotational support compliance, is warranted and provides the major motivation for the present work. For this reason, the next section of the literature review will focus on the support compliance effects on the dynamic response of beams, including the effect on the resonant characteristics of in-fluid lateral-mode microcantilever-based sensors.

2.4 Microcantilevers with Elastic Support

Many studies on the effects of support compliance on the static deflection of beams [e.g., O'Donnell, 1960] and the natural frequencies of vibrating flexural members [e.g., MacBain and Genin, 1973a,b] have been made since the mid-20th century, including a few recent papers that focus on MEMS/NEMS devices [Spletzer et al., 2006; 2008; Rinaldi et al., 2007; Fadel-Taris et al., 2011; Guillon et al., 2011; Tanno et al., 2012]. In the 1960 paper by W. J. O'Donnell an expression for the rotational support stiffness was derived for applications in computing the static deflection of so-called clamped beams. A decade later MacBain and Genin (1973a) studied the effect of support compliance on the natural frequencies of built-in beams and developed an expression for support stiffness for the case of the vibrating beam. In another investigation [Macbain and Genin, 1973b] the same authors took into account the Timoshenko beam effects to obtain theoretical values of the fundamental frequency and showed the effect of the rotational stiffness of the support on the fundamental frequency. Their numerical results were based on employing a finite difference formulation. The effects of translation as well as of rotation of the support on the fundamental frequency of a uniform cantilever beam were investigated by Justine and Krishnan (1980) using a matrix iteration procedure. In later studies Cook (1991) presented the derivation of an expression for the rotational stiffness of the support for finite element applications and Stevens (1996) used finite element analysis to study the deflection of cantilever beams with an integral (monolithic) elastic support of a different modulus than the beam. All three of these studies were based on two-dimensional analyses of support stiffness and did not include fluid effects. They also did not include the types of support geometries found in microcantilever-based MEMS/NEMS devices which are the focus of the present study.

Recently, engineered support compliance has been introduced to synchronize coupled multiple cantilever systems used as resonant sensors in order to improve sensitivity [Spletzer et al., 2006, 2008; Tanoo et al., 2012]. Even when support compliance is not introduced intentionally, microfabrication methods and their limitations can result in non-ideal support geometries that introduce increased levels of support compliance. The non-classical support boundary condition of AFM microcantilevers has been quantified through experiments [Rinaldi et al., 2007]. While two other recent studies [Fadel-Taris et al., 2011; Guillon et al., 2011] aimed to quantify support flexibility effects in cantilever devices at the micro- and nano-scales, the approach taken in those studies was experimental and numerical (finite element modeling) and did not attempt to derive any physics-based formulas to clearly demonstrate the influence of the various system parameters in determining support stiffness. It is also to be noted that most of these studies involved transverse beam vibration, in which case the stiffness characteristics of the support will differ from those that are relevant to the lateral vibration case which is the focus of this study. In these respects, the proposed work will fill an important gap in the literature, especially from the perspective of using three-dimensional stress analysis to quantify the rotational support stiffness for in-plane microcantilever bending and determining the effects of the support compliance on the resonant behavior of liquid-phase MEMS/NEMS devices that are becoming more prevalent in today's world.

The present chapter and the background material of Chapter 1 have described the state-of-the-art with regard to the advantages and limitations of in-fluid lateral-mode microcantilever-based devices being operated dynamically for use in sensing applications. In particular, for liquid-phase applications the lateral vibration mode decreases the negative impact of the viscous fluid effects and improves the resonant characteristics, i.e., increases the resonant frequency and quality factor of the resonating devices. But for the most promising cantilever geometries in this regard, i.e., those that are relatively short and wide, the effects of support flexibility will be most pronounced. Because such effects have yet to be adequately addressed in the literature, the present research seeks to develop an analytical model for the lateral vibration of a dynamic-mode microcantilever in a viscous fluid, including the effects of support compliance.

CHAPTER 3
MATHEMATICAL PROBLEM FORMULATION: LATERAL VIBRATION OF ELASTICALLY SUPPORTED CANTILEVER BEAM WITH STOKES-TYPE FLUID RESISTANCE

3.1 Introductory Remarks

In this chapter the mathematical model for the lateral vibration of an elastically supported cantilever beam with Stokes-type fluid resistance is formulated. The chapter begins with the assumptions made for converting the physical system (Fig. 1-2) into an idealized system (Fig. 3-1). Boundary value problems (BVPs) are explicitly formulated for two cases: in-fluid free vibration and in-fluid forced vibration caused by harmonic relative rotation imposed at an infinitesimal distance from the support. The equations of motion (EOMs) are derived by considering the equilibrium of a differential segment of beam. Respective boundary conditions (BCs) are discussed and derived. Both the EOMs and BCs are presented in non-dimensional forms.

3.2 Modeling Assumptions

In order to represent the physical system, depicted in Fig. 1-2, with an idealized model amenable to analytical treatment, the following assumptions are made:

1) Bernoulli-Euler beam theory is valid, i.e. $b << L$, such that the shear deformation and rotatory inertia of the beam are negligible. Thus, the kinematic assumption of Bernoulli-Euler theory that cross sections remain planar and normal to the bent beam axis is employed.
2) The slope of the deflected beam is small, i.e., much less than unity.

3) The beam material is isotropic and linearly elastic. (When applied to an anisotropic material, the appropriate value of Young's modulus, i.e., along the *x*–direction, should be used.)
4) The fluid is incompressible.
5) Only lateral flexural modes are considered.
6) The beam deflection at the supported end is assumed to be negligible; however, the beam may experience a non-zero rotation at the support due to support deformation. This will be incorporated into the model by the introduction of an elastic rotational spring at the supported end of the beam. The inertial effects associated with the deforming support are assumed to be negligible.
7) Issues of structural instability (i.e., out-of-plane buckling) are not considered.
8) The viscous dissipation in the fluid is the dominant energy dissipation mechanism, i.e., all other losses are negligible.
9) The cross-section is relatively thin, i.e., $h << b$, so that the fluid resistance associated with the pressure on the two smaller faces (of dimensions h x L) is negligible compared with that due to the shear resistance of the fluid on the two larger faces (of dimensions b x L).
10) The shear stress exerted by the fluid on the beam is uniform over the width dimension (b) and its magnitude is given by Stokes's classical unidirectional solution for harmonic, in-plane oscillations of an infinite plate in a viscous fluid.

The combination of assumptions 9 and 10 will be refered to as the assumption of “Stokes fluid resistance,” which is expected to be valid for sufficiently thin beams vibrating at sufficiently high Reynolds numbers [Heinrich et al., 2010 a, b]. These assumptions allow the effect of fluid resistance to be modeled as a distributed fluid mass, $\overline{m}_f$ and a distributed fluid damping coefficient, $\overline{c}_f$. (See Fig. 3-1.) These distributed fluid properties are defined per unit length of the beam and are frequency-dependent. The specific forms of the effective fluid properties can be shown to be (Appendix A)

$$\overline{c}_f = \sqrt{2\eta\rho_f b^2}\sqrt{\omega} \tag{3-1a}$$

and

$$\overline{m}_f = \frac{\sqrt{2\eta\rho_f b^2}}{\sqrt{\omega}}, \tag{3-1b}$$

where ω represents the radial frequency (rad/sec) at which the beam oscillates. (Other quantities appearing in Eqs. (3-1a,b) have been defined in Sect. 1.4.) In the present study this frequency corresponds to either the natural oscillation frequency in the presence of fluid (in the case of free vibration) or the excitation frequency (in the case of a harmonically forced vibration). It is noted that these expressions will be accurate approximations of the fluid resistance for sufficiently thin beams experiencing harmonically forced lateral vibrations at higher Reynolds numbers; however, for the free-vibration case, these expressions are approximate for another reason: they ignore the decay in the amplitude of oscillation that occurs during the free vibration. Nevertheless, the associated error incurred in the free-vibration analysis is expected to be minimal provided that the rate of decay is not high, i.e., when the equivalent damping ratio of the beam/fluid system is less than 10%. This will be the case in the high-Q liquid-phase applications of interest in the present research.

The foregoing assumptions allow the problem to be reduced to the analysis of the idealized system indicated in Fig. 3-1. The system parameters introduced in Fig. 3-1 are k, the rotational stiffness of the support; EI, the flexural rigidity of the beam cross section in lateral flexure; and $\overline{m}_b$, the mass per unit length of the beam:

$$EI = \frac{Ehb^3}{12}, \tag{3-2a}$$

$$\overline{m}_b = \rho_b hb. \tag{3-2b}$$

As mentioned earlier, $\overline{c}_f$ and $\overline{m}_f$ are the frequency- dependent effective fluid damping coefficient and effective fluid mass, respectively.

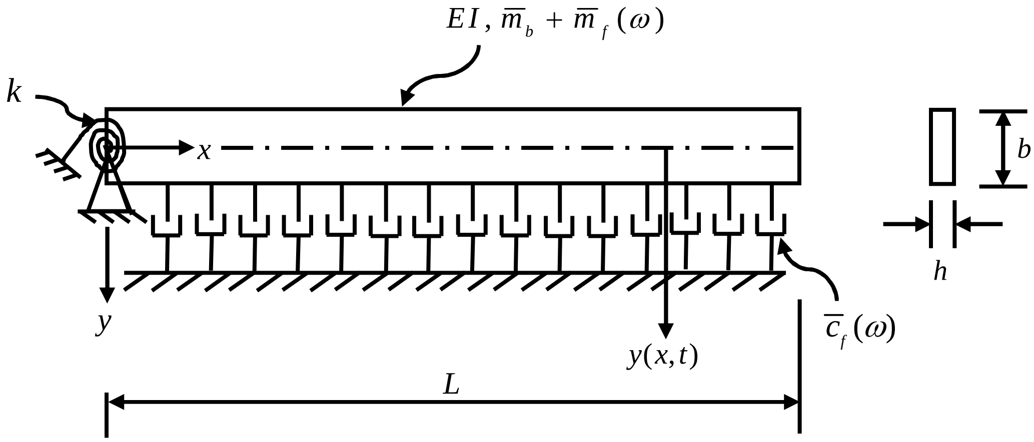

Figure 3-1: Idealized model of an elastically supported cantilever including effect of fluid resistance as distributed fluid mass and distributed fluid damping.

3.3 Governing Equation of Motion for Stokes-Type Fluid Resistance

To analyze a laterally vibrating elastically supported microcantilever with Stokes-type fluid resistance, the equation of motion governing the deflection of the microcantilever must be determined along with the necessary boundary conditions. To this end, the equation of motion for the system subjected to an arbitrary distributed harmonic loading will be formulated. Thus, the equation for the free-vibration case will simply be a special case.

Assume the beam in Fig. 3-1 is subjected to a lateral load $p(x,t) = P(x)e^{i\omega t}$ (parallel to the y-axis) that varies arbitrarily with position and harmonically in time as shown in Fig. 3-2. The equation of motion can be derived by considering the equilibrium of the forces and moments acting on the differential segment (Fig. 3-3) taken from the beam shown in Fig. 3-2. Symbols *M(x, t)* and *V(x, t)* represent the bending moment and shear force, respectively. The inertial force, $f_I(x,t)$, acting on the element can be written as follows:

$$f_I(x,t) = \left[\overline{m}_b + \overline{m}_f(\omega)\right] \ddot{y}(x,t)\, dx\,. \tag{3-3}$$

Summing all y-direction forces acting on the free-body diagram (FBD) leads to

$$V(x,t) - \left[V(x,t) + V'(x,t)\, dx\right] - P(x)e^{i\omega t}\, dx + f_I(x,t) + \overline{c}_f(\omega)\, \dot{y}(x,t)\, dx = 0 \tag{3-4}$$

In above equation and in Figs. 3-2 and 3-3, as well as in the equations that follow, the primes and dots represent differentiation with respect to space and time coordinates, respectively, unless mentioned otherwise. Substituting Eq. (3-3) into Eq. (3-4) results in

$$-V'(x,t) + \left[\overline{m}_b + \overline{m}_f(\omega)\right] \ddot{y}(x,t) + \overline{c}_f(\omega)\, \dot{y}(x,t) = P(x)e^{i\omega t}\,. \tag{3-5}$$

Similarly, moment equilibrium about point O leads to

$$\begin{aligned} &M(x,t) - \left[M(x,t) + M'(x,t)\, dx\right] + \left[V(x,t) + V'(x,t)\, dx\right]dx \\ &\qquad + P(x)e^{i\omega t}\, dx\frac{dx}{2} - \left[f_I(x,t) + \overline{c}_f(\omega)\, \dot{y}(x,t)\, dx\right]\frac{dx}{2} = 0 \end{aligned}\,, \tag{3-6}$$

wherein the rotational inertia of the differential element has been neglected.

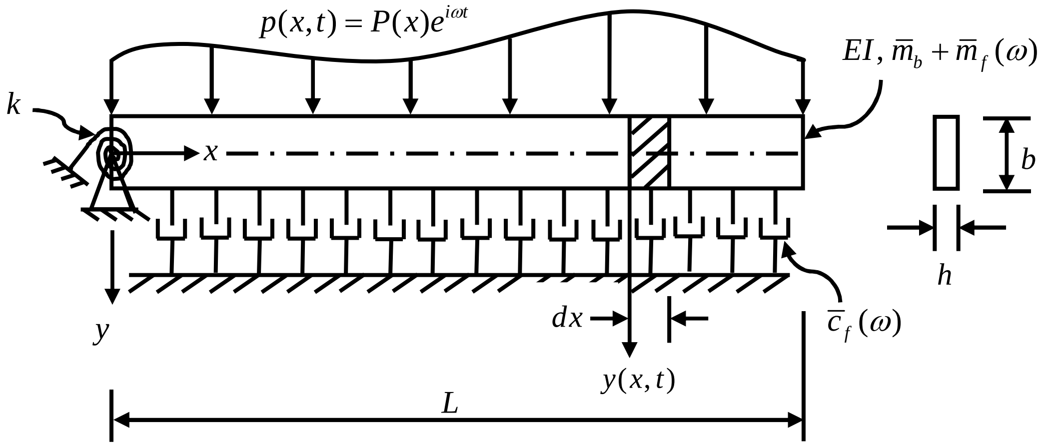

Figure 3-2: Idealized model for elastically supported cantilever subjected to an arbitrary harmonic load including effect of fluid resistance as distributed fluid mass and distributed fluid damping.

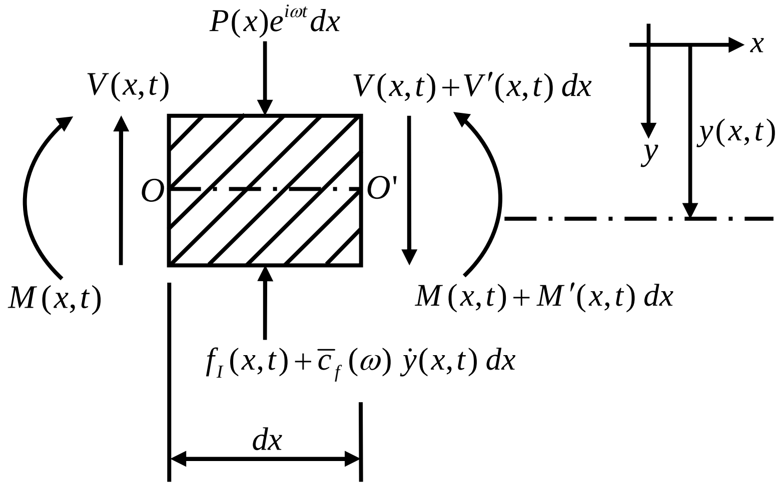

Figure 3-3: Free-body diagram (FBD) of a differential element taken from the beam shown in Fig. 3-2.

Substituting Eq. (3-3) into Eq. (3-6) and ignoring second-order terms in *dx*, Eq. (3-6) becomes

$$V(x,t)=M'(x,t)\quad . \tag{3-7}$$

Substituting Eq. (3-7) into Eq. (3-5) results in

$$-M''(x,t)+\left[\overline{m}_b+\overline{m}_f(\omega)\right]\ddot{y}(x,t)+\overline{c}_f(\omega)\dot{y}(x,t)=P(x)e^{i\omega t}\,. \tag{3-8}$$

The bending moment can be related to bending deflection by using the moment-curvature relationship from elementary bending theory [e.g., Gere and Timoshenko, 1984]

$$M(x,t)=-EIy''(x,t)\ \ . \tag{3-9}$$

Substituting Eq. (3-9) into Eq. (3-8) and assuming a prismatic beam with constant Young's modulus E along the length results in

$$EIy''''(x,t)+\left[\overline{m}_b+\overline{m}_f(\omega)\right]\ddot{y}(x,t)+\overline{c}_f(\omega)\dot{y}(x,t)=P(x)e^{i\omega t}\,. \tag{3-10}$$

This is the governing partial differential equation of motion for the system with arbitrary distributed load $p(x,t)=P(x)e^{i\omega t}$ that varies harmonically in time. But this work focuses mainly on free vibration and forced vibration caused by a harmonic relative rotation imposed near the support, both of which are cases that involve no spatial distribution of external loading. Therefore, the cases of interest correspond to $P(x)\equiv 0$, yielding the following homogeneous equation of motion:

$$EIy''''(x,t)+\left[\overline{m}_b+\overline{m}_f(\omega)\right]\ddot{y}(x,t)+\overline{c}_f(\omega)\dot{y}(x,t)=0\,. \tag{3-11}$$

The solution of this equation must, of course, satisfy the prescribed boundary conditions at $x=0$ and $x=L$ that correspond to the physical conditions present at those locations. These will be addressed in the next section.

Introducing a normalized beam deflection and dimensionless space and time coordinates, i.e.,

$$\overline{y}\equiv\frac{y}{L}\,,\qquad \xi\equiv\frac{x}{L}\,,\qquad \tau\equiv\omega_0 t\,, \tag{3-12a-c}$$

where

$$\omega_0 = \lambda_1{}^2 \frac{b}{L^2}\sqrt{\frac{E}{12\rho_b}} \tag{3-13}$$

is the natural frequency of the first lateral mode in vacuum for perfectly clamped cantilever ($\lambda_1 \equiv 1.875104$), Eq.(3-11) may be converted to the following dimensionless form:

$$\bar{y}''''(\xi,\tau)+\lambda_1{}^4\left(1+\frac{\zeta}{\lambda_1}\frac{1}{\sqrt{\bar{\omega}}}\right)\ddot{\bar{y}}(\xi,\tau)+\lambda_1{}^3\zeta\sqrt{\bar{\omega}}\,\dot{\bar{y}}(\xi,\tau)=0 \tag{3-14}$$

with

$$\zeta \equiv \left[\frac{48\eta^2\rho_f{}^2}{E\rho_f{}^3}\right]^{1/4}\frac{L}{h\sqrt{b}} = \text{dimensionless fluid resistance parameter,} \tag{3-15a}$$

and

$$\bar{\omega} \equiv \frac{\omega}{\omega_0} = \text{dimensionless frequency.} \tag{3-15b}$$

The primes and dots appearing in Eq. (3-14) now represent differentiation with respect to dimensionless space and time coordinates, respectively.

The governing equation of motion for a laterally vibrating cantilever beam with elastic support in vacuum can be easily obtained by zeroing out the dimensionless fluid resistance parameter, ζ , in Eq. (3-14). Thus the governing equation of motion in vacuum is

$$\bar{y}''''(\xi,\tau)+\lambda_1{}^4\,\ddot{\bar{y}}(\xi,\tau)=0\,. \tag{3-16}$$

3.4 Boundary Conditions

The governing equation of motion derived in Section 3.3 must be accompanied by a particular set of boundary conditions for the formulation of the boundary value problem to be complete. The number of boundary conditions required depends on the order of governing differential equation of motion. The differential equation of motion in this case is of fourth order and thus four boundary conditions are necessary, two at each end of the beam. The present study focuses on free vibration and a forced excitation involving a harmonic relative rotation near the support. Only the boundary conditions for these two cases will be discussed herein, although BCs for other cases of potential interest may easily be formulated.

Boundary Conditions for Free Vibration

The boundary conditions relevant to the free vibration case are

$$y(0,t) = 0\,, \tag{3-17a}$$

$$y'(0,t) - \frac{EI}{k} y''(0,t) = 0\,, \tag{3-17b}$$

$$y''(L,t) = 0\,, \tag{3-17c}$$

$$y'''(L,t) = 0\,. \tag{3-17d}$$

Equation (3-17a) corresponds to the lateral deflection being zero at the supported end ($x = 0$). Since the beam is not perfectly clamped, the slope need not be zero at the supported end. Instead, this condition becomes a mathematical statement that the bending moment at the end of the beam must equal the reaction moment supplied by the compliant support (i.e., by the elastic rotational spring) as described by Eq. (3-17b).

Equations (3-17c) and (3-17d) correspond, respectively, to the bending moment (or beam curvature) and shear force at free end ($x = L$) being zero.

The boundary conditions may easily be converted to dimensionless form using Eqs.(3-12a-c) and (3-15b):

$$\bar{y}(0,\tau) = 0\,, \tag{3-18a}$$

$$\bar{y}'(0,\tau) - \frac{\bar{y}''(0,\tau)}{\bar{k}} = 0\,, \tag{3-18b}$$

$$\bar{y}''(1,\tau) = 0\,, \tag{3-18c}$$

$$\bar{y}'''(1,\tau) = 0\,. \tag{3-18d}$$

where

$$\bar{k} \equiv \frac{kL}{EI} \tag{3-19}$$

represents the dimensionless rotational stiffness of the support.

Boundary Conditions for Forced Vibration via Imposed Relative Rotation near Support

For this forced vibration case, the displacement boundary condition at the supported end and the BCs corresponding to zero moment and zero shear force at free end are the same as that for the free vibration case. Thus, Eqs. (3-18a, c, d) remain unchanged; however, the equilibrium condition relating beam slope and beam curvature at the supported end is no longer given by Eq. (3-18b) since in the present case there is an imposed harmonic relative rotation near the support to simulate the electrothermal actuation (Fig. 1-3). This new boundary condition requires a careful examination and detailed derivation in order to distinguish between the imposed relative rotation and the resulting support rotation, the former corresponding to the electrothermal excitation as described in what follows.

Experimental devices [e.g., Beardslee et al., 2010a] were excited electrothermally by means of integrated heating resistors near the support. Figure 3-4 indicates the static deformation pattern, obtained via finite element analysis, of a beam that is thermally loaded at the "extreme fibers" of an arbitrary cross section. The thermal input is out-of-phase so that equal values of temperature change are specified, one being positive while the other is negative. As seen from the figure, the net effect of this type of loading may be represented kinematically as an imposed relative rotation of the beam at the location of the thermal input. This concept was utilized in a recent paper to simulate a harmonic electrothermal loading near a perfectly clamped support [Heinrich et al., 2010b]. In the present study – in which support compliance effects are to be included -- the imposed rotation associated with the heating resistors will be considered to occur at some distance $\overline{x}$ from the support in order to delineate between the loading *near* the support and the support rotation that occurs *at* the support. The two effects can then be incorporated subsequently by means of a single boundary condition by employing a limiting process, letting $\overline{x} \to 0$.

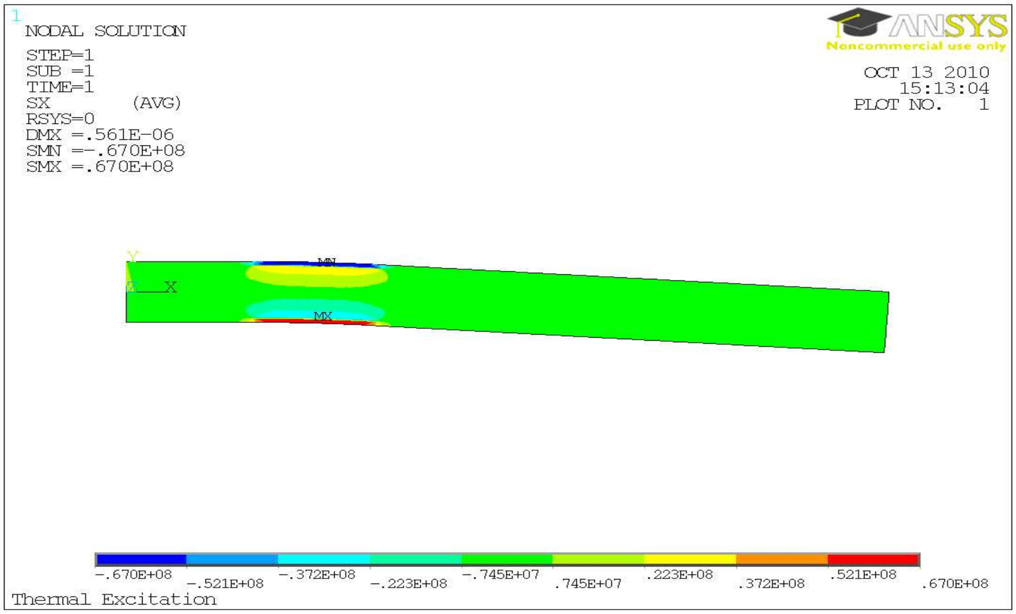

Figure 3-4: Thermally excited microcantilever via heating resistors near the support.

To derive the slope-curvature boundary condition it will be assumed that the harmonic relative rotation is applied at a distance $\bar{x}$ away from the support as shown in Fig. 3-5. The deflection response $y(x,t)$ may then be expressed in a piecewise manner as follows:

$$y(x,t)=\begin{cases} y_1(x,t) \;\; \left(0\le x\le \bar{x}\right) \\ y_2(x,t) \;\; \left(\bar{x}\le x\le L\right) \end{cases} . \tag{3-20}$$

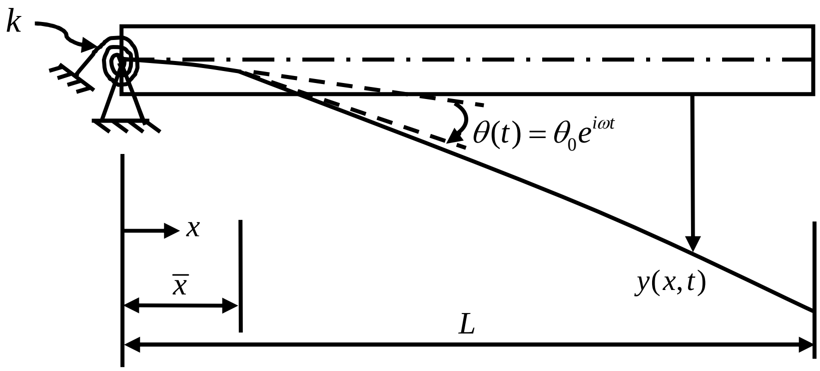

Figure 3-5: Schematic of imposed harmonic relative rotation at a distance $\bar{x}$ from the support.

The boundary conditions at the support and the continuity conditions at the point of application of relative rotation are as follows:

$$y_1(0,t) = 0\,, \tag{3-21a}$$

$$y_1'(0,t) - \frac{EI}{k} y_1''(0,t) = 0\,, \tag{3-21b}$$

$$y_2(\bar{x},t) = y_1(\bar{x},t)\,, \tag{3-21c}$$

$$y_2'(\bar{x},t) = y_1'(\bar{x},t) + \theta(t)\ \ , \tag{3-21d}$$

$$y_2''(\bar{x},t) = y_1''(\bar{x},t)\,, \tag{3-21e}$$

$$y_2'''(\bar{x},t) = y_1'''(\bar{x},t)\,, \tag{3-21f}$$

where $\theta(t) \equiv \theta_0 e^{i\omega t}$ is the harmonically varying relative rotation applied near the support. Equation (3-21a) corresponds to the lateral deflection being zero at the supported end. Equation (3-21b) corresponds to the moment reaction due to spring support being equal to the beam's bending moment at the supported end. Equations (3-21c), (3-21e), and (3-21f) correspond, respectively, to the continuity of beam deflection, bending curvature and shear force at the point of application of relative rotation. Equation (3-21d) represents the imposed discontinuity of slope at the point of application of relative rotation, which corresponds to the thermal excitation being applied at that location. Letting $\bar{x} \to 0$ in Eq. (3-21c) and using Eq. (3-21a) yields the following BC on $y_2(x,t)$ at $x=0$:

$$y_2(0,t) = 0\,. \tag{3-22a}$$

To obtain the second BC on $y_2(x,t)$ at $x=0$, the limits ($\bar{x} \to 0$) of Eqs. (3-21d, e) are taken to give

$$y_1'(0,t) = y_2'(0,t) - \theta(t)\,, \tag{3-22b}$$

$$y_1''(0,t) = y_2''(0,t)\,. \tag{3-22c}$$

These two equations may now be used to express Eq. (3-21b) in terms of y_2 only:

$$y_2'(0,t) - \frac{EI}{k} y_2''(0,t) = \theta_0 e^{i\omega t}\,, \tag{3-22d}$$

where the harmonic form of the imposed relative rotation has been inserted on the right-hand side. As, $\bar{x} \to 0$, $y_2(x,t)$ represents the displacement over the entire domain of the beam and can therefore be written simply as $y(x,t)$ for $0 \le x \le L$ and Eqs. (3-22a) and (3-22d) (without the “2” subscript) give the BCs at the left end. When combined with the zero shear and moment BCs at the right end, the four boundary conditions relevant to the problem of imposed relative rotation near the support may be summarized as

$$y(0,t) = 0\,, \tag{3-23a}$$

$$y'(0,t) - \frac{EI}{k} y''(0,t) = \theta_0 e^{i\omega t}\,, \tag{3-23b}$$

$$y''(L,t) = 0\,, \tag{3-23c}$$

$$y'''(L,t) = 0\,. \tag{3-23d}$$

The boundary conditions can easily be converted to dimensionless form using Eqs.(3-12a-c) and (3-15b). The dimensionless boundary conditions are

$$\bar{y}(0,\tau) = 0\,, \tag{3-24a}$$

$$\bar{y}'(0,\tau) - \frac{\bar{y}''(0,\tau)}{\bar{k}} = \theta_0 e^{i\bar{\omega}\tau}\,, \tag{3-24b}$$

$$\bar{y}''(1,\tau) = 0\,, \tag{3-24c}$$

$$\bar{y}'''(1,\tau) = 0\,. \tag{3-24d}$$

3.5 Summary of Boundary Value Problems to be Considered

In this section a summary of the two boundary value problems to be considered in this study will be presented. The BVPs considered are the lateral free vibration of a microcantilever in a viscous fluid and the forced lateral vibration of a microcantilever in a viscous fluid via an imposed harmonic relative rotation applied next to the compliant support.

3.5.1 Free Vibration with Stokes-Type Fluid Resistance

The dimensionless BVP for the free vibration of an elastically supported cantilever beam in a viscous fluid is given below. It is to be noted that the corresponding in-vacuum BVP can be easily obtained by zeroing out the fluid resistance parameter, ζ.

<u>Equation of Motion</u>

$$\bar{y}''''(\xi,\tau)+\lambda_1^4\left(1+\frac{\zeta}{\lambda_1}\frac{1}{\sqrt{\bar{\omega}}}\right)\ddot{\bar{y}}(\xi,\tau)+\lambda_1^3\zeta\sqrt{\bar{\omega}}\,\dot{\bar{y}}(\xi,\tau)=0\,. \tag{3-25}$$

<u>Boundary Conditions</u>

$$\bar{y}(0,\tau)=0\,, \tag{3-26a}$$

$$\bar{y}'(0,\tau)-\frac{\bar{y}''(0,\tau)}{\bar{k}}=0\,, \tag{3-26b}$$

$$\bar{y}''(1,\tau)=0\,, \tag{3-26c}$$

$$\bar{y}'''(1,\tau)=0\,. \tag{3-26d}$$

3.5.2 Forced Vibration with Stokes-Type Fluid Resistance via Harmonic Relative Rotation Imposed Adjacent to the Support

The dimensionless BVP for the forced vibration of an elastically supported cantilever beam in a viscous fluid via an imposed harmonic relative rotation adjacent to the compliant support is given below. It is to be noted that the corresponding in-vacuum BVP can be easily obtained by zeroing out the fluid resistance parameter, ζ .

Equation of Motion

$$\bar{y}''''(\xi,\tau)+\lambda_1^{\,4}\left(1+\frac{\zeta}{\lambda_1}\frac{1}{\sqrt{\bar{\omega}}}\right)\ddot{\bar{y}}(\xi,\tau)+\lambda_1^{\,3}\zeta\sqrt{\bar{\omega}}\,\dot{\bar{y}}(\xi,\tau)=0\,. \qquad (3\text{-}27)$$

Boundary Conditions

$$\bar{y}(0,\tau)=0\,, \qquad (3\text{-}28a)$$

$$\bar{y}'(0,\tau)-\frac{\bar{y}''(0,\tau)}{\bar{k}}=\theta_0 e^{i\,\bar{\omega}\,\tau}\,, \qquad (3\text{-}28b)$$

$$\bar{y}''(1,\tau)=0\,, \qquad (3\text{-}28c)$$

$$\bar{y}'''(1,\tau)=0\,. \qquad (3\text{-}28d)$$

CHAPTER 4
METHOD OF SOLUTION OF BOUNDARY VALUE PROBLEMS

4.1 Introductory Remarks

In this chapter the solutions of the BVPs summarized in Chapter 3 will be obtained. First, the solution for the in-fluid free-vibration BVP is derived. This is followed by the solution for the case of an in-fluid forced-vibration via harmonic relative rotation near the support. The corresponding in-vacuum results are special cases that may be obtained by setting $\zeta = 0$.

4.2 Solution for the In-Fluid Free-Vibration Response in Lateral Flexure

This section begins with the exact solution for in-fluid free-vibration response in lateral flexure. Later the approximate analytical results for the case of small values of fluid resistance parameter and large values of the dimensionless support stiffness are presented.

4.2.1 Exact Solution for the In-Fluid Free-Vibration Response in Lateral Flexure

The boundary value problem for the in-fluid, free-vibration of an elastically supported cantilever beam is summarized in Sect. 3.5.1 and is explicitly described by Eqs. (3-25) and (3-26a-d). For convenience, the equations are restated here:

$$\bar{y}''''(\xi,\tau) + \lambda_1^{\,4}\left(1 + \frac{\zeta}{\lambda_1}\frac{1}{\sqrt{\bar{\omega}}}\right)\ddot{\bar{y}}(\xi,\tau) + \lambda_1^{\,3}\zeta\sqrt{\bar{\omega}}\,\dot{\bar{y}}(\xi,\tau) = 0\,, \tag{4-1}$$

$$\bar{y}(0,\tau) = 0\,, \tag{4-2a}$$

$$\bar{y}'(0,\tau) - \frac{\bar{y}''(0,\tau)}{\bar{k}} = 0\,, \tag{4-2b}$$

$$\bar{y}''(1,\tau) = 0\,, \tag{4-2c}$$

$$\bar{y}'''(1,\tau) = 0\,. \tag{4-2d}$$

The solution methodology for this BVP consists of determining the characteristic equation (frequency equation), obtaining the natural frequencies (eigenvalues) from the roots of the characteristic equation, determining the quality factors for each mode, and determining the corresponding mode shapes (eigenfunctions). It will be assumed that the free-vibration response of the beam in lateral flexure will admit the form

$$y(x,t) = \phi(x)e^{i\Omega t} = \phi(x)e^{i(\omega+id)t} = \phi(x)e^{-dt}e^{i\omega t}\,, \tag{4-3}$$

where $\phi(x)$ is the unknown (possibly complex) mode shape of free vibration in fluid and $\Omega = \omega + id$ is the unknown complex natural frequency whose real part ω is the unknown damped natural frequency (frequency of oscillation in fluid) and whose imaginary part d is the unknown decay parameter. Now, the solutions to Eqs. (4-1) through (4-2a-d) are sought in a dimensionless form analogous to Eq. (4-3), i.e.,

$$\bar{y}(\xi,\tau) = \phi(\xi)e^{i\bar{\Omega}\tau} = \phi(\xi)e^{i(\bar{\omega}+i\bar{d})\tau} = \phi(\xi)e^{-\bar{d}\tau}e^{i\bar{\omega}\tau}\,, \tag{4-4}$$

where $\phi(\xi)$ is the mode shape of free vibration in fluid expressed as a function of ξ; $\bar{\Omega}$ is the unknown dimensionless complex natural frequency, $\bar{\omega}$ and $\bar{d}$ are dimensionless forms of the damped natural frequency and decay parameter, i.e.,

$$\bar{\Omega} \equiv \frac{\Omega}{\omega_0} = \bar{\omega} + i\bar{d}\,, \tag{4-5a}$$

$$\bar{\omega} \equiv \frac{\omega}{\omega_0}\,, \tag{4-5b}$$

$$\bar{d} \equiv \frac{d}{\omega_0}\,. \tag{4-5c}$$

Substituting Eq. (4-4) into Eqs. (4-1) and (4-2a-d) results in the following eigenvalue problem:

$$\phi''''(\xi) - \alpha^4 \phi(\xi) = 0\,, \tag{4-6}$$

$$\phi(0) = 0\,, \tag{4-7a}$$

$$\phi'(0) - \frac{\phi''(0)}{\bar{k}} = 0\,, \tag{4-7b}$$

$$\phi''(1) = 0\,, \tag{4-7c}$$

$$\phi'''(1) = 0\,, \tag{4-7d}$$

where the unknown parameter α is related to the fluid resistance parameter and the unknown free vibration response parameters through

$$\alpha^4 \equiv \lambda_1^{\,4} \left(1 + \frac{\zeta}{\lambda_1} \frac{1}{\sqrt{\bar{\varpi}}} \right) \left(\bar{\varpi}^2 + i2\bar{\varpi}\bar{d} - \bar{d}^{\,2} \right) - \lambda_1^{\,3} \zeta \sqrt{\bar{\varpi}} \left(i\bar{\varpi} - \bar{d} \right). \tag{4-8}$$

The general solution of Eq. (4-6) may be written as

$$\phi(\xi) = A_1 \cos\alpha\xi + A_2 \sin\alpha\xi + A_3 \cosh\alpha\xi + A_4 \sinh\alpha\xi\,, \tag{4-9}$$

where A_i, i =1, 2, 3, 4 are as yet undetermined constants. Imposing the BCs (4-7a-d) on the general solution leads to the following system of linear algebraic equations:

$$\left[e \right] \left\{ A \right\} = \left\{ 0 \right\}, \tag{4-10}$$

where

$$\left[e \right] = \begin{bmatrix} 1 & 0 & 1 & 0 \\ \alpha & \bar{k} & -\alpha & \bar{k} \\ -c & -s & C & S \\ s & -c & S & C \end{bmatrix}\,, \tag{4-11}$$

$$\{A\}=\begin{Bmatrix}A_1\\ \\ A_2\\ \\ A_3\\ \\ A_4\end{Bmatrix}, \tag{4-12}$$

and

$$c\equiv\cos\alpha\,,\ C\equiv\cosh\alpha\,,\ \ s\equiv\sin\alpha\,,\ \ S\equiv\sinh\alpha\,. \tag{4-13a-d}$$

The following characteristic equation can be obtained by setting the determinant of matrix $\left[e\right]$ equal to zero, which is necessary for Eq. (4-10) to have a non-trivial solution:

$$1+Cc=\frac{\alpha}{\bar{k}}\left(Cs-cS\right). \tag{4-14}$$

The positive real roots of Eq. (4-14) will depend on the dimensionless rotational stiffness of the support, $\bar{k}$, and shall be denoted by α_n, n=1, 2, 3, ... with $\alpha_1<\alpha_2<\alpha_3<\ldots$.

Natural Frequencies

For a specified value of dimensionless rotational stiffness $\bar{k}$, the positive real roots α_n can be determined numerically from Eq. (4-14), but one must still determine the physically meaningful free-vibration response parameters, $\bar{\omega}_n$ and $\bar{d}_n$, which correspond to each of the real numbers, α_n, n=1, 2, ... Substituting the value of α_n into Eq. (4-8) and equating the real and imaginary parts of the resulting equation leads to

$$\lambda_1^{\,4}\left(1+\frac{\zeta}{\lambda_1}\frac{1}{\sqrt{\bar{\omega}_n}}\right)\left(\bar{\omega}_n^{\,2}-\bar{d}_n^{\,2}\right)+\lambda_1^{3}\zeta\sqrt{\bar{\omega}_n}\,\bar{d}_n=\alpha_n^{\,4}, \tag{4-15}$$

$$\lambda_1^{\,4}\left(1+\frac{\zeta}{\lambda_1}\frac{1}{\sqrt{\bar{\omega}_n}}\right)\left(2\bar{\omega}_n\bar{d}_n\right)-\lambda_1^{3}\zeta\,\bar{\omega}_n^{\,3/2}=0. \tag{4-16}$$

Simplification of Eq. (4-16) gives

$$\bar{d}_n = \frac{\zeta\,\bar{\omega}_n}{2\lambda_1\left(\sqrt{\bar{\omega}_n} + \frac{\zeta}{\lambda_1}\right)} \;. \tag{4-17}$$

Substituting Eq. (4-17) into Eq. (4-15) results in the following equation:

$$4\left(\sqrt{\bar{\omega}_n}\right)^5 + \frac{8\zeta}{\lambda_1}\left(\sqrt{\bar{\omega}_n}\right)^4 + \frac{5\zeta^2}{\lambda_1^2}\left(\sqrt{\bar{\omega}_n}\right)^3 - \frac{4\alpha_n^{\;4}}{\lambda_1^4}\left(\sqrt{\bar{\omega}_n}\right) - \frac{4\zeta\alpha_n^{\;4}}{\lambda_1^5} = 0\,. \tag{4-18}$$

Equation (4-18) is a fifth-degree polynomial in $\sqrt{\bar{\omega}_n}$; thus, the square of the positive real root of this polynomial is the dimensionless damped natural frequency, $\bar{\omega}_n$, which depends on the fluid resistance parameter, ζ, and the dimensionless rotational stiffness of the support, $\bar{k}$. Once $\bar{\omega}_n$ has been determined for a particular mode *n*, the corresponding decay parameter, $\bar{d}_n$, may be obtained using Eq. (4-17).

Viscous Damping Ratios and Quality Factors

The form of the free-vibration response in Eq. (4-3) is identical to that of a viscously damped single-degree-of-freedom (SDOF) system [e.g., Tedesco et al., 1999]. It may easily be shown that the viscous damping ratio of this equivalent SDOF system is given by

$$\xi_n^{\;*} = \frac{\bar{d}_n}{\sqrt{\bar{\omega}_n^{\;2} + \bar{d}_n^{\;2}}} \,. \tag{4-19}$$

Thus, Eq. (4-19) may be considered to represent the viscous damping ratio associated with the nth lateral flexural mode of a freely vibrating cantilever with Stokes-type fluid resistance. Substituting Eq. (4-17) into Eq. (4-19) results in

$$\xi_n^* = \frac{\zeta}{2\lambda_1} \frac{1}{\sqrt{\bar{\omega}_n + \frac{2\zeta}{\lambda_1}\sqrt{\bar{\omega}_n} + \frac{5\zeta^2}{4\lambda_1^2}}} . \tag{4-20}$$

The quality factors, Q_n, defined here in terms of the reciprocal of the respective damping ratios, can be obtained using Eq. (4-20) as

$$Q_n \equiv \frac{1}{2\xi_n^*} = \frac{\sqrt{\bar{\omega}_n^2 + \bar{d}_n^2}}{2\bar{d}_n} = \frac{\lambda_1}{\zeta}\sqrt{\bar{\omega}_n + \frac{2\zeta}{\lambda_1}\sqrt{\bar{\omega}_n} + \frac{5\zeta^2}{4\lambda_1^2}} . \tag{4-21}$$

Mode Shapes

Knowing the values of α_n from Eq. (4-14) and substituting them into Eq. (4-10), one may solve for the constants A_2, A_3 and A_4 in terms of A_1; thus, using Eq. (4-9), the specific form of the mode shapes of free vibration in a viscous fluid may be written as

$$\phi_n(\xi) = A_1\left(\cos\alpha_n\xi - \cosh\alpha_n\xi - \frac{C_n + c_n + \frac{2\alpha_n}{\bar{k}}S_n}{S_n + s_n}\sin\alpha_n\xi + \frac{C_n + c_n - \frac{2\alpha_n}{\bar{k}}s_n}{S_n + s_n}\sinh\alpha_n\xi \right), \tag{4-22a}$$

where

$$c_n \equiv \cos\alpha_n \,, C_n \equiv \cosh\alpha_n \,,\ s_n \equiv \sin\alpha_n \,,\ S_n \equiv \sinh\alpha_n \,. \tag{4-22b-e}$$

Here A_1 represents the arbitrary amplitude of the mode shape functions, $\phi_n(\xi)$. It is to be noted that these mode shapes are independent of the fluid parameters and thus are the same as for the in-vacuum case.

4.2.2 Approximate Analytical Results for Small Fluid Resistance and Small Support Compliance

In many cases of practical interest the fluid resistance parameter ζ is expected to be much smaller than 1. For example, for a silicon cantilever with dimensions *L*x*b*x*h* =

(400x50x10) μm immersed in water, $\zeta = 0.07$. Also, for many practical cases the normalized rotational support compliance, $1/\bar{k}$, is expected to be much smaller than unity. This provides the motivation to derive simple analytical expressions for the results derived earlier (dimensionless natural frequency and quality factor) in those cases for which the values of the fluid resistance parameter and rotational support compliance are small. Since for most lateral-mode sensing applications the first lateral mode of vibration is the most easily excited, this section will only consider the results for the fundamental mode of lateral vibration.

To this end it will be assumed that $\sqrt{\varpi_1}$ may be expanded in a power series in ζ as

$$\sqrt{\varpi_1} = c_0 + c_1\zeta + O(\zeta^2) \quad \text{as} \quad \zeta \to 0, \tag{4-23}$$

where ϖ_1 is the mode-1 dimensionless natural frequency; c_0 and c_1 are coefficients which may depend on $1/\bar{k}$ and may be obtained by substituting Eq. (4-23) into Eq. (4-18) , expanding the left-hand side of Eq. (4-18), and subsequently equating the coefficients on like powers of ζ up to the linear term. The coefficients are

$$c_0 = \frac{\alpha_1}{\lambda_1}, \qquad c_1 = -\frac{1}{4\lambda_1}. \tag{4-24a-b}$$

The expression for ϖ_1 is obtained by squaring Eq. (4-23) as follows:

$$\varpi_1 = c_0{}^2 + 2c_0c_1\zeta + O(\zeta^2) \quad \text{as} \quad \zeta \to 0. \tag{4-25}$$

If the coefficients of Eq. (4-25) are subsequently expanded in powers of $1/\bar{k}$ and all higher-order terms (higher than first-order) are ignored, the resulting bilinear approximation for ϖ_1 is only moderately accurate when $1/\bar{k}$ is in the vicinity of 0.1. Therefore, to obtain an analytical result having better accuracy, an alternative approach shall be taken. Recognizing that the first term on the right hand side of Eq. (4-25) (i.e., $c_0^{\ 2}$) represents the mode-1 dimensionless natural frequency in vacuum for the case of a compliant support, $\bar{\varpi}_{1,vac}$, this term may be approximated quite accurately by fitting the curve of the exact $\bar{\varpi}_{1,vac}$ vs. $1/\bar{k}$, obtained using Eq. (4-18) with $\zeta = 0$, instead of expanding analytically about $1/\bar{k} = 0$. Figure 4-1 shows a plot of the exact $\bar{\varpi}_{1,vac}$ vs. $1/\bar{k}$ for the first-mode lateral vibration and the corresponding quadratic polynomial curve-fit. The range of $1/\bar{k}$ considered for the fit is 0 to 0.15, which is expected to include most practical cases for the application of interest and the support configuration considered. In performing the fit, the value of normalized frequency is forced to be 1 when $1/\bar{k} = 0$ in order to agree with the perfectly fixed case. The maximum error of the fit over the range of $1/\bar{k}$ considered is 0.22%. The expression for $\bar{\varpi}_{1,vac}$ obtained from the quadratic curve-fitting for the range of $1/\bar{k}$ considered is

$$\bar{\varpi}_{1,vac} = c_0^{\ 2} \approx 1 - 1.909\frac{1}{\bar{k}} + 3.417\left(\frac{1}{\bar{k}}\right)^2 . \qquad (4\text{-}26)$$

Substituting Eq. (4-26) into the first term on the right-hand side of Eq. (4-25) and Eqs. (4-24a-b) into the second term results in

$$\bar{\varpi}_1 \approx 1 - 1.909\frac{1}{\bar{k}} + 3.417\left(\frac{1}{\bar{k}}\right)^2 - \frac{\alpha_1}{2\lambda_1^{\ 2}}\zeta + O\left(\zeta^2\right) \text{ as } \quad \zeta \to 0 . \qquad (4\text{-}27)$$

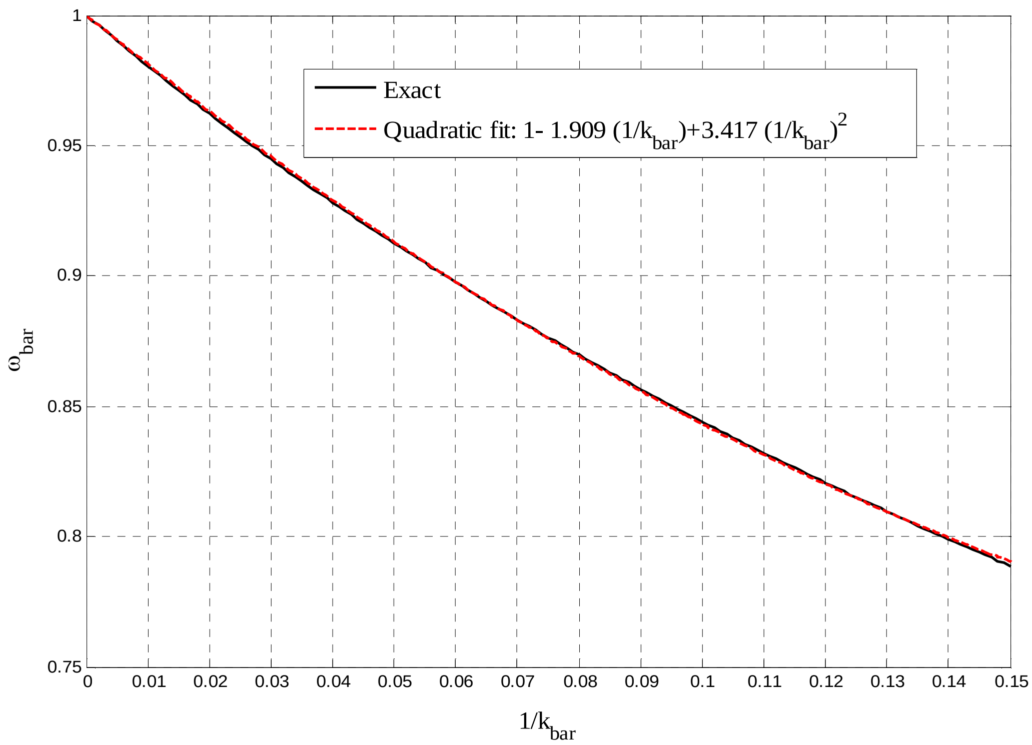

Figure 4-1: In-vacuum exact dimensionless natural frequency for fundamental lateral mode and quadratic curve fit. $\left(0 \le 1/\bar{k} \le 0.15\right)$

Equation (4-27) depends on the first positive real root of the characteristic equation (Eq. (4-14)), α_1, which in turn depends on the dimensionless rotational compliance of the support, $1/\bar{k}$. If one assumes that α_1 may be expanded in a power series in terms of $1/\bar{k}$, α_1 may be written as

$$\alpha_1 = a_0 + a_1\left(\frac{1}{\bar{k}}\right) + O\left(\left(\frac{1}{\bar{k}}\right)^2\right) \quad \text{as} \quad \frac{1}{\bar{k}} \to 0, \tag{4-28}$$

where a_0 and a_1 are the coefficients to be determined. Substituting Eq. (4-28) into Eq. (4-14), expanding both sides of Eq. (4-14), and subsequently equating the coefficients on like powers of $1/\bar{k}$ gives following two equations:

$$1+\cosh a_0 \cos a_0 = 0\,; \tag{4-29a}$$

$$a_0 + a_1 = 0\,. \tag{4-29b}$$

Equation (4-29a) is the characteristic equation for the free vibration of a perfectly supported ("fixed") cantilever in vacuum and the positive real roots of this equation are well known [e.g., Clough and Penzien, 2003]. The first root shall be denoted by λ_1, whose value is listed below to 7-significant-figure accuracy:

$$\lambda_1 \equiv 1.875104\ . \tag{4-30}$$

(Note that λ_1 has been introduced previously in Eq. (3-13).) Therefore, from Eqs. (4-29a-b), the coefficients are:

$$a_0 = \lambda_1\,; \tag{4-31a}$$

$$a_1 = -\lambda_1\,. \tag{4-31b}$$

Substituting Eq. (4-31a-b) into Eq. (4-28) gives

$$\alpha_1 = \lambda_1 \left[1 - \frac{1}{\bar{\bar{k}}} + O\left(\frac{1}{\bar{\bar{k}}}\right)^2 \right] \text{ as } \frac{1}{\bar{\bar{k}}} \to 0\,. \tag{4-32}$$

Substituting Eq. (4-32) into Eq. (4-27) results in the approximate expression for the mode-1 dimensionless natural frequency of a laterally vibrating cantilever beam with elastic support and Stokes-type fluid resistance for the case $\zeta << 1$ and $1/\bar{k} << 1$ as follows:

$$\bar{\omega}_1 \approx 1 - 1.909\frac{1}{\bar{\bar{k}}} + 3.417\left(\frac{1}{\bar{\bar{k}}}\right)^2 - \frac{1}{2\lambda_1}\left(1 - \frac{1}{\bar{\bar{k}}}\right)\zeta\,. \tag{4-33}$$

Placing the numerical value of λ_1 from Eq. (4-30) into Eq. (4-33) gives

$$\bar{\omega}_1 \approx 1-1.909\frac{1}{\bar{k}}+3.417\left(\frac{1}{\bar{k}}\right)^2-0.2667\left(1-\frac{1}{\bar{k}}\right)\zeta\ . \tag{4-34}$$

Now, the approximate expression for lateral mode-1 quality factor for the case $\zeta << 1$ and $1/\bar{k} << 1$ can be obtained by substituting Eq. (4-33) into Eq. (4-21) to yield

$$Q_1 \approx \frac{\lambda_1}{\zeta}\sqrt{1-1.91\frac{1}{\bar{k}}+\frac{1.5}{\lambda_1}\zeta}\ . \tag{4-35}$$

Here the terms of order 2 or higher in ζ or in $1/\bar{k}$, including their product, have been ignored. After binomial expansion, Eq. (4-35) reduces to

$$Q_1 \approx \frac{\lambda_1}{\zeta}\left(1-0.95\frac{1}{\bar{k}}+\frac{0.75}{\lambda_1}\zeta\right)\ . \tag{4-36}$$

The last term is insignificant in many practical cases, in which case it may be ignored, resulting in

$$Q_1 \approx \frac{\lambda_1}{\zeta}\left(1-0.95\frac{1}{\bar{k}}\right)\ , \tag{4-37}$$

which clearly and concisely indicates the main influences of the Stokes-type fluid resistance and the support compliance on the viscous quality factor.

It is to be noted that the difference between Eqs. (4-36) and (4-37) is simply an additive constant of 0.75 and, thus, this difference is only significant for low quality factors. But in most practical cases and in this present study, large values of quality factors are of primary interest and, thus, Eq. (4-37) can be used without significant error. Also, the current theoretical model underestimates the resistance offered by the viscous fluid and therefore overestimates the actual quality factor values. Therefore, using Eq. (4-

37) helps to compensate to some extent for the error due to the underestimation of viscous dissipation in the fluid.

4.3 Solution for the In-Fluid Forced-Vibration Response via Harmonic Relative Rotation near Support in Lateral Flexure

Presented in this section is the derivation of the exact solution for the in-fluid, forced-vibration, lateral flexural response caused by a harmonic relative rotation near the support. The BVP governing this problem is summarized in Section 3.5.2 and is explicitly described by Eqs. (3-27) and (3-28a-d). For convenience this BVP, involving a partial differential equation, is restated here:

$$\bar{y}''''(\xi,\tau)+\lambda_1^4\left(1+\frac{\zeta}{\lambda_1}\frac{1}{\sqrt{\bar{\omega}}}\right)\ddot{\bar{y}}(\xi,\tau)+\lambda_1^3\zeta\sqrt{\bar{\omega}}\,\dot{\bar{y}}(\xi,\tau)=0\,, \qquad (4\text{-}38)$$

$$\bar{y}(0,\tau)=0\ , \qquad (4\text{-}39a)$$

$$\bar{y}'(0,\tau)-\frac{\bar{y}''(0,\tau)}{\bar{k}}=\theta_0 e^{i\bar{\omega}\tau}\ , \qquad (4\text{-}39b)$$

$$\bar{y}''(1,\tau)=0\ , \qquad (4\text{-}39c)$$

$$\bar{y}'''(1,\tau)=0\,. \qquad (4\text{-}39d)$$

Once this BVP is solved, i.e., after the displacement response is determined, theoretical frequency response plots may be generated, from which the resonant frequencies and quality factors may be extracted. The quality factors may be determined, for example, by using the -3dB bandwidth method [e.g., Meirovitch, 2001].

The solution to Eqs. (4-38) through (4-39a-d) is sought in the form

$$\bar{y}(\xi,\tau)=\phi(\xi)e^{i\bar{\omega}\tau}\ , \qquad (4\text{-}40)$$

where $\phi(\xi)$ is the shape of the vibrating beam under an imposed complex harmonic relative rotation near the support and $\bar{\omega}$ is the dimensionless form of the specified exciting frequency, ω, and, thus, also the dimensionless frequency of the steady-state response, i.e.,

$$\bar{\omega} = \frac{\omega}{\omega_0}. \tag{4-41}$$

Substituting Eq. (4-40) into Eqs. (4-38) and (4-39a-d) results in the following BVP, which now involves an ordinary differential equation:

$$\phi''''(\xi) - \alpha^4 \phi(\xi) = 0, \tag{4-42}$$

$$\phi(0) = 0, \tag{4-43a}$$

$$\phi'(0) - \frac{\phi''(0)}{\bar{k}} = \theta_0, \tag{4-43b}$$

$$\phi''(1) = 0, \tag{4-43c}$$

$$\phi'''(1) = 0 \quad . \tag{4-43d}$$

where the known complex parameter α is related to the fluid resistance parameter and the normalized forcing frequency through

$$\alpha^4 \equiv \lambda_1^4 \left(1 + \frac{\zeta}{\lambda_1} \frac{1}{\sqrt{\bar{\omega}}}\right) \bar{\omega}^2 - i \lambda_1^3 \zeta \bar{\omega}^{3/2}. \tag{4-44}$$

The general solution of Eq. (4-42) may be written as

$$\phi(\xi) = A_1 \cos \alpha\xi + A_2 \sin \alpha\xi + A_3 \cosh \alpha\xi + A_4 \sinh \alpha\xi, \tag{4-45}$$

where A_i, i =1, 2, 3, 4, are as yet undetermined constants. Imposing BCs from Eqs. (4-43a-d) on Eq. (4-45) gives the following complex shape of the vibrating beam under an imposed complex harmonic relative rotation, $\theta_0 e^{i\omega t}$, near the support:

$$\phi(\xi) = \frac{\theta_0}{2}\left[\frac{\left(Cs-cS\right)\left(\cosh\alpha\xi-\cos\alpha\xi\right)+\left(1+Cc-Ss\right)\sinh\alpha\xi+\left(1+Cc+Ss\right)\sin\alpha\xi}{\alpha\left[1+Cc-\frac{\alpha}{\overline{k}}\left(Cs-cS\right)\right]}\right], \quad (4\text{-}46)$$

where

$$c \equiv \cos\alpha\,,\ C \equiv \cosh\alpha\,,\ \ s \equiv \sin\alpha\,,\ \ S \equiv \sinh\alpha\,. \qquad (4\text{-}47\text{a-d})$$

In practical sensing applications the beam response may be monitored in different ways. Two of the most common methods of measuring response are optical (laser) and piezorestive detection. In the optical method the total tip deflection or tip slope is monitored (e.g., using a laser), while in the piezoresistive method piezoresistive elements near the support monitor the bending strain that results from the vibration. Thus, to account for both types of detection methods, the amplitudes of the both the tip displacement and the bending strain at the root of the beam will be of particular interest in this study and results in terms of both of these quantities will therefore be presented.

The complex (normalized) displacement amplitude at the tip is obtained by evaluating Eq. (4-46) at $\xi = 1$:

$$\phi(1) = \theta_0\left[\frac{s+S}{\alpha\left[1+Cc-\frac{\alpha}{\overline{k}}\left(Cs-cS\right)\right]}\right]. \qquad (4\text{-}48)$$

The modulus of this quantity may be scaled by its quasi-static value, which corresponds to a slowly applied harmonic rotation at the support, $\phi_{static}(1) \equiv \theta_0$, thereby resulting in the following “dynamic magnification factor” for tip displacement, DMF_{tip} :

$$DMF_{tip} = \frac{\left|\phi(1)\right|}{\phi_{static}(1)} = \frac{\left|\phi(1)\right|}{\theta_0} = \left|\frac{s+S}{\alpha\left[1+Cc-\frac{\alpha}{\overline{k}}\left(Cs-cS\right)\right]}\right|. \qquad (4\text{-}49)$$

The maximum bending strain $\varepsilon_{max}(x,t)$ at any x and t on the beam is given by

$$\varepsilon_{max}(x,t)=\frac{\sigma_{max}(x,t)}{E}, \tag{4-50}$$

where $\sigma_{max}(x,t)$ is the maximum bending stress at position *x* at time *t*, and can be related to the curvature at (*x*, *t*) by

$$\sigma_{max}(x,t)=\frac{M_{max}(x,t)}{I}\frac{b}{2}=\frac{EIy''(x,t)}{I}\frac{b}{2}. \tag{4-51}$$

Substituting Eq. (4-51) into Eq. (4-50) results in

$$\varepsilon_{max}(x,t)=y''(x,t)\frac{b}{2}. \tag{4-52}$$

Equation (4-52) can be written in terms of dimensionless deflection and dimensionless coordinates ξ and τ as

$$\varepsilon_{max}(\xi,\tau)=\overline{y}''(\xi,\tau)\frac{b}{2L}. \tag{4-53}$$

Using Eqs. (4-40) and (4-53), the maximum bending strain at the root of the beam is

$$\varepsilon_{max}(0,\tau)=\frac{b}{2L}\phi''(0)\,e^{i\varpi\tau}, \tag{4-54}$$

so that

$$\varepsilon_{max,\ root}\equiv\frac{b}{2L}\left|\phi''(0)\right| \tag{4-55}$$

is the amplitude of the maximum bending strain at the root. Substituting Eq. (4-46) into Eq. (4-55) results in

$$\overline{\varepsilon}_{max,\ root}\equiv\frac{\varepsilon_{max,\ root}}{\theta_0 b/2L}=\frac{\left|\phi''(0)\right|}{\theta_0}=\left|\frac{\alpha\left(Cs-cS\right)}{\left[1+Cc-\frac{\alpha}{\overline{k}}\left(Cs-cS\right)\right]}\right|, \tag{4-56}$$

where $\bar{\varepsilon}_{max,\, root}$ is the normalized amplitude of the maximum bending strain at the root of the beam.

Equation (4-49) represents the normalized beam response as measured by the tip displacement amplitude (e.g., an optical method) and Eq. (4-56) corresponds to the normalized beam response as detected by monitoring the bending strain amplitude at the root of the beam (e.g., by piezoresistive detection). The dependence of these results on the exciting frequency will be used in Chapter 6 to determine the resonant frequencies and quality factors for a microcantilever beam excited by a harmonic relative rotation near the support. More specifically, the frequency response plots (plots of normalized response vs. normalized exciting frequency) for tip displacement amplitude and bending strain amplitude at the root will be generated and the resonant frequencies shall be extracted as the exciting frequencies at which the respective response quantities attain their relative maximum values. Then one may use a resonant frequency value and the corresponding frequency response plot to extract the associated quality factor using the -3dB bandwidth method. Note that the frequency response plots and the associated resonant frequency and quality factor values need not be the same for the two different types of output signals that will be considered.

CHAPTER 5
QUANTIFICATION OF DIMENSIONLESS SUPPORT STIFFNESS, DIMENSIONLESS RESONANT FREQUENCY AND QUALITY FACTOR IN TERMS OF SYSTEM PARAMETERS

5.1 Introductory Remarks

The main objective of this dissertation is to study the effects of support compliance on the resonant behavior of lateral-mode microcantilevers operating in viscous fluids. For this purpose, the BVPs and their solutions for different cases were discussed in Chapters 3 and 4 with dimensionless rotational stiffness of the support $\bar{k}$ (or compliance $1/\bar{k}$) as a “specified” system parameter. However, to obtain the results for the natural and resonant frequencies and quality factors for a particular practical application, a rational means of determining the value of this parameter is needed. This chapter deals with the quantification of $\bar{k}$ in terms of cantilever dimensions, i.e., *L*, *b* and *h*. In order to quantify the rotational stiffness of the support, finite element analysis (FEA) will be used. Several three-dimensional (3-D) finite element analyses will be performed using the commercially available ANSYS 13.0 software package [ANSYS Inc., 2013] and the results will be used to determine an appropriate analytical expression for $\bar{k}$ and, thus, for $1/\bar{k}$. Then the expression for $1/\bar{k}$ will be used in conjunction with the results for dimensionless frequencies and quality factors obtained in Ch. 4 to obtain analytical expressions for $\bar{\omega}_1$ and Q_1 in terms of system parameters.

The chapter begins with the general description of the 3-D finite element modeling/analysis approach taken in ANSYS, including how the rotational support stiffness is defined through the concept of work equivalence so that its value may be extracted from the ANSYS results. Then the Buckingham Pi Theorem [e.g., Fox and McDonald, 1993] is used to obtain the possible dimensionless relationships between k and the system parameters. Based on those results, a parametric study is then performed using ANSYS, the results of which are used in conjunction with the dimensional analysis in order to rationally deduce a simple analytical expression for the dimensionless rotational stiffness and compliance, $\bar{k}$ and $1/\bar{k}$, respectively. Finally, the stiffness/compliance expression permits one to convert the previously obtained analytical expressions for $\bar{\omega}_1$ and Q_1 to formulae expressed explicitly in terms of the fundamental system parameters.

5.2 3-D Finite Element Modeling Approach

This section will include a statement of the assumptions on which the FE model is based, a brief description of the ANSYS modeling/analysis procedure, and an explanation of how rotational support stiffness is defined and calculated using concept of work equivalence.

5.2.1 Modeling Assumptions

In order to perform 3-D finite element modeling and analysis within ANSYS, the following assumptions are made:

1) The cantilever beam and the "support block" are made of the same material and that material is elastic and isotropic.
2) The SOLID187 element, which is a higher-order, 3-D, 10-node tetrahedral element, will be used to model both the beam and the support.

3) The support block is assumed to be sufficiently large in comparison to the beam dimensions so that it is, for all practical purposes, “infinite” in that its dimensions do not affect the support stiffness.
4) The length of the beam is large enough so that it has no influence on the rotational stiffness of the support.
5) The outer surfaces of the support block that are not adjacent to the supported end of the beam are considered fixed; however, by virtue of assumption (3), the details of the support conditions on these surfaces should not have an appreciable effect on the characteristics of the support deformation.
6) The beam is assumed to be loaded with a static bending moment applied at the unsupported end of the cantilever. This moment is distributed in the form of a linear normal stress over the end cross-section. The orientation of this moment is such that it will cause the beam to bend in the lateral direction.
7) Since the geometry and the loading exhibit anti-symmetry, only half of the geometry will be modeled. (See Fig. 5-1.)
8) In order to perform the ANSYS analysis, the support block and cantilever dimensions, material properties, and the applied moment magnitude are to be specified. In this analysis following numerical values will be used for aforementioned quantities:

   Modulus of elasticity of material, $E = 0.1\ \mathrm{N}/\mu\mathrm{m}^2 = 100$ GPa;

   Poisson’s ratio, $\nu = 0$, 0.1, 0.2, 0.25, 0.3, and 0.4;

   Support block dimension: length=$1000\,\mu\mathrm{m}$, width=thickness= $500\,\mu\mathrm{m}$;

   Beam dimensions: L=$300\,\mu\mathrm{m}$, b= $(10, 20, 50, 100, 200)\,\mu\mathrm{m}$, h=$10\,\mu\mathrm{m}$;

Applied moment magnitude: M=0.01 $\mathrm{N\,\mu m}$.

5.2.2 ANSYS Modeling and Analysis Procedure

Three-dimensional models of one-half of the beam-support geometry were created using SOLID187 elements. In all models the support block dimensions and the length and thickness of the cantilever were kept constant and only the width of the cantilever and Poisson's ratio were varied. Figure 5-1a is an example of the 3-D ANSYS model and Fig. 5-1b represents the top view of the model. The models were meshed in such a way that the local meshing of elements on or near the interface of beam and support was very fine relative to the mesh farther away from this region. This is because of the expected stress concentration in this region of sudden change in geometry and the fact that the accuracy of the support stiffness calculation will be dependent on the accuracy of the displacement and stress values at the interface. (See section 5.2.3.) The mesh fineness was increased until the desired result for $\bar{k}$ was accurate to at least two significant figures. It is to be noted that, in those cases in which the beam was especially thin (relative to the beam width), there were a few element size warnings while meshing within ANSYS; however, such warnings did not appear in the vast majority of the meshes created.

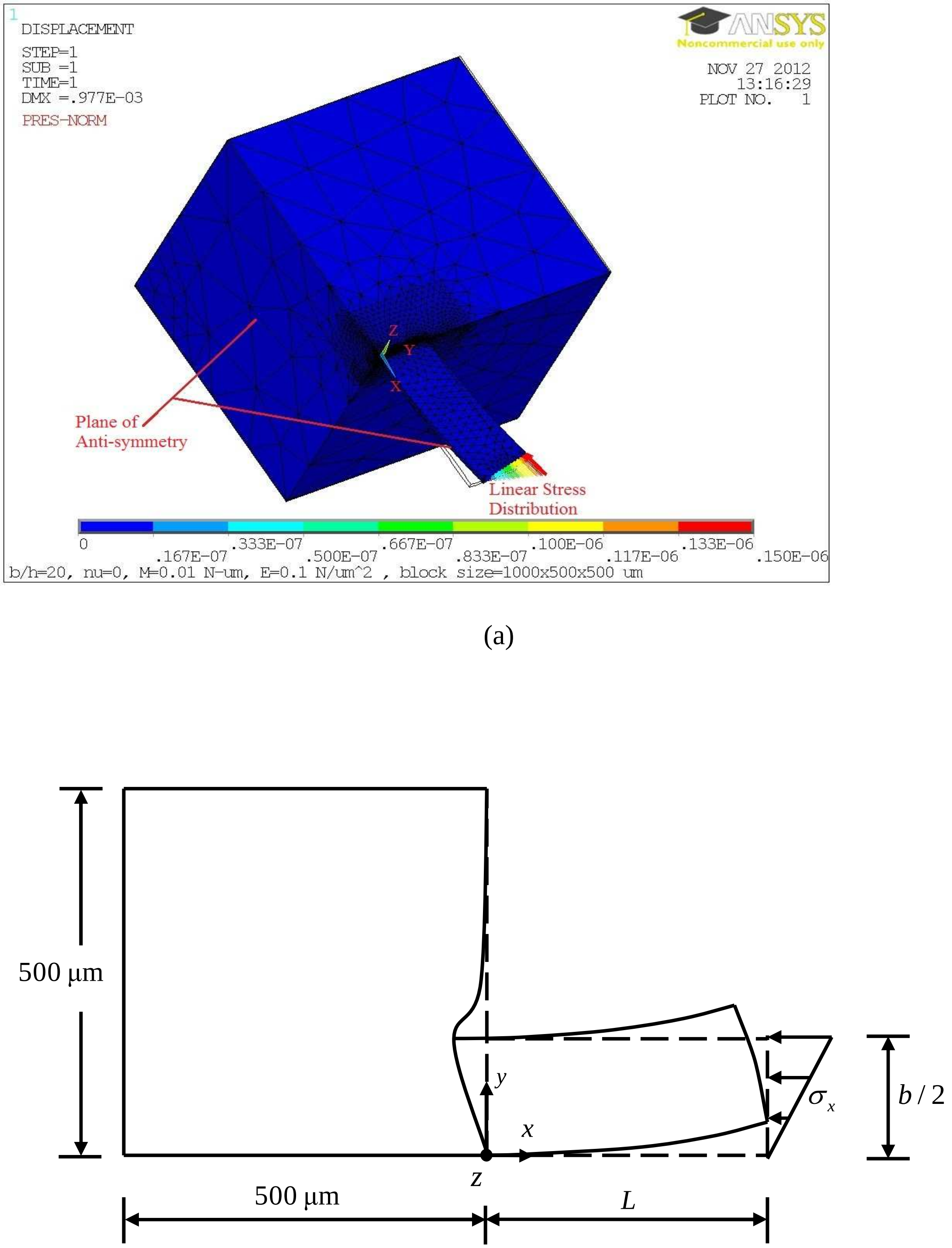

(a)

(b)

Figure 5-1: Finite-element model showing coordinate axes, dimensions, applied stress and deflected shape: (a) 3-D model, (b) schematic of top view.

At the loaded face, the specified normal stress distribution σ_x is equivalent to a resultant moment *M* being applied over the entire cross-section. The maximum normal stress on the loaded face is related to the resultant moment through

$$\sigma_x = \pm \frac{M}{I} \bar{c} \ , \tag{5-1}$$

where $I = hb^3/12$ is the moment of inertia of the total beam cross-section about the neutral axis ("strong" axis) and $\bar{c} = b/2$ is the distance from the neutral axis to the "extreme fibers."

On the plane of anti-symmetry, appropriate anti-symmetry boundary conditions apply:

$$\sigma_y = 0\, ,\ u_x = 0\, ,\ u_z = 0\, , \tag{5-2}$$

where the subscripts refer to the reference frame shown in Fig. 5-1. Also, the three hidden faces of the support block in Fig. 5.1a are fixed ($u_x = u_y = u_z = 0$).

After the application of the load and displacement boundary conditions, a linear elastic analysis of the models was performed using ANSYS. Via postprocessing of the results, the work done by the bending stress σ_x at the beam-support interface was determined and, as specified in the next section, used to calculate the support stiffness as defined using the concept of equivalent work.

5.2.3 Determination of Effective Support Stiffness Using the Concept of Work Equivalence

The work done by the bending stress σ_x in displacing the support at the beam-support interface may be considered to be equal to the resultant moment on the interface (*M*, by statics on the beam) acting through an “effective rotation”:

$$W = 2W_{FEM} = 2\iint_{BSI} \sigma_x u_x dA \equiv M\theta_e \quad , \tag{5-3}$$

in which “BSI” refers to the beam-support interface of the finite-element model, θ_e is the effective rotation of the beam-support interface, and the factor 2 is present so that $W = 2W_{FEM}$ represents the work over the *total* interface, only half of which is modeled in ANSYS. [The notation W_{FEM} refers to the value of work obtained from the finite-element model. It is defined by the integral appearing in Eq. (5-3), which is evaluated numerically within ANSYS.] Using the effective rotation to define the rotational support stiffness k yields

$$k = \frac{M}{\theta_e} . \tag{5-4}$$

Using Eq. (5-3), one may eliminate the effective rotation from Eq. (5-4) to obtain the support stiffness explicitly in terms of the work calculated within the finite-element model:

$$k = \frac{M^2}{2W_{FEM}} . \tag{5-5}$$

Despite the appearance of *M* in the numerator of Eq. (5-5), the stiffness does *not* depend on the value of *M* that is specified in the model, since the linearity of the model dictates that the work appearing in the denominator will also be proportional to M^2.

5.3 Dimensional Analysis for the Functional Relationship Between the Rotational Support Stiffness and the System Parameters

In this section the Buckingham Pi Theorem [e.g., Fox and McDonald, 1993] is used to obtain the possible dimensionless relationships between $\bar{k}$ and the system parameters. Of these, the most convenient relationship will be chosen and used in Ch. 6 in conjunction with the results of Ch. 4 to relate the dynamic response of the elastically supported cantilever to the geometric and material parameters of the system.

Dimensional analysis performed by applying the Buckingham Pi Theorem [e.g., Fox and McDonald, 1993] to the present problem (Appendix B) results in the following candidate forms for the dimensionless relationship among rotational support stiffness, system geometry, and system material properties:

$$\frac{k}{Eb^3} = f_1\left(\frac{h}{b}, \nu\right), \tag{5-6a}$$

$$\frac{k}{Eh^3} = f_2\left(\frac{h}{b}, \nu\right), \tag{5-6b}$$

$$\frac{k}{Ehb^2} = f_3\left(\frac{h}{b}, \nu\right), \tag{5-6c}$$

$$\frac{k}{Eh^2b} = f_4\left(\frac{h}{b}, \nu\right). \tag{5-6d}$$

These four candidate forms are equivalent representations, but they involve different dimensionless functions, each dependent on the cross-section’s aspect ratio, h/b, and the Poisson’s ratio, ν, of the device material. In the following section the most convenient of these four will be selected to yield the simplest analytical expression based on curve-fitting the results of an FEA parametric study to the forms listed in Eqs. (5-6a-d).

5.4 Parametric Study for Rotational Stiffness of Support Based on 3-D Finite Element Analysis

For a particular beam geometry the rotational stiffness of the support, as defined in the Section 5.2.3, may be obtained by performing a finite element analysis (summarized in Section 5.2.2) and substituting the value of the interface work from the analysis into Eq. (5-5). Performing several analyses of this type enables one to determine numerically how normalized support stiffness depends on system parameters. The results of such a parametric study are shown in Table 5-1, in which the numerical values of rotational support stiffness k for different aspect ratios (h/b) and different Poisson's ratios (ν) are listed.

It can be concluded from the numerical results that k decreases significantly with an increase in the h/b ratio, i.e., with a decrease in b for a fixed h. Since h is fixed in the models, smaller b results in a smaller beam-support interface area and, thus, for a given transferred moment, a larger rotation of the support resulting in smaller k . The table also indicates that the dependence of k on ν is quite weak, with the trend (increasing or decreasing) depending on the aspect ratio.

h/b	***ν***	**W_{FEM} (N-µm)**	***k*** **(N-µm/rad)**
0.05	0	2.265E-09	22073
	0.1	2.300E-09	21735
	0.2	2.320E-09	21555
	0.25	2.323E-09	21521
	0.3	2.323E-09	21525
	0.4	2.310E-09	21646
0.1	0	1.213E-08	4121.9
	0.1	1.235E-08	4049.8
	0.2	1.250E-08	4000.9
	0.25	1.255E-08	3984.4
	0.3	1.258E-08	3973.2
	0.4	1.261E-08	3966.2
0.2	0	6.089E-08	821.19
	0.1	6.183E-08	808.64
	0.2	6.248E-08	800.20
	0.25	6.270E-08	797.43
	0.3	6.284E-08	795.61
	0.4	6.290E-08	794.94
0.5	0	4.696E-07	106.47
	0.1	4.731E-07	105.69
	0.2	4.734E-07	105.62
	0.25	4.723E-07	105.86
	0.3	4.704E-07	106.29
	0.4	4.637E-07	107.83
1	0	2.090E-06	23.918
	0.1	2.095E-06	23.870
	0.2	2.080E-06	24.042
	0.25	2.065E-06	24.219
	0.3	2.044E-06	24.462
	0.4	1.985E-06	25.192

Table 5-1: Rotational stiffness of support based on 3-D finite element analysis with $E = 0.1$ N/µm^2, $L = 300$ µm, and $h = 10$ µm.

5.5 Determination of Analytical Expressions for Dimensionless Rotational Stiffness of Support

After obtaining the numerical results for the rotational stiffness of the support, k , using work equivalence and 3-D finite-element modeling as explained in the preceding sections, an analytical expression for k in terms of the problem parameters (beam dimensions and material properties) may be obtained. Using the numerical values for k from Table 5-1 and the corresponding values of problem parameters, the dimensionless functions $f_i\left(h/b,\ \nu\right)$ in Eqs. (5-6a-d) can be determined and plotted. Figures 5-2a-d show the plots of these dimensionless functions plotted versus the aspect ratio h/b for fixed values of Poisson's ratio over the ranges considered. From the plots it is obvious that the dependence on ν is weak, as observed earlier in Table 5-1. Also, the plots for the dimensionless function in Fig. 5-2a, i.e., $f_1\left(h/b,\ \nu\right)=k/Eb^3$, are nearly linear and, for this reason, the form of Eq. (5-6a) will be chosen to characterize the desired dimensionless relationship. In addition, since the dependence on ν is very weak, only the plot for $\nu=0.25$ will be considered in determining an analytical form of this relationship. The plot in Fig. 5-2a for $\nu=0.25$ is fitted by a straight line, as shown in Fig. 5-3, to obtain the following linear equation relating k/Eb^3 to h/b:

$$\frac{k}{Eb^3}=0.2258\frac{h}{b}+0.0174\,. \tag{5-7}$$

Thus, the expression for the (dimensional) rotational stiffness of the support is

$$k=Eb^3\left(0.2258\frac{h}{b}+0.0174\right). \tag{5-8}$$

Now the relative rotational stiffness of the support with respect to the beam's flexural stiffness, as defined in Chapter 3 and given by Eq. (3-19), is

$$\bar{k}\equiv\frac{kL}{EI}\,. \tag{5-9}$$

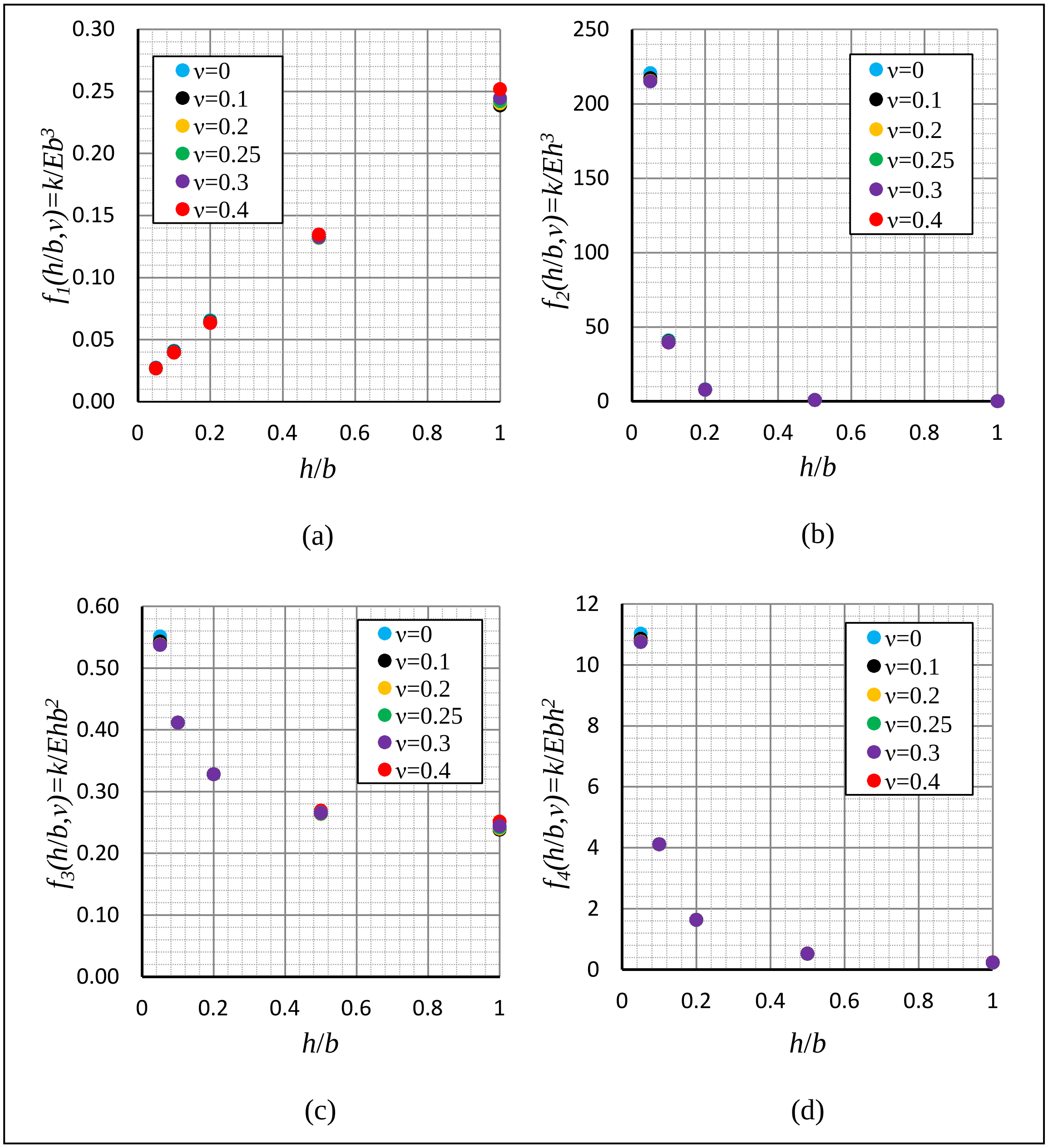

(a) (b) (c) (d)

Figure 5-2: Values of dimensionless functions $f_i\,(h/b,\ \nu)$ for in-plane static bending of microcantilevers of rectangular cross-section: (a) Eq. (5-6a), (b) Eq. (5-6b), (c) Eq. (5-6c), (d) Eq. (5-6d). (Results are based on 3-D FEA results for rotational support stiffness calculation using the work equivalence method.)

Substituting Eq. (5-9) into Eq. (5-8) with $I = hb^3/12$ results in $\bar{k}$ explicitly in terms of system geometry:

$$\bar{k} = \frac{L}{b}\frac{b}{h}\left(0.2088 + \frac{2.710}{b/h}\right), \tag{5-10}$$

The corresponding compliance, $1/\bar{k}$, becomes

$$\frac{1}{\bar{k}} = \frac{1}{\frac{L}{b}\frac{b}{h}\left(0.2088 + \frac{2.710}{b/h}\right)} \tag{5-11}$$

Equations (5-10) and (5-11) are restricted to the range $0.05 \le h/b \le 1$ since the fit (Fig. 5-3) was performed over this range.

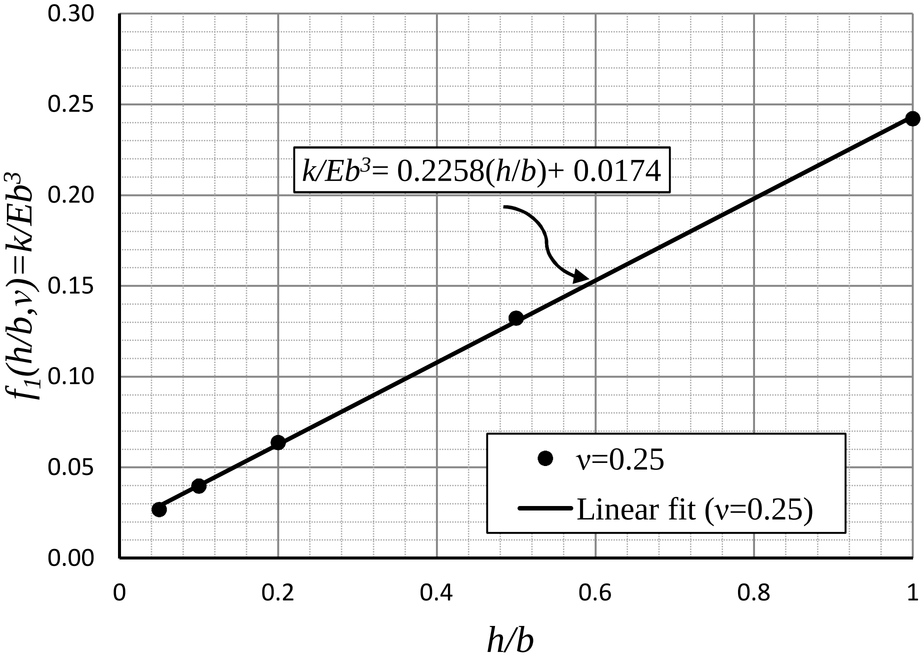

Figure 5-3: Linear fit of dimensionless function k/Eb^3 vs. h/b for $\nu = 0.25$, $0.05 \le h/b \le 1$.

5.6 Determination of Analytical Expressions for Dimensionless Frequency and Quality Factor in Terms of System Parameters

Having determined an analytical expression for $1/\bar{k}$, the approximate expressions for the dimensionless natural frequency and quality factor for the first lateral mode, derived in Ch. 4, can now be expressed explicitly in terms of system parameters. The approximate expressions [Eqs. (4-34) and (4-37)] from Ch. 4 are

$$\bar{\omega}_1 \approx 1 - 1.909\frac{1}{\bar{k}} + 3.417\left(\frac{1}{\bar{k}}\right)^2 - 0.2667\left(1 - \frac{1}{\bar{k}}\right)\zeta\,, \qquad (5\text{-}12)$$

$$Q_1 \approx \frac{1.8751}{\zeta}\left(1 - 0.95\frac{1}{\bar{k}}\right). \qquad (5\text{-}13)$$

The fluid resistance parameter, ζ, in Eq. (3-15a) can be written in the form

$$\zeta = 2.632\sqrt{\frac{L_0}{h}}\,\frac{L}{b}\sqrt{\frac{b}{h}}\,, \qquad (5\text{-}14)$$

where

$$L_0 \equiv \sqrt{\frac{\eta^2 {\rho_f}^2}{E {\rho_b}^3}} \qquad (5\text{-}15)$$

has unit of length and may be interpreted as a "characteristic material length" which is constant for a given fluid and beam material. Substituting Eq. (5-11) into Eqs. (5-12) and (5-13) and making use of Eq. (5-14) results in,

$$\begin{aligned}\bar{\omega}_1 \approx 1 &- \frac{1.909}{\frac{L}{b}\frac{b}{h}\left(0.2088 + \frac{2.710}{(b/h)}\right)} + \frac{3.417}{\left(\frac{L}{b}\frac{b}{h}\left(0.2088 + \frac{2.710}{(b/h)}\right)\right)^2} \\ &- 0.7019\left(1 - \frac{1}{\frac{L}{b}\frac{b}{h}\left(0.2088 + \frac{2.710}{(b/h)}\right)}\right)\sqrt{\frac{L_0}{h}}\,\frac{L}{b}\sqrt{\frac{b}{h}}\end{aligned}\,, \qquad (5\text{-}16)$$

$$Q_1 \approx \frac{0.7124}{\sqrt{\frac{L_0}{h}}\,\frac{L}{b}\sqrt{\frac{b}{h}}}\left(1 - \frac{0.95}{\frac{L}{b}\frac{b}{h}\left(0.2088 + \frac{2.710}{(b/h)}\right)}\right). \qquad (5\text{-}17)$$

Equations (5-16) and (5-17) are valid for

$$1 \le \frac{b}{h} \le 20 \ , \tag{5-18a}$$

$$0 \le \frac{1}{\bar{k}} = \frac{1}{\frac{L}{b}\frac{b}{h}\left(0.2088 + \frac{2.710}{(b/h)}\right)} \le 0.15 \quad \text{or,} \quad \frac{L}{b} \ge \frac{1}{0.15\frac{b}{h}\left(0.2088 + \frac{2.710}{(b/h)}\right)} \ , \tag{5-18b}$$

$$\zeta = 2.632\sqrt{\frac{L_0}{h}}\frac{L}{b}\sqrt{\frac{b}{h}} << 1 \ . \tag{5-18c}$$

Similarly, the displacement response due to forced vibration via relative rotation near the support, as described in Ch. 4 by Eqs. (4-49) and (4-56), can be rewritten in terms of system parameters using Eqs. (5-11) and (5-14) and then the corresponding results for resonant frequency and quality factor can also be determined in terms of system parameters. Those results are not listed explicitly here; however, in most cases of practical interest we expect that the analytical formulae based on free vibration – Eqs. (5-16) and (5-17) – will give excellent approximations to the corresponding resonant quantities associated with forced vibration of the model.

The analytical results obtained in this chapter for natural frequency and quality factor for the first lateral mode of vibration will serve as the basis for a parametric study to be performed in the following chapter. The parametric study of the first lateral mode resonant frequency and quality factor for the forced vibration case will also be performed and discussed in Ch. 6.

CHAPTER 6
NUMERICAL RESULTS AND DISCUSSION

6.1 Introductory Remarks

In this chapter a parametric study based on the results obtained in Chs. 4 and 5 is presented and discussed. First the results for the in-fluid free-vibration case, namely, the natural frequencies, quality factors, and mode shapes are presented. This is followed by the results for the in-fluid forced-vibration case for an imposed relative rotation near the support. These include frequency spectra for the response amplitude, resonant frequencies, quality factors, and vibrational shapes. For the forced-vibration case, the results are presented for both the tip displacement response and the bending strain response at the root. In addition the results for natural/resonant frequencies and quality factors are compared to experimental data. This chapter quantifies the impact of support compliance, fluid resistance and microcantilever dimensions on the dynamic response of lateral-mode microcantilevers.

6.2 Parametric Study: Free Vibration with Stokes-Type Fluid Resistance

In this section the parametric study of the natural frequencies, quality factors and mode shapes for the case of in-fluid free vibration are presented. The effects of support compliance and fluid resistance on natural frequencies and quality factors are presented for multiple lateral modes of vibration using results from Ch. 4. Then the results of Ch. 5 are used to relate the support compliance to the beam dimensions so that a detailed study may be performed to show how the natural frequency and mode shape of the fundamental lateral mode depend on the device dimensions. The fundamental mode is the focus since it is the most easily excited.

6.2.1 Natural Frequencies

The impact of support compliance, $1/\bar{k}$, fluid resistance, ζ, and beam geometry on the natural frequencies is examined in this section. The parametric study of the natural frequencies, obtained by solving the 5th-degree frequency equation given by Eq. (4-18), in terms of $1/\bar{k}$ and ζ for the first three modes of in-fluid lateral vibration is presented in Fig. 6-1. This figure clearly indicates, as expected, that the natural frequencies decrease with increases in support compliance, $1/\bar{k}$, and fluid resistance, ζ. For the range of ζ considered, the natural frequency varies almost linearly in ζ but nonlinearly in $1/\bar{k}$. Also, the curves for different $1/\bar{k}$ are parallel to each other indicating that the effects of support compliance and fluid resistance on natural frequency are somehow independent of each other. For the first mode and for the ranges of support compliance and fluid resistance considered, the support effects may cause up to a 21% drop in natural frequency, while the fluid resistance may cause up to a 25% drop in natural frequency. For second mode the relative change in natural frequency due to support effects and fluid effects might reach 16% and 11% respectively over the parameter ranges considered. For mode 3 the drop in natural frequency may reach 12% due to support effects and 7% due to fluid effects. As mentioned earlier, since the first mode of lateral vibration is the most easily excited lateral mode and thus the most practical lateral mode for sensors applications, the relative decrease in natural frequency due to support compliance and fluid resistance, which could be quite significant as demonstrated here, must be dealt with properly to achieve reasonable theoretical estimates. Conversely, if higher modes can be excited, the adverse effects of support compliance and fluid resistance will be less significant.

Figure 6-2 shows the comparison of the approximate analytical results for the fundamental natural frequency, obtained from Eq. (4-34), with the exact results presented in Fig. 6-1a. Over the practical range of support compliance, $1/\bar{k} \in [0,\ 0.15]$, considered, the approximate results compare quite well with the exact results for small values of ζ. More specifically, for the considered range of support compliance the percentage error of the approximate results is less that 2% for $\zeta \in [0,\ 0.6]$.

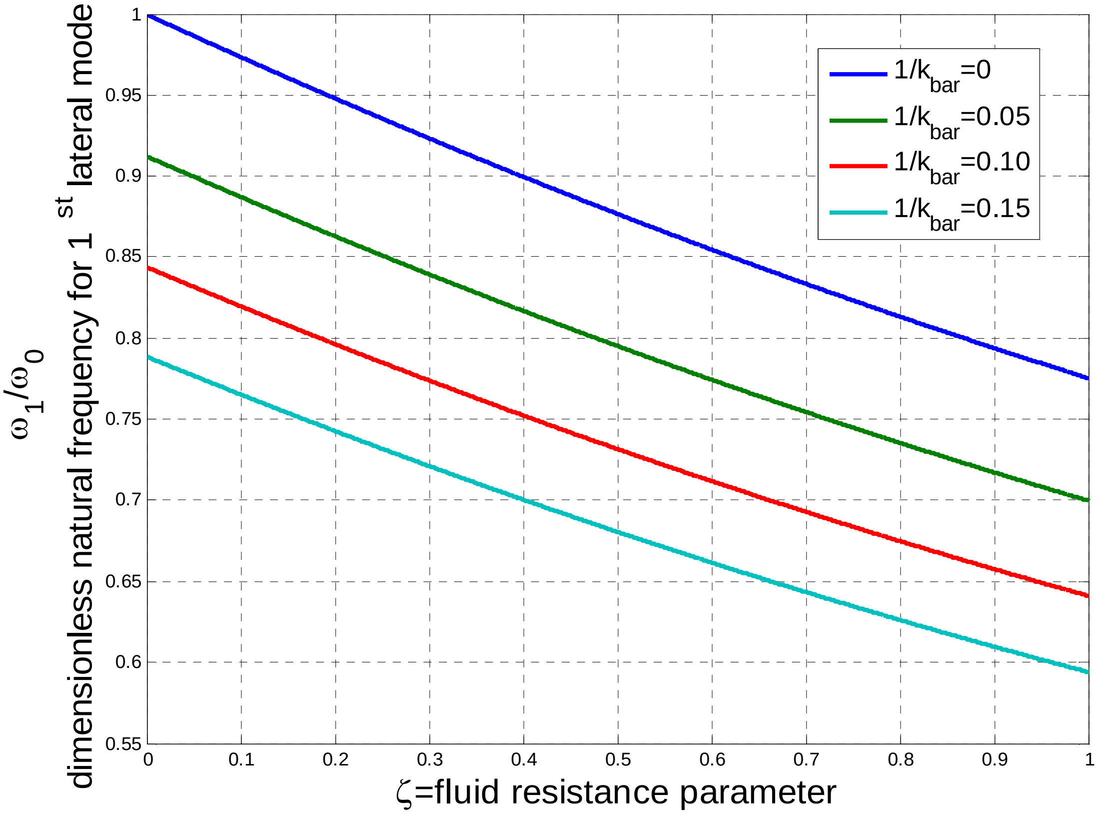

(a)

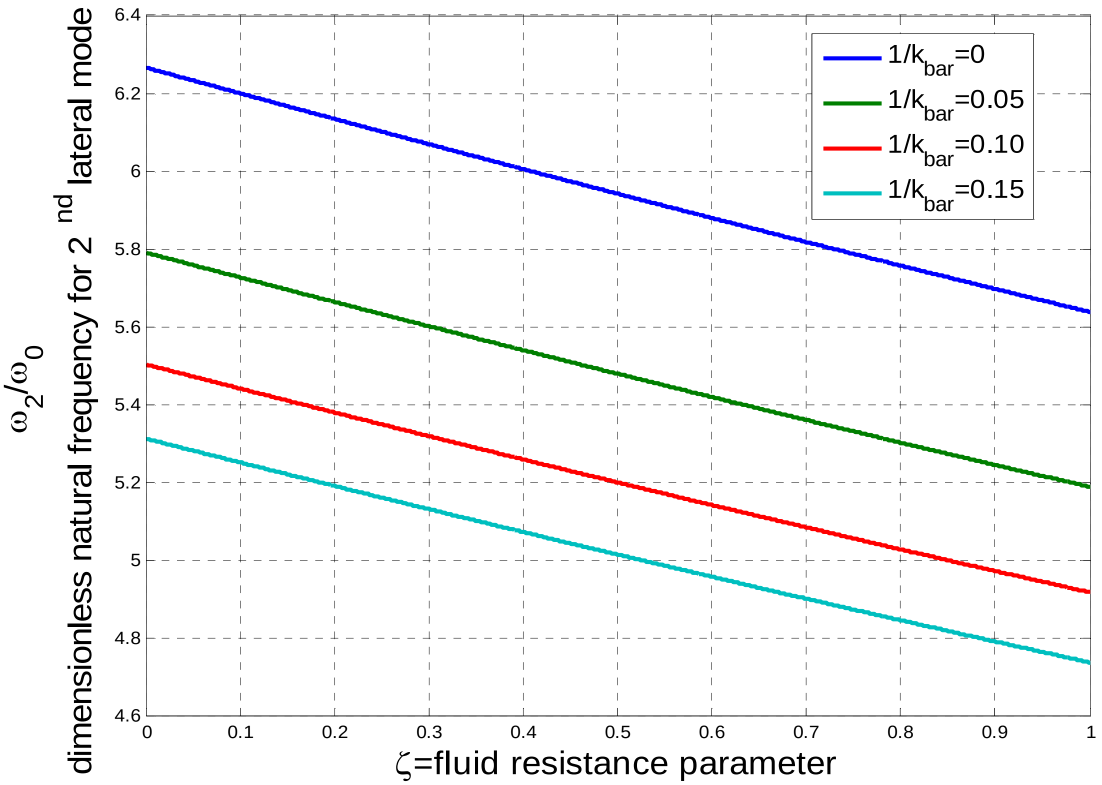

(b)

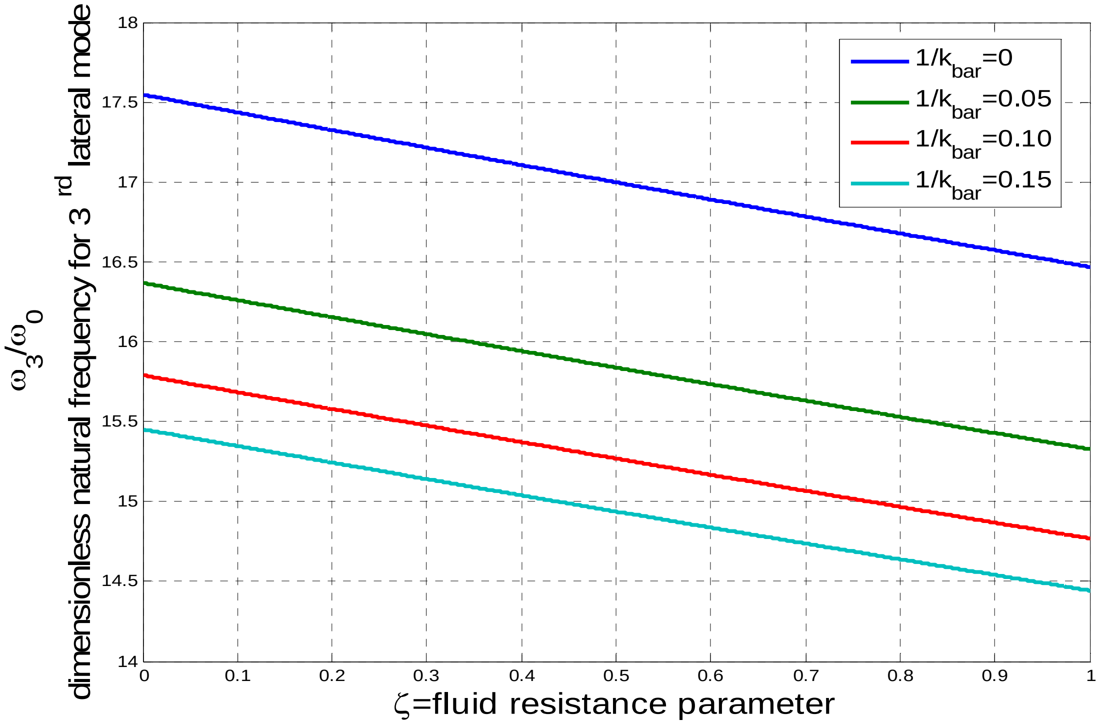

(c)

Figure 6-1: Dimensionless natural frequency for the first three modes of lateral vibration of a microcantilever beam in a viscous fluid [Eq. (4-18)]: (a) first mode, (b) second mode, (c) third mode.

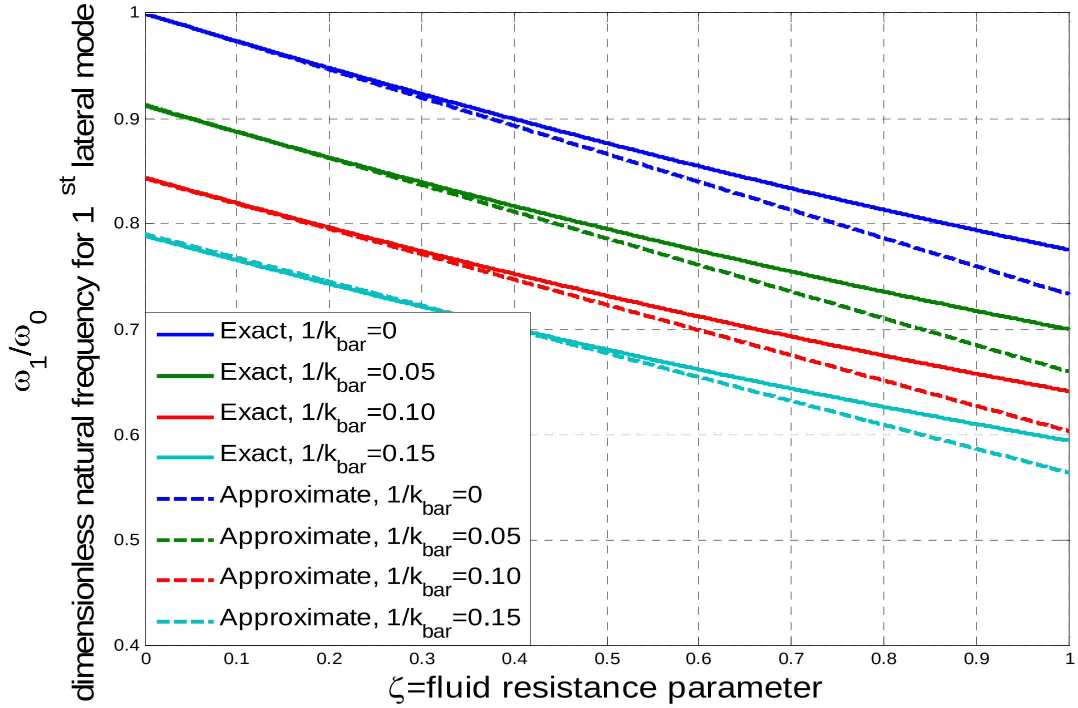

Figure 6-2: Comparison of exact [Eq. (4-18)] and approximate [Eq. (4-34)] dimensionless natural frequency for the fundamental mode of lateral vibration of a microcantilever beam in viscous fluid.

The effects of beam dimensions on the fundamental lateral natural frequency can be studied using the analytical expression given by Eq. (5-16), repeated here for convenience:

$$\bar{\varpi}_1 \approx 1-\frac{1.909}{\frac{L}{b}\frac{b}{h}\left(0.2088+\frac{2.710}{(b/h)}\right)}+\frac{3.417}{\left(\frac{L}{b}\frac{b}{h}\left(0.2088+\frac{2.710}{(b/h)}\right)\right)^2} -0.7019\left(1-\frac{1}{\frac{L}{b}\frac{b}{h}\left(0.2088+\frac{2.710}{(b/h)}\right)}\right)\sqrt{\frac{L_0}{h}}\,\frac{L}{b}\sqrt{\frac{b}{h}}\,, \qquad (6\text{-}1)$$

The second and third terms on the right-hand side of Eq. (6-1) represent the decrease in natural frequency due to support compliance in-vacuum, while the last term involves L_0

and thus represents the decrease in natural frequency due to fluid effects. The support compliance effect is also present in the last term via the negative term inside the parentheses. For Eq. (6-1) to be valid, it must satisfy the limits for the various parameters given by Eqs. (5-18a-c). In particular, the condition that $\zeta << 1$ [Eq. (5-18c)] shall be interpreted as $\zeta \leq 0.6$ as it has already been noted that this constraint ensures no more than a 2% error in the natural frequency (relative to the exact results of the model) over the range of support compliance of interest. This upper limit on ζ, i.e., 0.6, enables Eq. (5-18c) to be rearranged to yield an upper limit on L/b, while a lower limit on L/b is given by Eq. (5-18b). Therefore, the restriction on L/b for Eq. (6-1) to be valid is given by the following inequality:

$$\frac{1}{0.15\dfrac{b}{h}\left(0.2088+\dfrac{2.710}{(b/h)}\right)} \leq \frac{L}{b} \leq \frac{0.2280}{\sqrt{\dfrac{L_0}{h}\dfrac{b}{h}}} . \tag{6-2}$$

In addition the validity of Eq. (6-1) is limited to the range of cross-sectional aspect ratio, b/h, over which the FEA results of Ch. 5 were fitted. This inequality was specified in Eq. (5-18a), repeated here for convenience:

$$1 \leq \frac{b}{h} \leq 20 . \tag{6-3}$$

Examining Eq. (6-1), one sees that, for a given beam material and a specified fluid, L_0 is determined, so that if the thickness of the beam is also specified, the first mode natural frequency may be expressed in terms of L/b and b/h only. These results will be valid provided that L/b and b/h satisfy the constraints given by Eqs. (6-2) and (6-3) listed above. For example, Eq. (6-1) may be applied for the case of beams made of silicon (E=169 GPa and ρ_b=2330 kg/m^3) with thicknesses h = [5, 10, 15, 20] μm vibrating in water (η =0.001 Pa·s, ρ_f =1000 kg/m^3). The results may be cast in the form of the relative decrease in natural frequency due to the effects of support compliance and fluid resistance, which are plotted versus L/b for different b/h ratios in Fig. 6-3. From the figure it is clear that, with an increase in thickness, h, the reduction in natural frequency becomes smaller. This is because the Stokes fluid resistance parameter decreases with an increase in h, which is manifested through the $\sqrt{L_0/h}$ term in Eq. (6-1). For microcantilevers that are short relative to their width (smaller L/b) and for the values of b/h considered, Fig. 6-3 illustrates that support compliance effects dominate and fluid resistance effects are very small, which is why the effect of thickness h (i.e., the last term in Eq. (6-1)) is negligible. But for more slender microcantilevers (larger L/b) the fluid resistance effects are large and thus the dependence on h for given value of b/h is more prominent, i.e., the second and third terms in Eq. (6-1) become negligible and the fourth term becomes linear in L/b. The starting value of L/b for each curve corresponds to $1/\bar{k} = 0.15$ (upper limit of support compliance) and the ending value to ζ = 0.6 (upper limit of fluid resistance parameter). The relative decrease in natural frequency at the starting value of L/b for all curves is about 0.21% and is about 0.16% at the ending value of L/b. For a fixed h value, it is also clear that for smaller L/b ratios the natural frequency drop decreases with an increase in b/h because the relative support compliance, $1/\bar{k}$, decreases as b/h increases. [See Eq. (5-11).] Conversely, for larger L/b ratios, the fluid resistance effect becomes dominant and, as indicated by the ζ definition given by Eq. (5-14) and the last term in Eq. (6-1), an increase in b/h will increase ζ and thus will also increase the relative natural frequency change. Because of

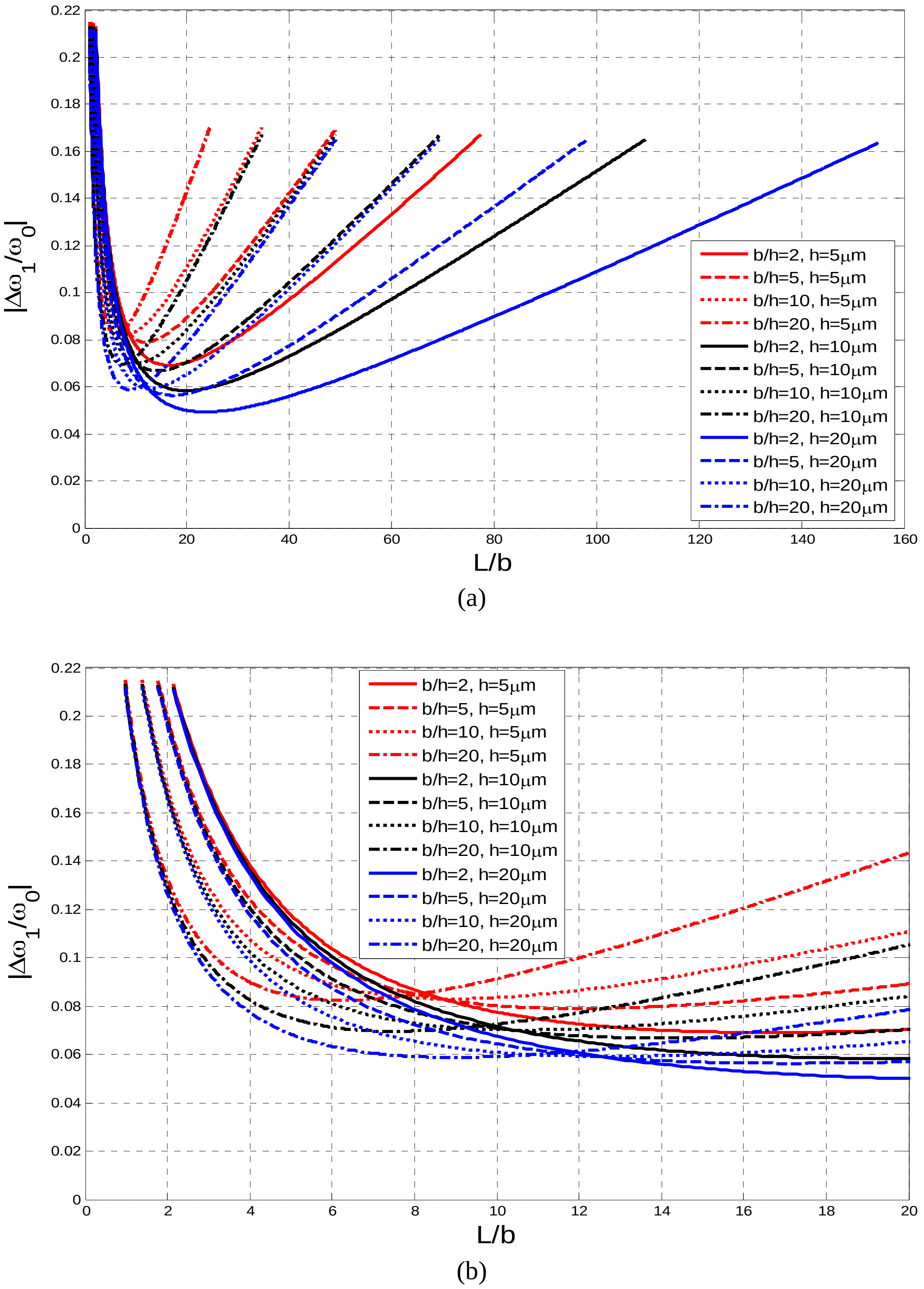

Figure 6-3: Relative difference between fundamental lateral natural frequency and perfectly clamped in-vacuum value for a silicon microcantilever beam in water with h = [5, 10, 20] μm and b/h = [2, 5, 10, 20]: (a) $L/b \in [0, 160]$, (b) $L/b \in [0, 20]$ (zoomed view).

the two competing effects, the plots of Fig. 6-3 are not monotonic. For each curve there is a value of the L/b ratio for which the frequency drop has a relative minimum. When the L/b ratio is very large the relative frequency drop approaches $\zeta/2\lambda_1$ which is in agreement with the SDOF results for a perfectly fixed cantilever beam [Heinrich et al., 2010a]. The drop in natural frequency from the fixed cantilever model [Heinrich et al., 2010a] to the current elastic support model is 21% for the starting L/b value for each value of b/h considered. For the range of b/h considered, the difference between the two models is negligible (percent change in natural frequency is less that 4%) if $L/b > 15$. (This limiting value of L/b is governed by the results for $b/h = 2$.) It is important to note that at smaller values of L/b, not only are the support compliance effects important as indicated here, but other effects that have been neglected in the present Euler-Bernoulli beam model – namely, the "Timoshenko beam effects" of shear deformation and rotatory inertia – will also be important. Thus, one should use the results of Fig. 6-3 at smaller values of L/b with caution; to obtain more accurate values in this range the results of Ch. 5 could be used to specify appropriate boundary conditions in the Timoshenko beam model of Schultz (2012) to generate improved values of the relative frequency change, which would be expected to be larger due to the increased flexibility and inertia of a Timoshenko beam relative to its Bernoulli-Euler counterpart.

6.2.2 Quality Factors

The impact of support compliance, $1/\overline{k}$, fluid resistance, ζ and beam geometry parameters on the quality factors are presented in this section. The parametric study of the ”exact” quality factor furnished by the model for the free-vibration case, given by Eq.

(4-21), in terms of $1/\bar{k}$ and ζ for the first three modes of in-fluid lateral vibration is presented in Fig. 6-4. This figure clearly indicates that the quality factors decrease with increases in support compliance, $1/\bar{k}$ and fluid resistance, ζ. It is also clear from the figure that the quality factor increases with mode number, a trend that has also been observed in theoretical and experimental studies on transverse-mode microcantilevers [e.g., Van Eysden and Sader, 2007; Ghatkesar et al., 2008]. The quality factor is heavily dependent on fluid resistance parameter, ζ, especially at small values. In contrast the quality factor dependence on support compliance is quite small.

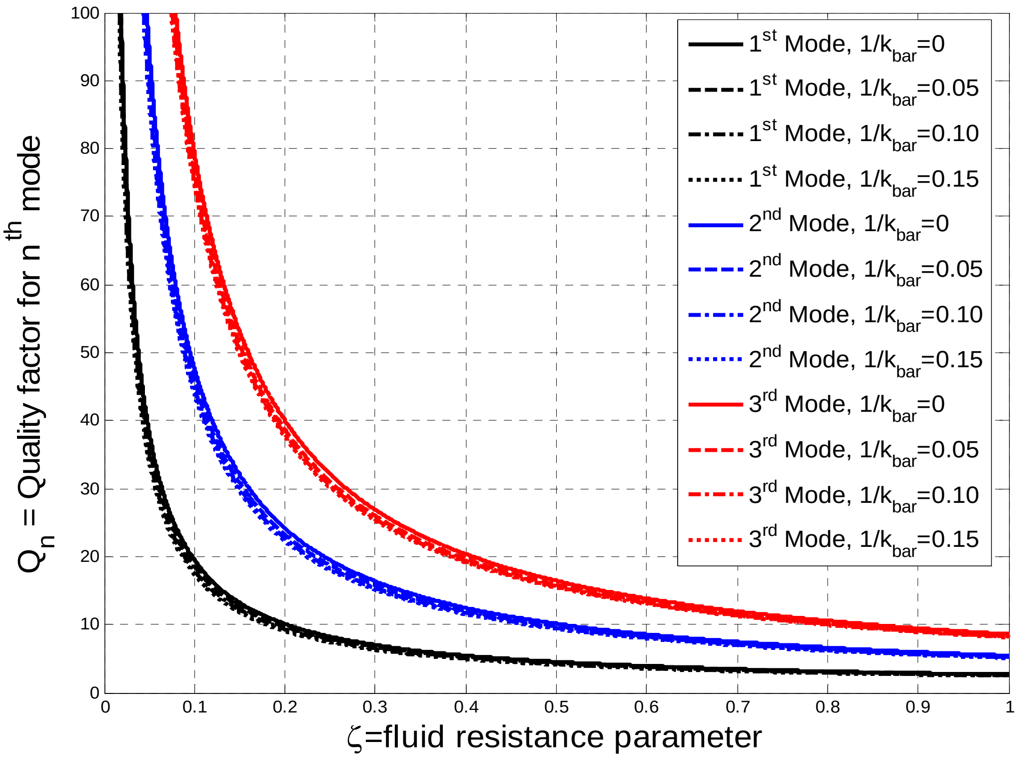

Figure 6-4: Quality factor for the first three modes based on lateral free vibration of a microcantilever beam in a viscous fluid [Eq. (4-21)].

Figure 6-5a shows the comparison of the approximate analytical result for quality factor, given by Eq. (4-36), with the exact results presented in Fig. 6-4, based on Eq. (4-

21), for the case of the fundamental lateral mode of vibration. For the practical ranges of support compliance, $1/\bar{k} \in [0, 0.15]$, and fluid resistance, $\zeta \in [0, 0.6]$, the approximate results compare quite well with the exact results. Over these ranges the percentage error of the approximate results is less that 5%. Figure 6-5b shows the comparison of the approximate analytical result for quality factor, given by Eq. (4-37), with the exact results presented in Fig. 6-4, based on Eq. (4-21), for the case of the fundamental lateral mode of vibration. For the same ranges of support compliance, $1/\bar{k} \in [0, 0.15]$, and fluid resistance, $\zeta \in [0, 0.6]$, the maximum error in this case is 25%. However, the case for utilizing the simpler form for Q given by Eq. (4-37) may be made on three points: (1) The simpler form of Eq. (4-37) will permit a very concise description of the dependence of Q on the geometric and material parameters, as will be discussed shortly. (2) While the accuracy level of Eq. (4-37) appears to be much worse than that of Eq. (4-36), the latter equation differs from the former only by an additive constant of 0.75. (See previous discussion in Sect. 4.2.2.) Thus, the larger relative error of Eq. (4-37) is only significant at lower Q values, i.e., for devices/fluids that are not of interest here since they are not viable candidates for liquid-phase sensing applications. (One of the primary motivations of this study is to achieve high Q in liquids by exploiting the lateral mode.) (3) Because the Stokes-type fluid resistance model tends to overestimate the viscous quality factor, the fact that Eq. (4-37) yields a smaller value of Q than Eq. (4-36) will slightly compensate for some of the error inherent in the fluid resistance model. Thus, for these reasons Eq. (4-37) [or equivalent forms of it, such as Eq. (5-17)] will be used hereafter when presenting and discussing analytical results for the quality factor.

When the results of Ch. 5 are used to relate support compliance to beam dimensions, one may use Eq. (5-17) to directly relate the mode-1 viscous quality factor to beam geometry. To present these results in a general, yet efficient, manner the quality factor as given by the analytical Eq. (5-17), is normalized by $\sqrt{h / L_0}$ so that the resulting analytical expression for the quality factor,

$$\frac{Q_1}{\sqrt{\frac{h}{L_0}}} \approx \frac{0.7124}{\frac{L}{b}\sqrt{\frac{b}{h}}}\left(1-\frac{0.95}{\frac{L}{b}\frac{b}{h}\left(0.2088+\frac{2.710}{(b/h)}\right)}\right) \tag{6-4}$$

can be used to generate plots that are applicable for any value of thickness h and any material and fluid, provided that the parameter range constraints [Eqs. (5-18a-c) or, equivalently, Eqs. (6-2) and (6-3)] are not violated. This normalized quality factor is plotted against the L/b ratio for different b/h values and for $L/b \in [0, 20]$ as shown in Fig. 6-6. From the figure it is clear that, for specified values of thickness (*h*) and material properties (L_0) and a fixed width (*b*), the quality factor increases with a decrease in length *L*. This figure may be used to graphically determine the quality factor for a lateral-mode microcantilever of specified geometry and given beam and fluid properties. Note that the starting points of the curves in Fig. 6-6 are dictated by the lower bound of the constraint given by Eq. (6-2). It is also important to note that Fig. 6-6 should NOT be applied for L/b ratios in excess of the upper bound listed in Eq. (6-2), although the entire curves of Fig. 6-6 are applicable in many practical instances. For example, if the beam material is silicon ($E = 169$ GPa, ρ_b =2330 kg/m^3) and the fluid is water (η =0.001 Pa.s, ρ_f =1000 kg/m^3), then Fig. 6-6 is valid in its entirety provided that $h \geq 3.3\,\mu\text{m}$.

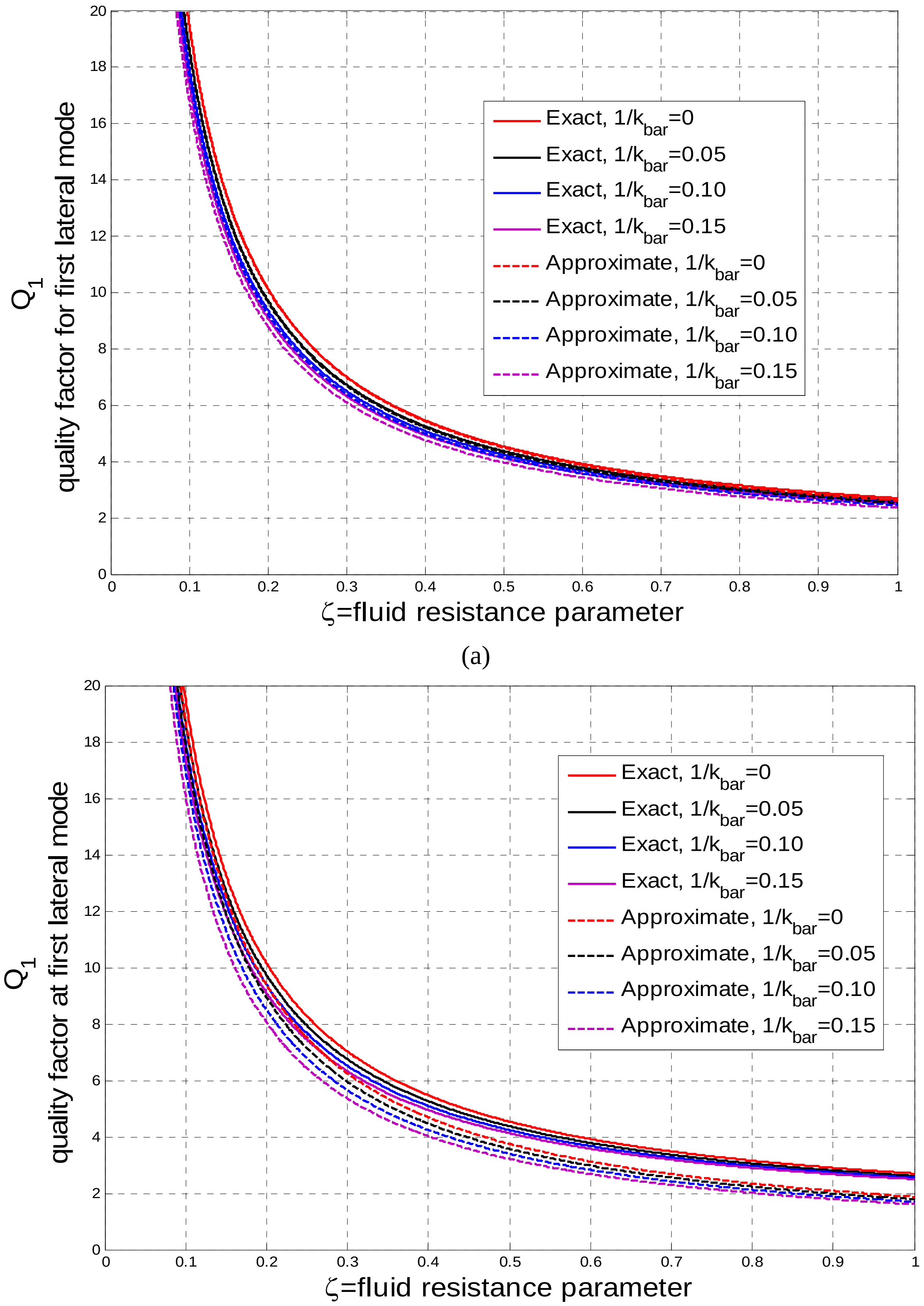

(a)

(b)

Figure 6-5: Comparison of exact and approximate quality factor for the fundamental mode of lateral free vibration of a microcantilever beam in a viscous fluid: Approximate results given by (a) Eq. (4-36), (b) Eq. (4-37).

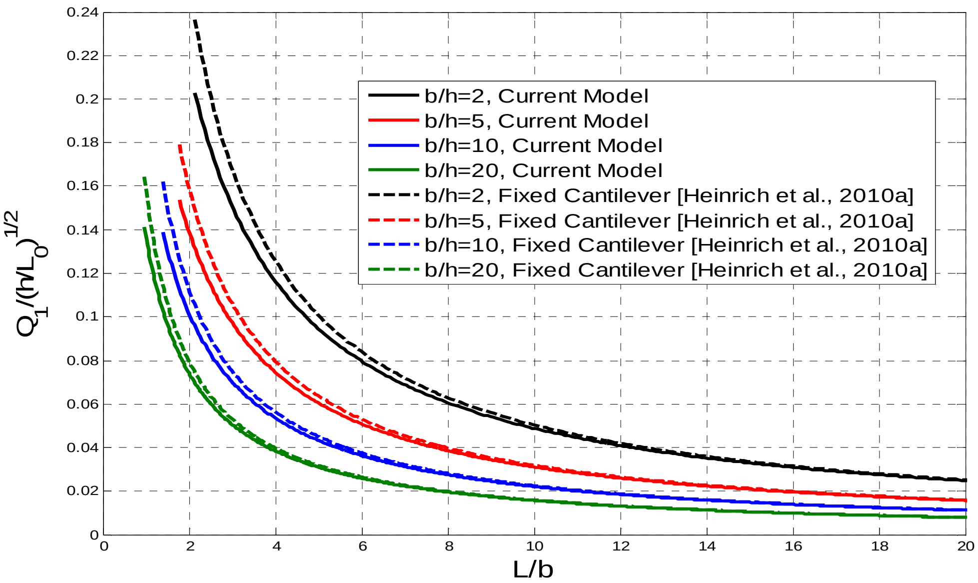

Figure 6-6: Normalized mode-1 viscous quality factor in terms of beam geometry for lateral vibration of a cantilever beam in an arbitrary viscous fluid. Results of current compliant-support model based on analytical formula, Eq. (6-4). This figure should NOT be applied for L/b ratios in excess of the upper bound listed in Eq. (6-2). (Dashed curves are based on the fixed-support model of Heinrich et al., 2010a.)

The quality factor results for a perfectly fixed beam [Heinrich et al., 2010a] are also shown in Fig. 6-6 in order to clearly display the impact of support compliance on the quality factor. It can be seen that the impact of support compliance is negligible for large L/b values but for smaller L/b values becomes more important. The drop in quality factor from the fixed cantilever model [Heinrich et al., 2010a] to the current elastic support model is 14% for the starting L/b value for each value of b/h considered. For the range of b/h considered, the difference between the two models is negligible (percent change in Q is less that 2%) if $L/b > 15$. (This limiting value of L/b is governed by the results for $b/h = 2$.) It is also to be noted that for lower L/b values the Timoshenko beam effects might play an important role. These effects have not been considered in this study but have been studied recently for the case of a perfectly fixed cantilever [Schultz et al., 2013a, b].

6.2.3 Mode Shapes

The impact of support compliance, $1/\bar{k}$, on the mode shapes are presented in this section. (Recall that these mode shapes correspond to both an in-vacuum free vibration and a free vibration in a viscous fluid providing Stokes-type resistance.) The first three mode shapes given by Eq. (4-22a) have been normalized by their absolute maximum values and are presented in Fig. 6-7a-c. These figures clearly show the effect of the support compliance parameter on the mode shapes. For a perfectly fixed cantilever, i.e., $1/\bar{k}$ =0, the slope of the mode shapes are zero at the support for all three modes, as expected, but when $1/\bar{k} \neq 0$ the mode shapes reflect the support compliance through a non-zero slope at the support. The vibrational nodes for modes 2 and 3 depend weakly on the support compliance.

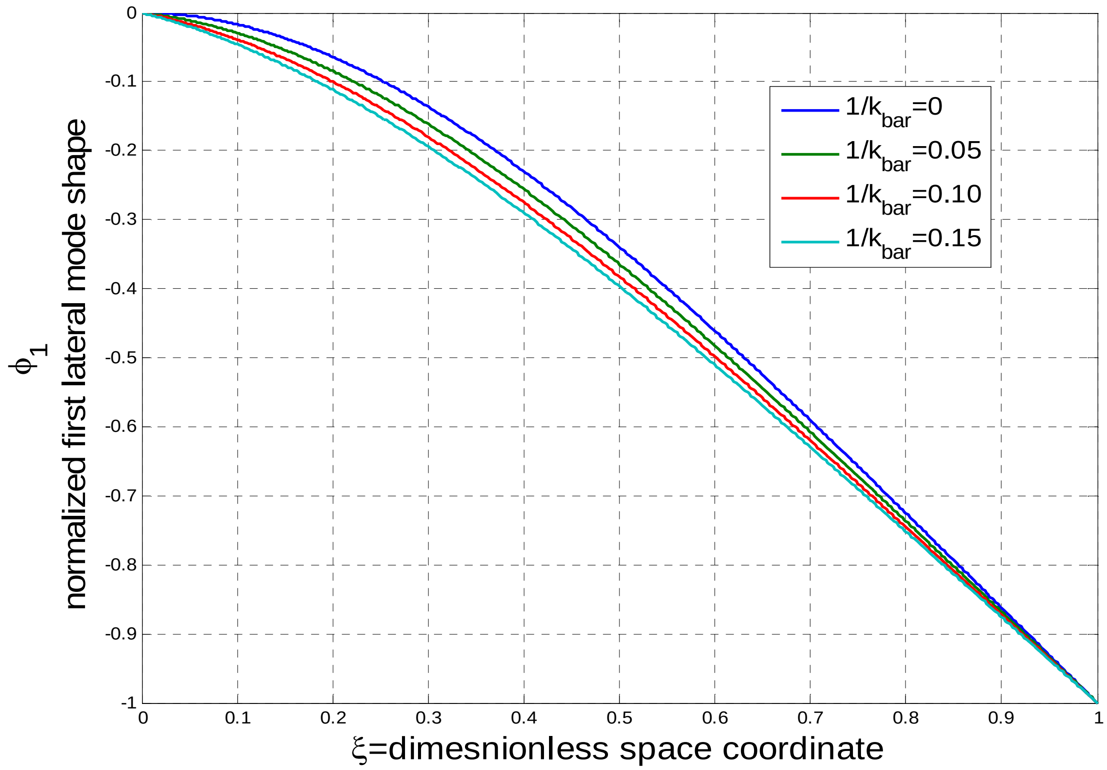

(a)

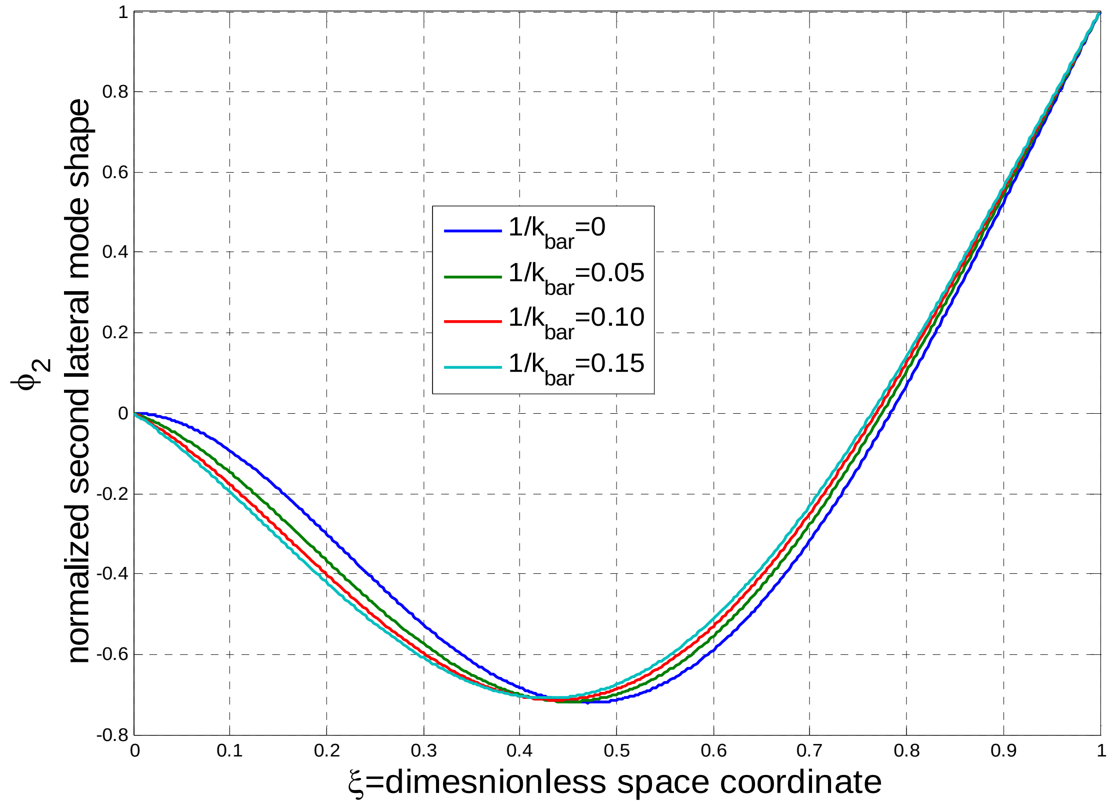

1
0.8
0.6
0.4
0.2
0
-0.2
-0.4
-0.6
-0.8
0
0.1
0.2
0.3
0.4
0.5
0.6
0.7
0.8
0.9
1
φ2
normalized second lateral mode shape
ξ=dimesnionless space coordinate
1/k_bar=0
1/k_bar=0.05
1/k_bar=0.10
1/k_bar=0.15

(b)

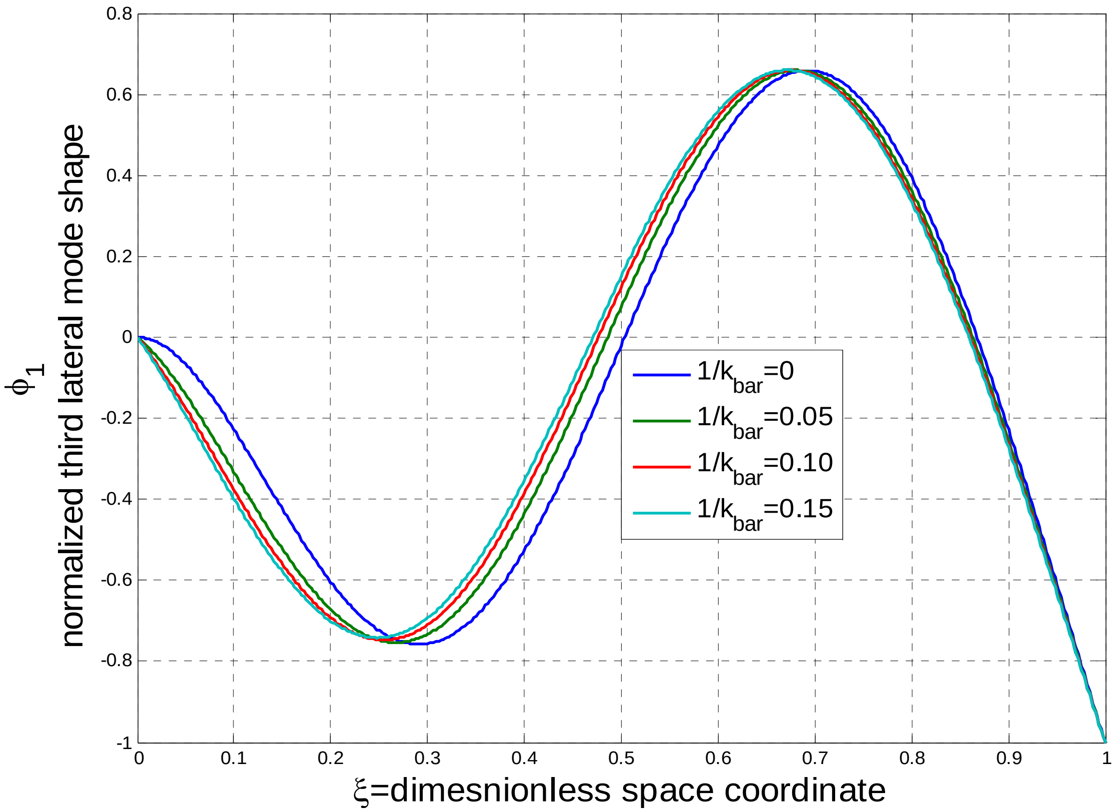

0.8
0.6
0.4
0.2
0
-0.2
-0.4
-0.6
-0.8
-1
0
0.1
0.2
0.3
0.4
0.5
0.6
0.7
0.8
0.9
1
φ1
normalized third lateral mode shape
ξ=dimesnionless space coordinate
1/k_bar=0
1/k_bar=0.05
1/k_bar=0.10
1/k_bar=0.15

(c)

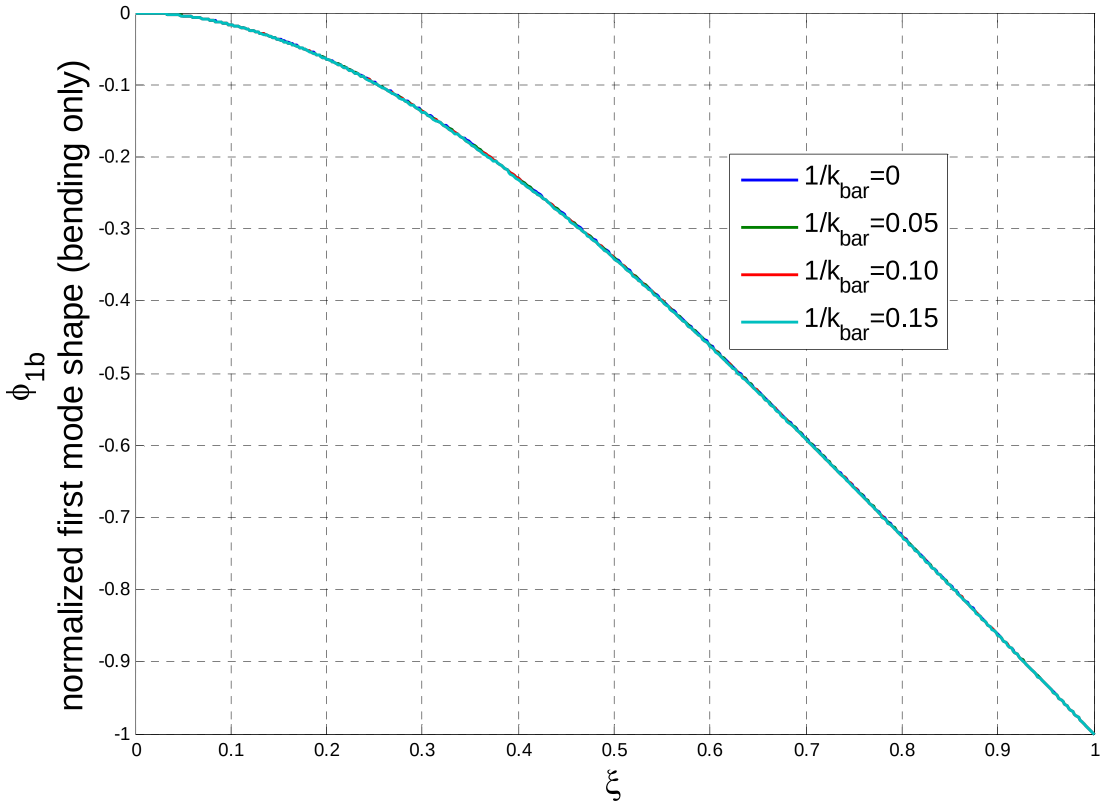

(d)

Figure 6-7: Mode shapes for the lateral vibration of an elastically supported microcantilever in a viscous fluid: (a) first mode shape, (b) second mode shape, (c) third mode shape, (d) mode-1 “bending-only” mode shape, i.e., first mode shape with rigid rotation removed.

For the first mode, if the rigid rotation due to the support rotation is subtracted out, then for all of the values of $1/\bar{k}$ considered the resulting “bending-only” mode shapes are virtually identical to that of a perfectly fixed cantilever as shown in Fig. 6-7d. However, this is not true for the higher mode shapes.

6.3 Parametric Study: Forced Vibration Due to Harmonic Relative Rotation Imposed Near the Support

In this section the results for the lateral vibration of a microcantilever in a viscous fluid will be presented for the case of an applied harmonic relative rotation near the support. As noted earlier (Sects. 1.4 and 3.4), this type of loading is of practical interest since it simulates the electrothermal excitation scheme that has been employed in lateral-mode cantilevers and cantilever-based sensors [Beardslee et al., 2010a,b; Heinrich et al., 2010b; Beardslee et al., 2012]. The theoretical results to be presented and discussed include frequency response plots, resonant frequency, quality factor and vibrational beam shapes. The frequency response plots (plots of normalized response amplitude vs. normalized exciting frequency) will be determined for two types of “output signals”: the tip displacement amplitude and the bending strain amplitude at the root of the beam. These correspond to two common response detection schemes used in microcantilever applications: optical methods and piezoresistive methods, respectively. From these frequency response plots the resonant frequencies are extracted, these being defined as the exciting frequencies at which the respective response quantities attain their relative maximum values. Also extracted from the frequency response plots are the quality factors associated with resonant peaks; these are determined by employing the -3dB bandwidth method (also known as the half-power method) [e.g., Meirovitch, 2001]. While the frequency response plots are generated over a frequency range that includes the first three modes of lateral vibration, the resonant characteristics will only be determined for the first lateral mode of vibration as it is the most easily excited and most widely used mode in lateral-mode sensing applications. The impact of support compliance, fluid resistance and beam geometry on the beam response results and the resonant characteristics are presented.

6.3.1 Frequency Response

The frequency response plots for the tip displacement amplitude are generated by plotting the dynamic magnification factor for tip displacement, given by Eq. (4-49), against the dimensionless exciting frequency as shown in Fig. 6-8. Similarly, the frequency response plots for bending strain amplitude at the root are generated by plotting the normalized amplitude of the maximum bending strain at the root of the beam, given by Eq. (4-56), as shown in Fig. 6-9. Figure 6-8a shows frequency response plots for tip displacement amplitude over a frequency range that includes the first three lateral modes, while Fig. 6-8b provides a clearer view of the first-mode response. Figure 6-9 shows analogous information when the bending strain amplitude at the root is used as the theoretical output signal.

Figure 6-8a indicates a reduction in resonant peak amplitudes at the higher resonances for the tip displacement signal, thus indicating that the first resonant mode may be the most suitable of the lateral flexural modes for sensing applications using a response detection method that tracks the tip deflection (or tip slope), e.g., optical. Figure 6-8a also shows the expected decrease in resonant frequencies and resonant peak amplitudes as the values of support compliance and fluid resistance parameter are increased. Similar trends are seen in Fig. 6-9 for the root bending strain amplitude, with the exception that the resonant peak amplitude *increases* as the mode number increases. The responses based on the two different detection schemes are exhibited more clearly in Fig. 6-10 for a particular system having a support compliance of $1/\overline{k} = 0.05$ and a fluid resistance parameter of $\zeta = 0.2$. In contrast to tip-tracking detection schemes, if the higher modes can be excited, strain-based detection methods (e.g., piezoresistive) may

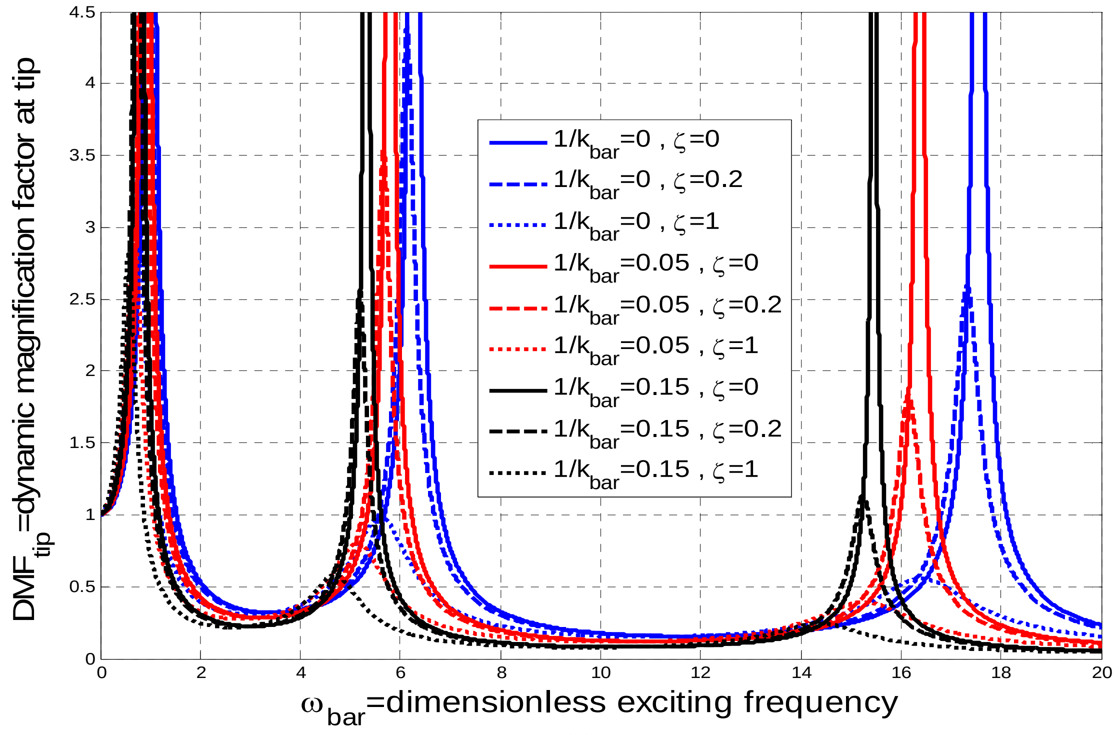

(a)

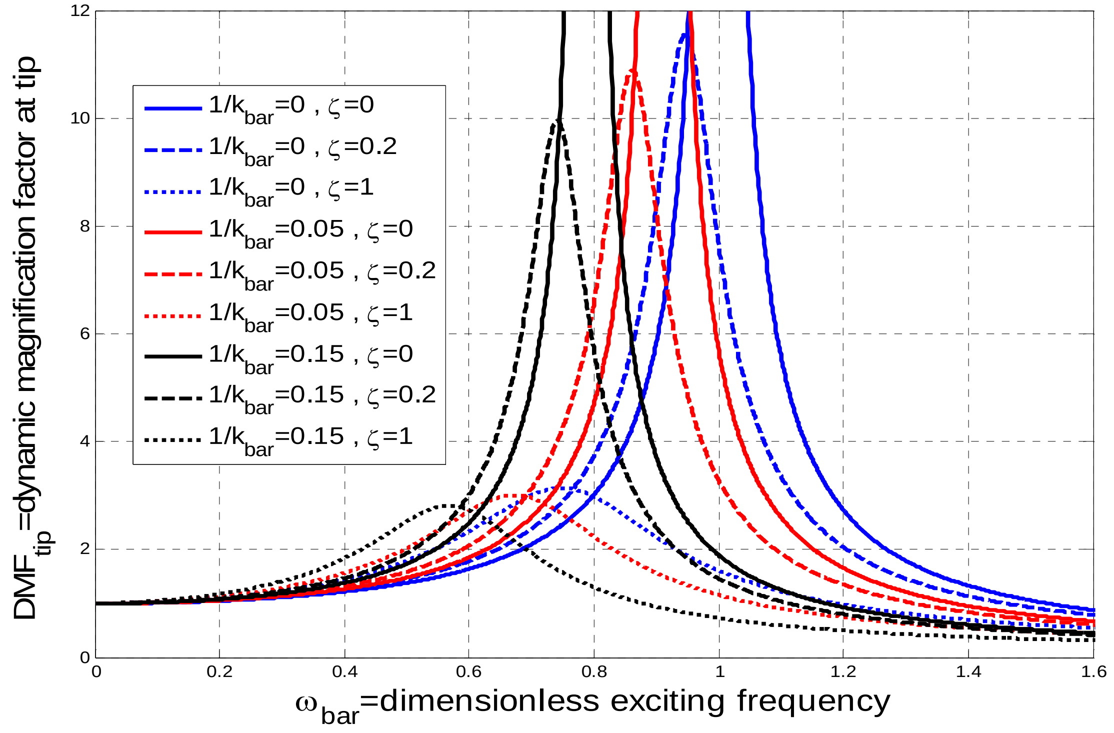

(b)

Figure 6-8: Frequency response plots of normalized tip displacement amplitude for the lateral vibration of a microcantilever in fluid caused by relative harmonic rotation near the support: (a) $\bar{\varpi} \in [0, 20]$ (including first three modes), (b) $\bar{\varpi} \in [0, 1.6]$ (including first mode).

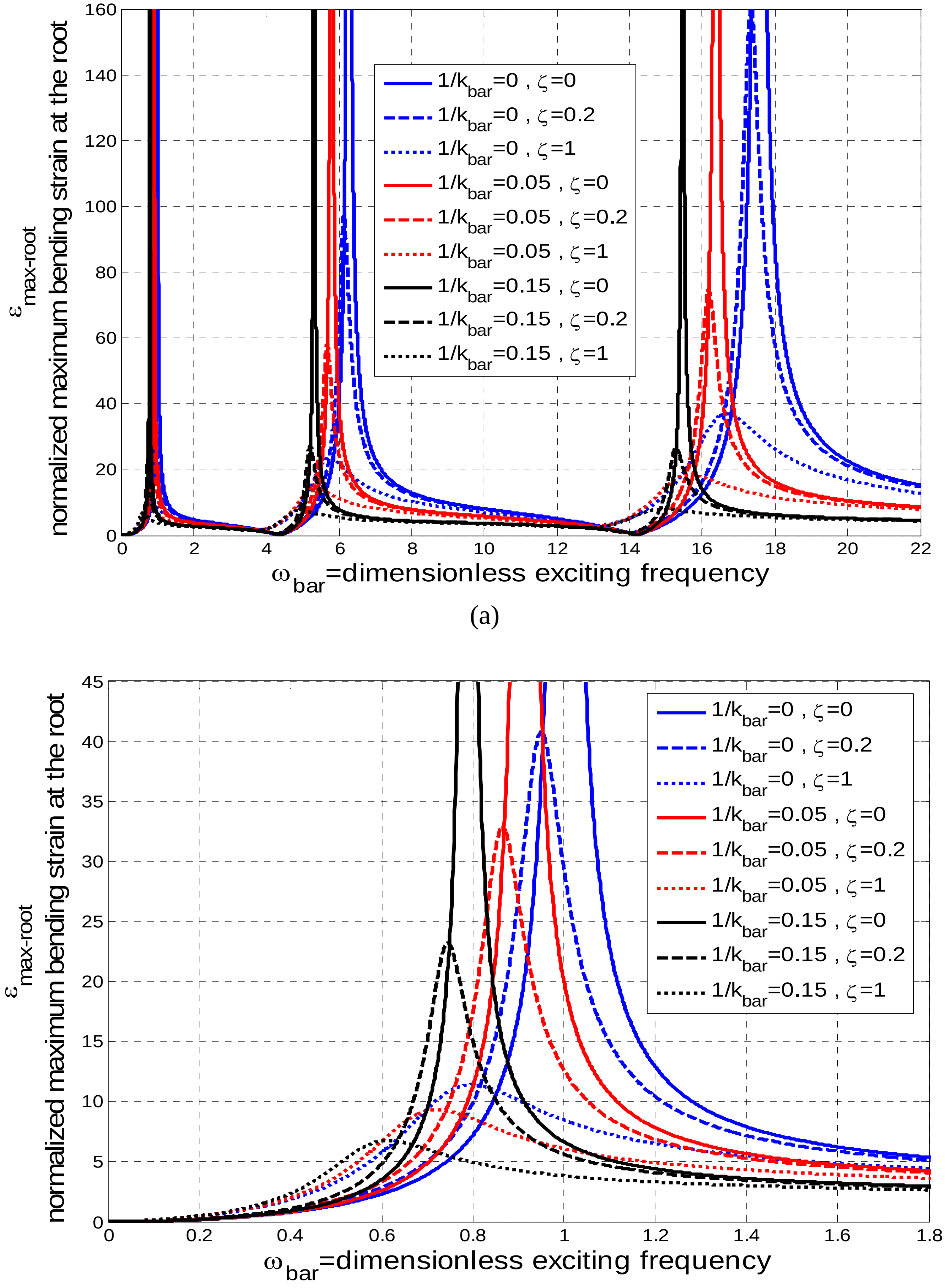

(a)

(b)

Figure 6-9: Frequency response plots of normalized bending strain amplitude at the root of a cantilever for lateral vibration in fluid caused by relative harmonic rotation near the support: (a) $\bar{\omega} \in [0, 22]$ (including first three modes), (b) $\bar{\omega} \in [0, 1.8]$ (including first mode).

have advantages at higher modes due to the stronger signal amplitude at higher modes in comparison to the fundamental lateral mode. All curves in Fig. 6-8 (and the solid curve in Fig. 6-10) start at 1 because at low frequencies the amplitude of tip displacement approaches the quasi-static value associated with a rigid rotation of the beam. The curves in Fig. 6-9 (and the dashed curve in Fig. 6-10) start at zero because, when the load is applied quasi-statically (i.e., at a very low frequency), there is no bending strain in the beam since the beam undergoes only a rigid rotation. Also, it is noted that, for $\zeta = 0$, the maximum strain amplitude is zero at some exciting frequencies, indicating that the vibrational shape at those frequencies has zero curvature at the supported end. In other words, it indicates that the beam shape is in transition from one mode shape to the next.

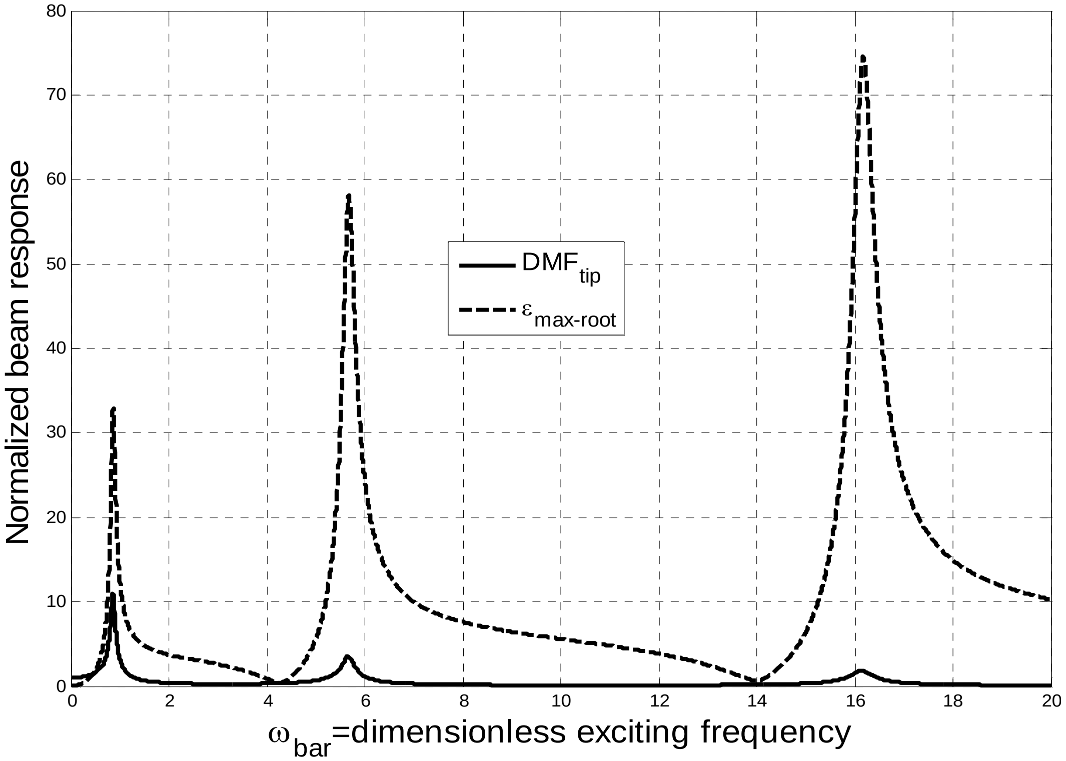

Figure 6-10: Comparison of frequency response plots for normalized tip displacement amplitude and normalized bending strain amplitude at the root for a cantilever excited laterally by a relative harmonic rotation near the support ($1/\overline{k} = 0.05$, $\zeta = 0.2$).

6.3.2 Resonant Frequency

The resonant frequency can be obtained from the frequency response plots as it is by definition the exciting frequency at which the response attains a relative maximum. Even though the higher mode resonant frequencies can be extracted from the frequency response plots discussed in previous section, only the first-mode resonant frequency is extracted and discussed in this section.

In Fig. 6-11 the first-mode resonant frequency based on both tip displacement amplitude and maximum bending strain amplitude at the root is presented in terms of support compliance and the fluid resistance parameter. From Fig. 6-11 it is clear that, as expected, the fundamental lateral resonant frequency decreases with an increase in $1/\overline{k}$ and ζ. It is also clear that this resonant frequency as detected by the maximum bending strain signal is greater than that for the tip displacement response, with the difference being negligible at smaller values of ζ (less than 2% for $\zeta \in [0, 0.4]$) but approaching 8% as ζ approaches 1. As sensitivity is directly proportional to the resonant frequency [Dufour et al., 2007a, b] it can be concluded that the sensor devices that detect resonant response by monitoring the bending strain at the root of the cantilever will be more sensitive than ones whose output signal is based on tracking the tip displacement, and this advantage will become more evident at higher values of the fluid resistance parameter.

Figure 6-12 compares the resonant frequency at first resonance, as detected by both the tip displacement response and the bending strain response, to the first-mode natural frequency obtained from the analytical expression given by Eq. (4-34). From Fig. 6-12 it is clear that the natural frequency closely resembles the resonant frequency for the ranges of $1/\overline{k}$ and ζ considered, especially for small values of ζ (less than 1% error for

$\zeta \in [0, 0.3]$). Thus, the same analytical expressions for the first-mode dimensionless natural frequency given by Eqs. (4-34) and (5-16) can be utilized to predict the impact of support compliance, fluid resistance parameter and beam geometric parameters on resonant frequency at the first resonance for in-fluid lateral vibration of the cantilever via harmonic relative rotation near the support. The free vibration analytical result predicts the resonant frequency based on tip displacement better than that based on maximum bending strain at the root.

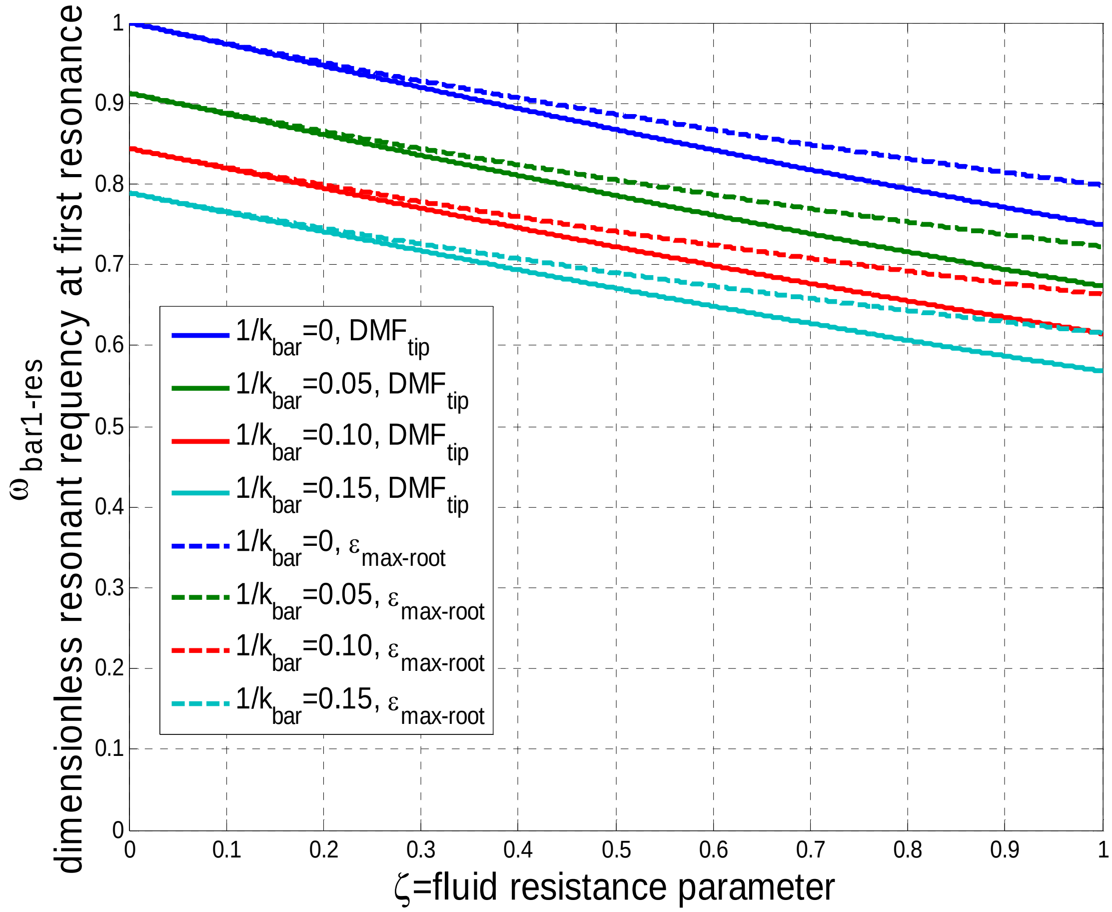

Figure 6-11: Comparison of resonant frequency at first lateral resonance for tip displacement response and maximum bending strain response at the root of a cantilever in a viscous fluid caused by relative harmonic rotation near the support. (Resonant frequency extracted from frequency response curves.)

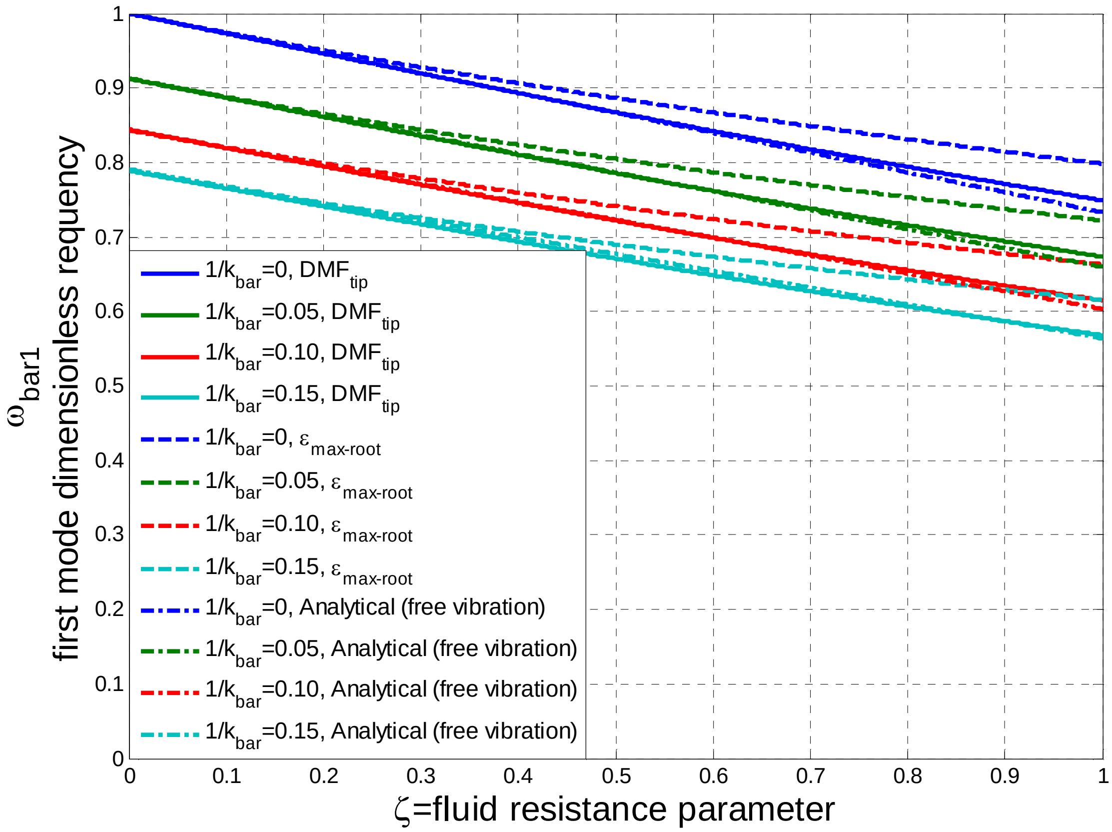

Figure 6-12: Comparison of first-mode lateral resonant frequency (extracted from frequency response curves) for excitation via harmonic relative rotation near support (both via tip displacement response and maximum bending strain response at the root) with the first-mode lateral natural frequency obtained via analytical expression [Eq. (4-34)] for free vibration case.

6.3.3 Quality Factor

The quality factor is extracted from the frequency response plots using the -3dB bandwidth method. The quality factor estimate from this method is valid for small levels of damping. i.e., for small values of the fluid resistance parameter. In the -3dB bandwidth method the quality factor is calculated as the ratio of the resonant frequency to the -3dB bandwidth of the resonant peak of the frequency response [Meirovitch, 2001]. The quality factor at the first resonant peak is calculated by applying this method to both the tip displacement response and the bending strain response and is shown in Fig. 6-13.

From Fig. 6-13 it is clear that the quality factor decreases with an increase in the fluid resistance parameter and support compliance. The quality factor is extremely sensitive to ζ at small values of ζ. The effect of $1/\bar{k}$ is relatively weak compared to that of ζ. Also for small values of ζ, the quality factor based on maximum bending strain response at the root is nearly equal to that obtained via the tip displacement response. For larger values of ζ, the tip displacement response quality factor is greater than its bending–strain counterpart. But as mentioned earlier, for large values of ζ the -3dB bandwidth method does not accurately estimate quality factor.

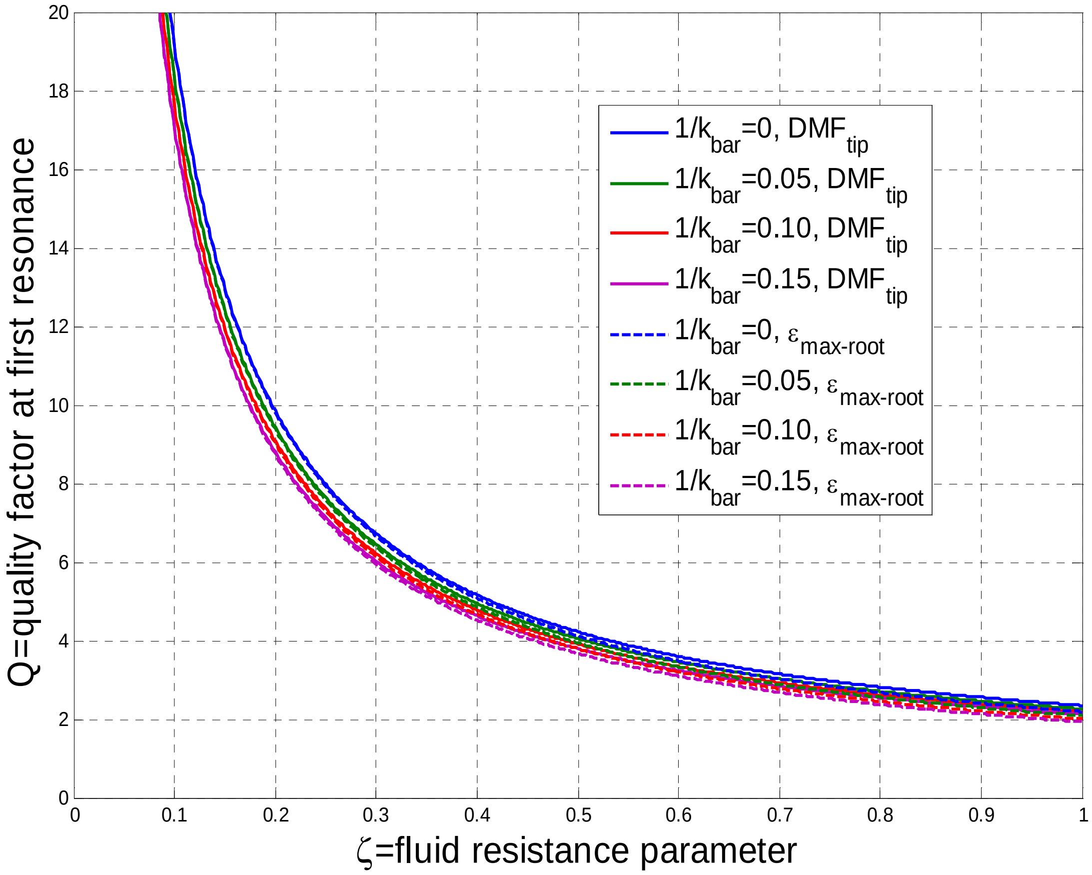

Figure 6-13: Comparison of quality factor (bandwidth method) at first resonance based on tip displacement response and maximum bending strain response at the root of the cantilever for lateral vibration in fluid caused by relative harmonic rotation near the support.

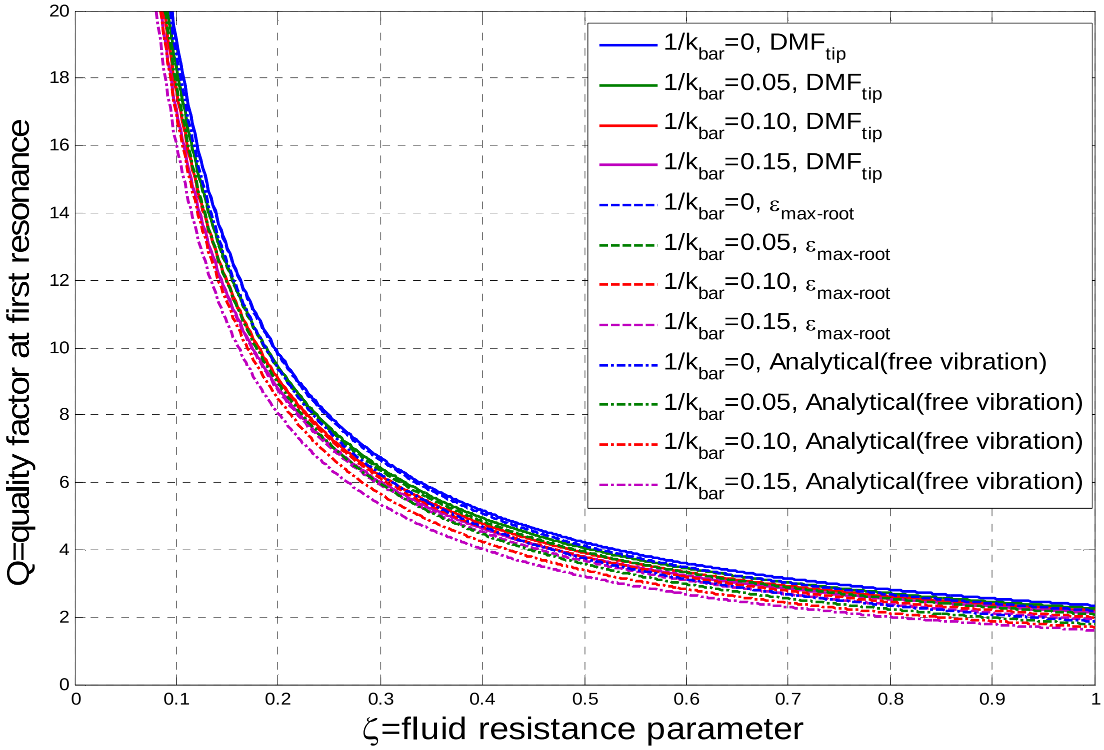

Figure 6-14: Comparison of first-mode quality factor (bandwidth method) for lateral excitation via harmonic relative rotation near support (both via tip displacement response and maximum bending strain response at the root) with the first-mode quality factor obtained via analytical expression [Eq. (4-37)] for lateral free vibration case.

Figure 6-14 compares the quality factor at first resonance for the forced vibration case, as detected by the two output signals mentioned above, with the first-mode quality factor obtained from the simple analytical expression for the free vibration case [Eq. (4-37)]. The figure shows that the analytical free vibration quality factor compares quite well with those based on the forced vibration case for small ζ values, i.e., those yielding relatively large Q values. The percent error is large for larger ζ values, but as explained earlier (Sect. 6.2.2) this study is mainly focused on obtaining higher quality factors, i.e., smaller ζ values. Thus, the same analytical expressions for quality factor, i.e., Eq. (4-37) and Eq. (5-17), can be used to predict the impact of support compliance, fluid resistance parameter and beam geometry parameters on quality factor at the first lateral resonance.

6.3.4 Vibrational Beam Shapes

The time-dependent vibrational shapes for forced vibration via relative harmonic rotation near the support are presented in Fig. 6-15. These shapes are plotted for $1/\bar{k}=0.15$, $\zeta=0.2$ and $\bar{\omega}=0.7447$ (fundamental lateral resonant frequency) and are based on a real forcing function of the form $\theta(\tau)=\text{Re}[\theta_0 e^{i\bar{\omega}\tau}]$. Thus, what is plotted in Fig. 6-15 is $\text{Re}[\bar{y}(\xi,\tau)]/\theta_0$, where $\bar{y}(\xi,\tau)$ is given by Eqs. (4-40) and (4-46). The figure clearly shows how the deflected position of the beam changes throughout one complete cycle of steady-state vibration. For the considered values of $1/\bar{k}$, ζ, and $\bar{\omega}$, the vibrational shape (if normalized) is essentially constant over time. (The exceptions are near $\bar{\omega}\tau=0,\ \pi,\ 2\pi$, at which times the beam is passing through an essentially undeformed configuration.) The maximum values of the beam deflection appear to occur near $\bar{\omega}\tau=\pi/2$ and $\bar{\omega}\tau=3\pi/2$. Note that the beam positions indicated in the figure are consistent with the concept that, at resonance, the response should lag the input by approximately 90 degrees.

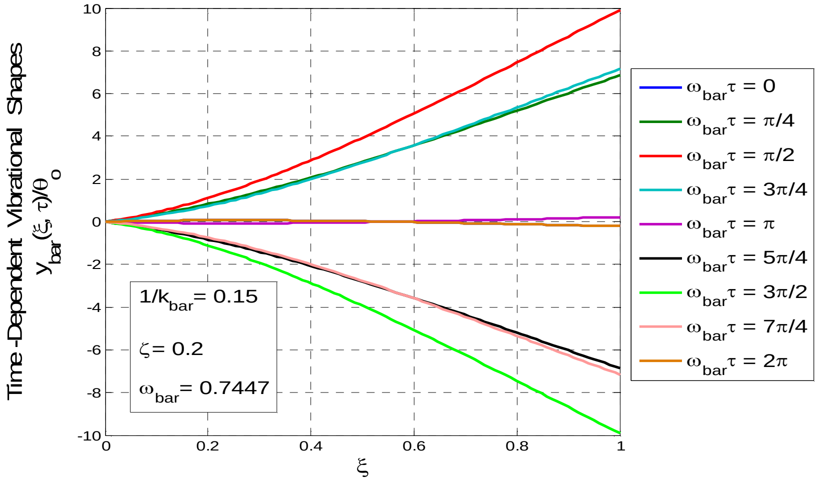

Figure 6-15: Time-dependent vibrational shapes due to relative harmonic rotation near support for $1/\bar{k}=0.15$, $\zeta=0.2$, and $\bar{\omega}=0.7447$.

6.4 Comparisons with Experimental Data

The purpose of this section is to compare the present analytical results for the in-fluid lateral-mode resonant frequency and quality factor to experimental data [Beardslee et al., 2010a; Beardslee et al., 2012]. The microcantilever devices used in the experiments were excited electrothermally near the support and the beam motion was detected via piezoresistive elements positioned near the "extreme fibers" of the cross section near the support. Thus, the most appropriate theoretical results of this study are those based on the forced-vibration model excited by an imposed relative rotation near the support with the output signal being the maximum bending strain at the root of the cantilever. However, as explained earlier (Sects. 6.3.2 and 6.3.3), at resonance the forced vibration results are very close to the free vibration results and, thus, the analytical formulae based on the free vibration results will be used here in making comparisons with the experimental data.

For the experiments the microcantilever beam was made of silicon and the liquid used was water. The experimental data were collected for four sets of nominal cantilever thickness, $h_{nom} = (5, 8, 12, 20)\,\mu\text{m}$ and each thickness consisted of five cantilever lengths, $L = (200, 400, 600, 800, 1000)\,\mu\text{m},$ and four cantilever widths, $b = (45, 60, 75, 90)\,\mu\text{m}.$ The silicon cantilever was coated with several passivation layers, consisting of thermal oxide, PECVD silicon oxide and PECVD silicon nitride [Beardslee et al., 2012]. In comparing theoretical results with experimental data, the average total thickness is used in the theoretical models instead of the nominal thickness. These total thickness values were obtained by taking the average Si thickness and adding the corresponding passivation thickness. The average total thickness values for each nominal thickness set are listed in Table 6.1. As explained above, the beam is not homogeneous but made of different layers of different materials. Thus, the material properties of the composite beam, especially the effective Young's modulus *E*, will be different than that of pure silicon. The theoretical model is based on a homogeneous beam and, thus, an effective value of *E* for the composite beam must be specified in the model. Since it is difficult to specify the appropriate value of effective Young's modulus, its value is determined by performing a least-squares fit of existing resonant frequency data for the in-air case with the in-vacuum, perfectly fixed cantilever model. (See Appendix C.) In performing the fit, it is assumed that the air resistance is negligible and only the data for $L = (800\,, 1000)\ \mu\text{m}$ are considered for the fit. This is because the larger-length specimens are not expected to exhibit support-compliance and Timoshenko beam effects, so that these complicating effects will be negligible so that the fit will yield a reasonable estimate of the effective modulus. Also, the density of the composite beam is assumed to be the same as that of silicon ρ_b =2330 kg/m^3. The best fit values for *E* for the different nominal thickness sets are listed in Table 6-2. The results show a very modest dependence on the cantilever thickness; thus, the average Young's modulus of these four thickness sets, *E*=142 GPa, will be used as the effective Young's modulus in all of the theoretical calculations in this section. Other input values to be specified in the theoretical model include the properties of water, given by ρ_f =1000 kg/m^3 and $\eta = 0.001$ Pa·s , and the specimen geometries as specified by h = (7.009, 10.32, 14.48, 22.34) μm, L = (200, 400, 600, 800, 1000) μm, and b = (45, 60, 75, 90) μm. The present theoretical results will also be compared with the results obtained from the Euler-Bernoulli model without support compliance effects [Heinrich et al., 2010a].

Nominal Thickness h_{nom} (μm)	Average Silicon Thickness h_{Si} (μm)	Passivation Layer Thickness $h_{pas.}$ (μm)	Average Total Thickness h_t (μm)
5	5.169	1.84	7.009
8	8.48	1.84	10.32
12	12.61	1.87	14.48
20	20.47	1.87	22.34

Table 6-1: Average total thickness for each nominal thickness set [Beardslee and Brand, 2010].

Nominal Thickness h_{nom} (μm)	Young's Modulus E (GPa)	Average Young's Modulus E (GPa)
5	138.97	141.81 ≈ **142**
8	141.07	
12	138.67	
20	148.52	

Table 6-2: Effective Young's modulus based on fitting lateral-mode in-vacuum, perfectly fixed model to in-air experimental lateral frequency data.

Figures 6-16a-d show the comparison of resonant frequency from the current model [Eq. (6-1)] and the experimental data (in water) for each nominal thickness set. Also shown are the results from the Euler-Bernoulli fixed cantilever model. From the figures it is evident that the frequencies from the current model are closer to the experimental data than the perfectly fixed cantilever model based on Euler Bernoulli theory without support effects [Heinrich et al., 2010a]. But the current model still overestimates the experimental data, especially for the shorter and wider beams. This might be because of Timoshenko beam effects (shear deformation and rotatory inertia effects) which have not been considered in the present model. The other reason for the overestimation, especially for larger thickness, might be that the pressure effects of water on the side faces of the beam are not negligible as is being assumed in the present model.

Figures 6-17a-d show the quality factor comparison between the current model [Eq. (5-17) or, equivalently, Eq. (6-4)] and the experimental data for the various nominal thickness sets. Also shown are the results of the earlier fixed-cantilever model [Heinrich et al., 2010a]. It is evident from the figures that the quality factors from the current model are closer to experimental data than the results based on the perfectly fixed cantilever model of Heinrich et al., 2010a. For the thinner specimens (nominal thicknesses of $5\,\mu\mathrm{m}$ and $8\,\mu\mathrm{m}$) the results of the present model provide very good quantitative estimates of Q (as does the earlier model); however, for the thicker beams (nominal thicknesses of 12 $\mu\mathrm{m}$ and $20\,\mu\mathrm{m}$) the present results consistently overestimate the experiment data. This is most likely due to the fact that the Stokes-type fluid resistance assumption becomes worse as thickness increases. Also, the softening effect predicted by the model at higher $\sqrt{b}/L$ values is not as pronounced as that exhibited by the data. This indicates that other softening effects not considered here are coming into play. As explained earlier, these effects might include the Timoshenko beam effects of shear deformation and rotatory inertia. Such effects have been included in a model proposed recently [Schultz, 2012; Schultz et al., 2013a, b].

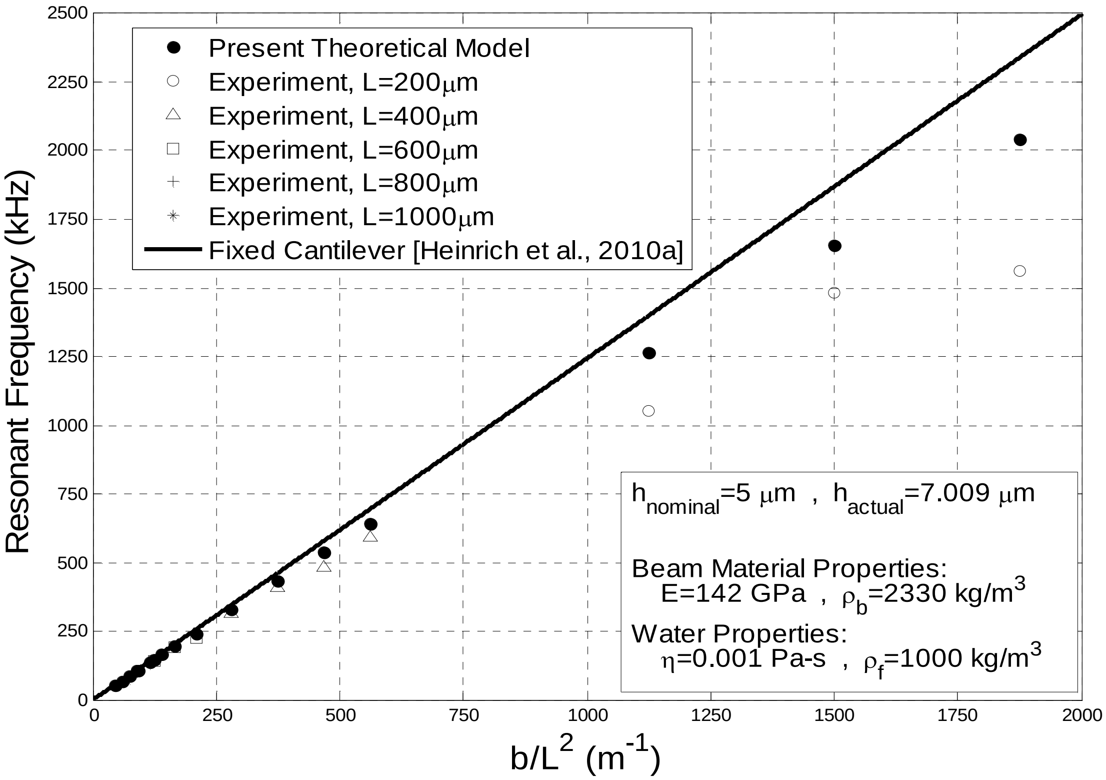
Present Theoretical Model
Experiment, L=200μm
Experiment, L=400μm
Experiment, L=600μm
Experiment, L=800μm
Experiment, L=1000μm
Fixed Cantilever [Heinrich et al., 2010a]
h_nominal=5 μm , h_actual=7.009 μm
Beam Material Properties:
E=142 GPa , ρ_b=2330 kg/m^3
Water Properties:
η=0.001 Pa-s , ρ_f=1000 kg/m^3
Resonant Frequency (kHz)
b/L^2 (m^-1)
0
250
500
750
1000
1250
1500
1750
2000
2250
2500

(a)

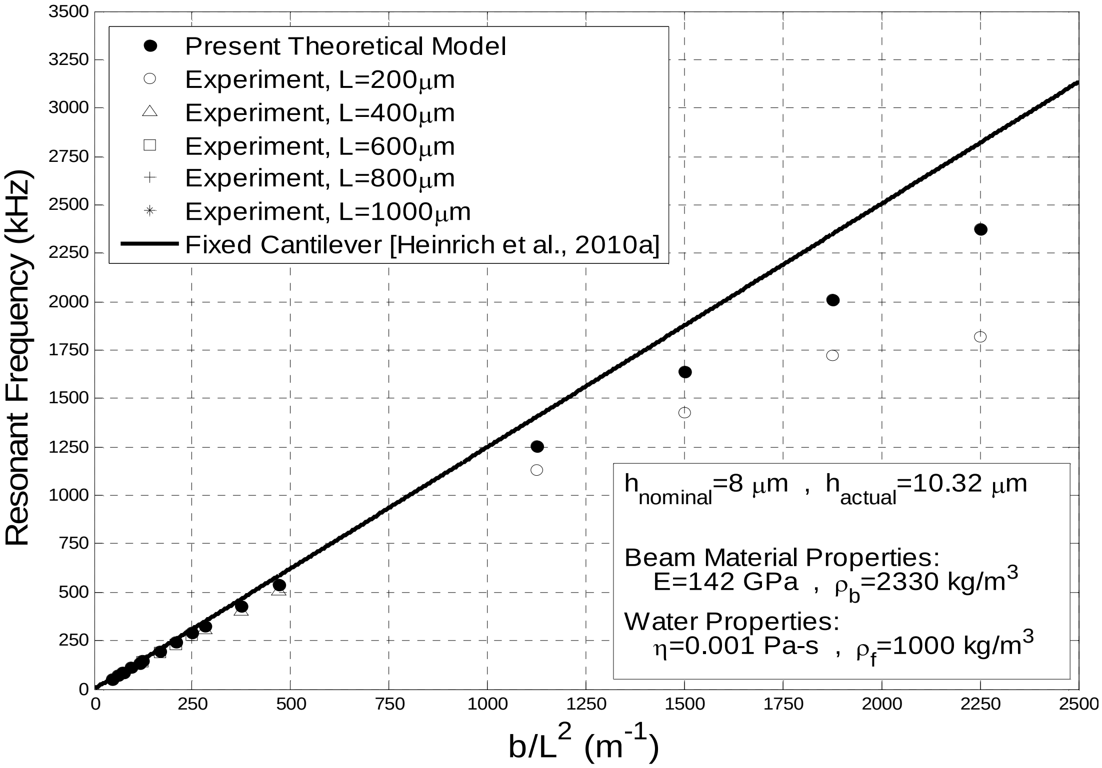
Present Theoretical Model
Experiment, L=200μm
Experiment, L=400μm
Experiment, L=600μm
Experiment, L=800μm
Experiment, L=1000μm
Fixed Cantilever [Heinrich et al., 2010a]
h_nominal=8 μm , h_actual=10.32 μm
Beam Material Properties:
E=142 GPa , ρ_b=2330 kg/m^3
Water Properties:
η=0.001 Pa-s , ρ_f=1000 kg/m^3
Resonant Frequency (kHz)
b/L^2 (m^-1)
0
250
500
750
1000
1250
1500
1750
2000
2250
2500
2750
3000
3250
3500

(b)

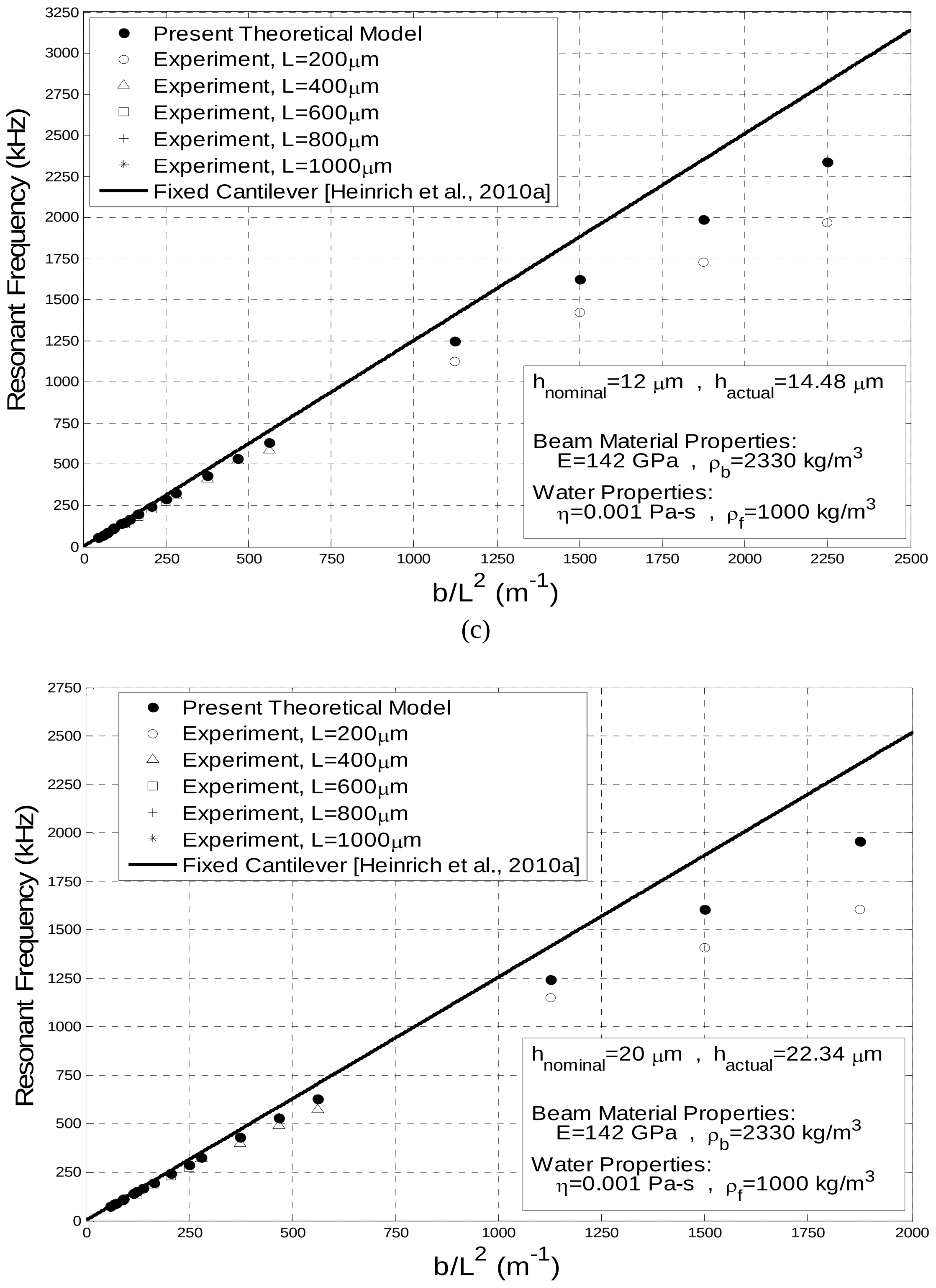

(c)

(d)

Figure 6-16: Fundamental lateral resonant frequency comparisons: current model, fixed cantilever model [Heinrich et al., 2010a], and experimental data for the following nominal Si thicknesses: (a) 5 μm; (b) 8 μm; (c) 12 μm; (d) 20 μm.

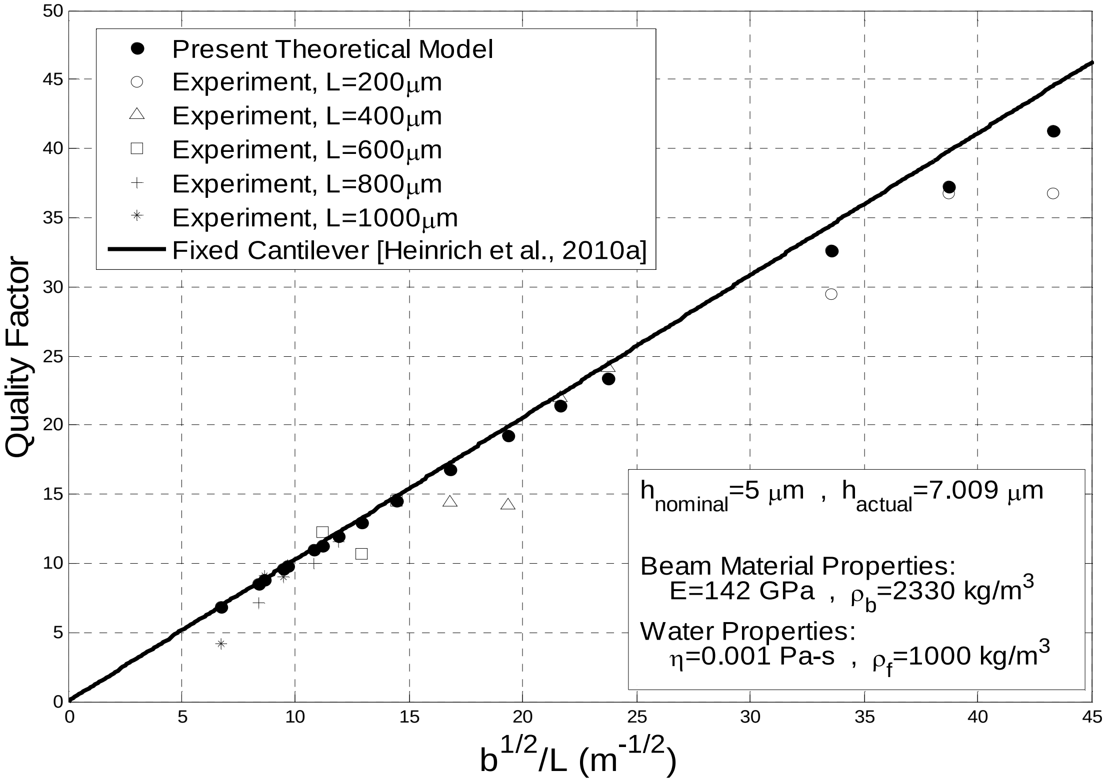
Quality Factor
$b^{1/2}/L$ ($m^{-1/2}$)
0
5
10
15
20
25
30
35
40
45
50
● Present Theoretical Model
○ Experiment, L=200μm
△ Experiment, L=400μm
□ Experiment, L=600μm
+ Experiment, L=800μm
✳ Experiment, L=1000μm
Fixed Cantilever [Heinrich et al., 2010a]
$h_{nominal}$=5 μm , h_{actual}=7.009 μm
Beam Material Properties:
E=142 GPa , ρ_b=2330 kg/m^3
Water Properties:
η=0.001 Pa-s , ρ_f=1000 kg/m^3

(a)

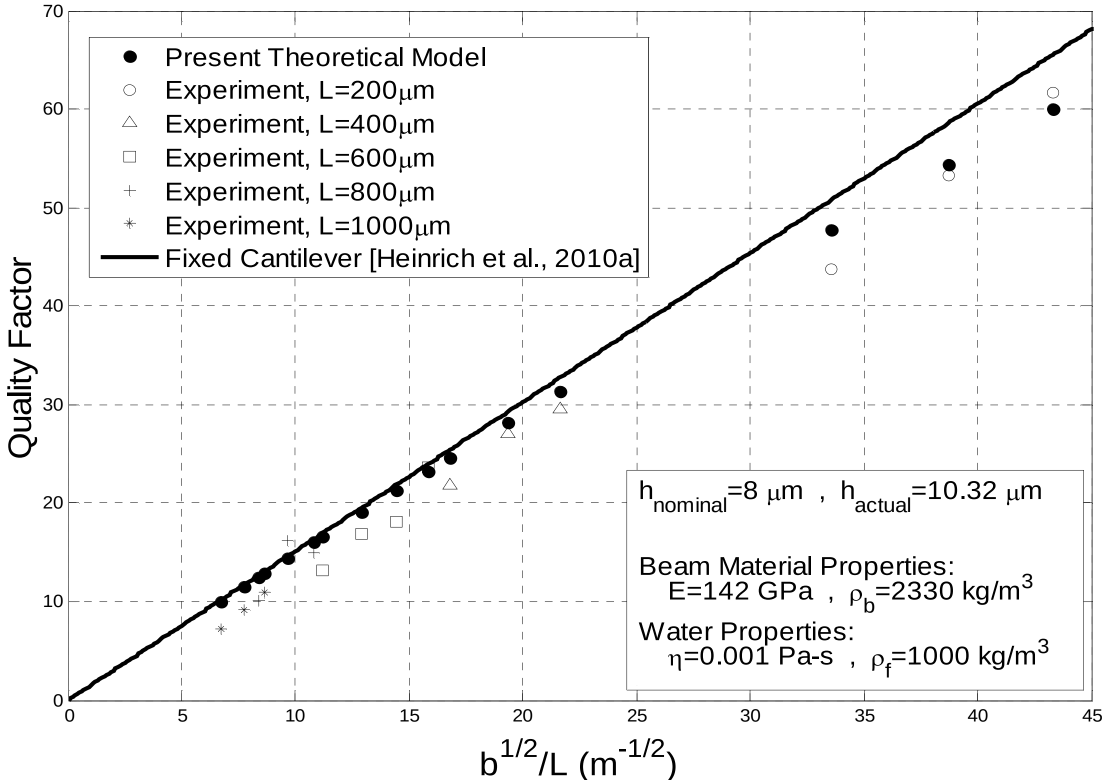
Quality Factor
$b^{1/2}/L$ ($m^{-1/2}$)
0
5
10
15
20
25
30
35
40
45
0
10
20
30
40
50
60
70
● Present Theoretical Model
○ Experiment, L=200μm
△ Experiment, L=400μm
□ Experiment, L=600μm
+ Experiment, L=800μm
✳ Experiment, L=1000μm
Fixed Cantilever [Heinrich et al., 2010a]
$h_{nominal}$=8 μm , h_{actual}=10.32 μm
Beam Material Properties:
E=142 GPa , ρ_b=2330 kg/m^3
Water Properties:
η=0.001 Pa-s , ρ_f=1000 kg/m^3

(b)

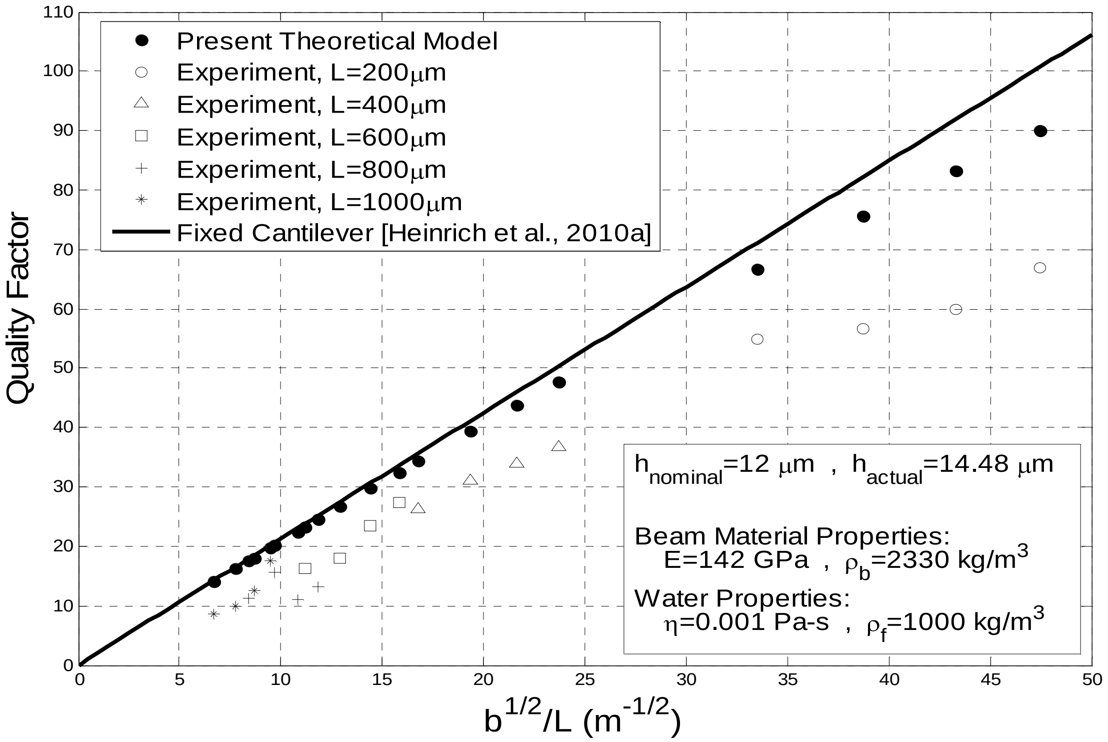

(c)

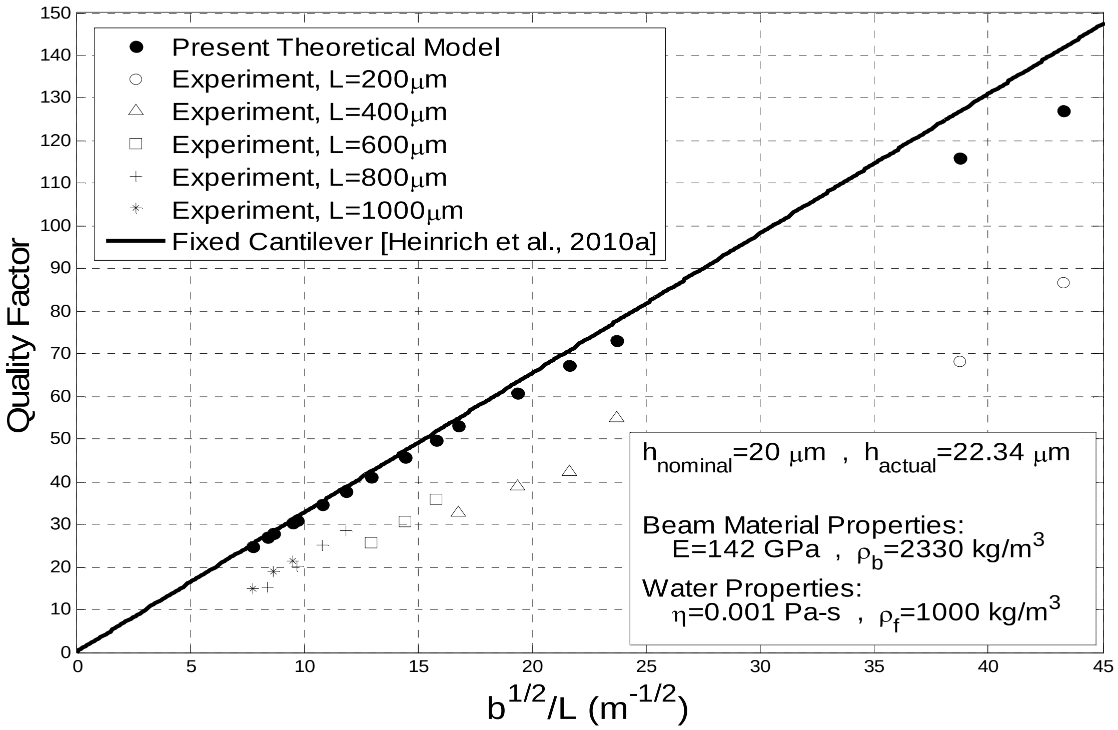

(d)

Figure 6-17: Fundamental lateral quality factor comparisons: current model, fixed cantilever model [Heinrich et al., 2010a], and experimental data for several nominal Si thicknesses: (a) 5 μm; (b) 8 μm; (c) 12 μm; (d) 20 μm.

6.5 Model Verification

To verify the accuracy of the results obtained from the current model, the solutions of the boundary value problems (BVPs) for free vibration and forced vibration, the latter via relative harmonic support rotation near the support, are compared to numerical solutions obtained via the MATLAB bvp4c solver [Mathworks Inc., 2010]. For the free-vibration case the mode shapes (up to the third mode) are generated by solving the eigenvalue problem defined by Eqs. (4-6) and (4-7a-d) using bvp4c. (The value of the eigenvalue α was specified in Eq. (4-6) and determined by numerically obtaining the first three positive real roots of the characteristic equation given by Eq. (4-14) for a specified value of $1/\bar{k}$.) Similarly, for the forced-vibration case the complex vibrational shape is generated near the first resonance peak by using bvp4c to solve the forced vibration BVP defined by Eqs. (4-42) and (4-43a-d). The resulting mode shapes and vibrational shapes from MATLAB are then compared with their counterparts obtained from the theoretical modeling using Eqs. (4-22a) and (4-46) respectively to verify the validity of the analytical solutions obtained herein. The MATLAB programs used to generate these results are included in Appendix D.

Figure 6-18 shows the comparison of the normalized mode shapes for up to the third mode, obtained by using Eq. (4-22a) and by the MATLAB bvp4c solver for $1/\bar{k} \in [0, 0.15]$. The two methods show consistent agreement and hence verify the accuracy of the analytical free-vibration solution obtained using the current theoretical model. Figures 6-19a and 6-19b, respectively, show the real and imaginary parts of the complex vibrational shape for the forced-vibration case, obtained via Eq. (4-46) and via the MATLAB bvp4c solver. There is complete agreement between the vibrational shapes obtained via the two methods, thus verifying the methodology used in this work to obtain the solutions for the present theoretical model.

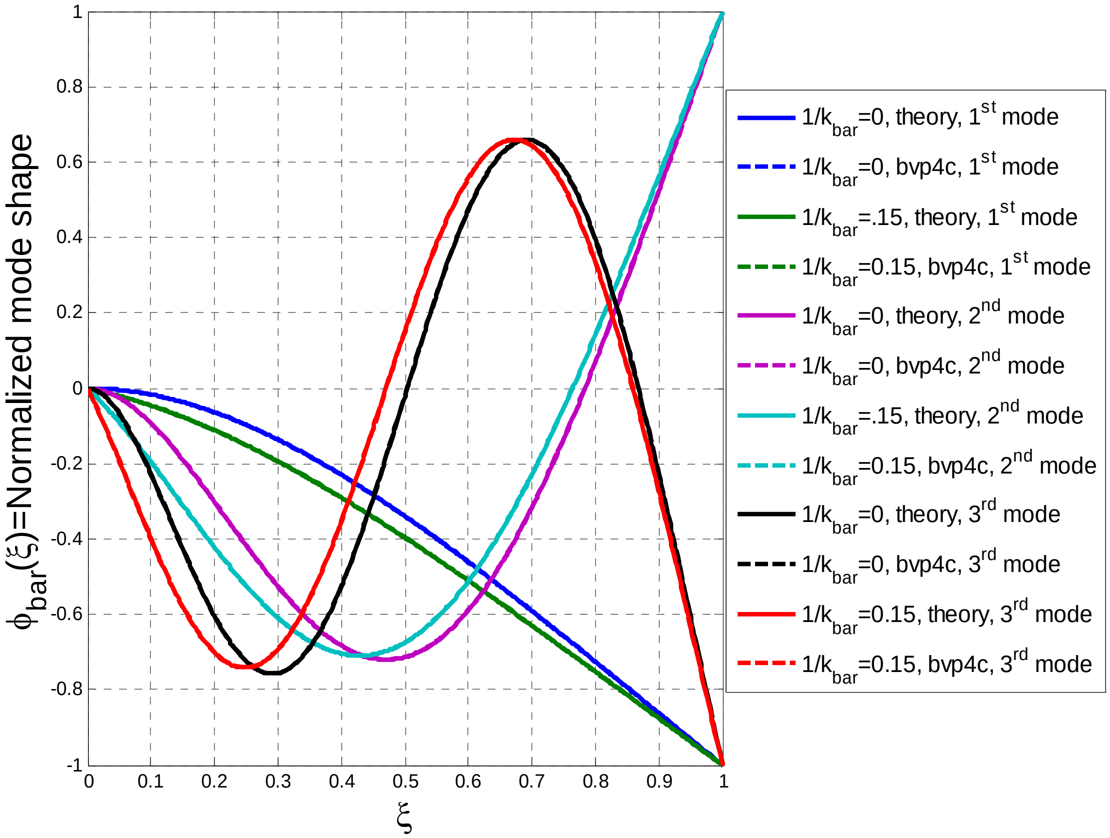

Figure 6-18: Normalized mode shapes for the lateral vibration of an elastically supported microcantilever in a viscous fluid. (Mode shapes are independent of the fluid resistance parameter ζ.)

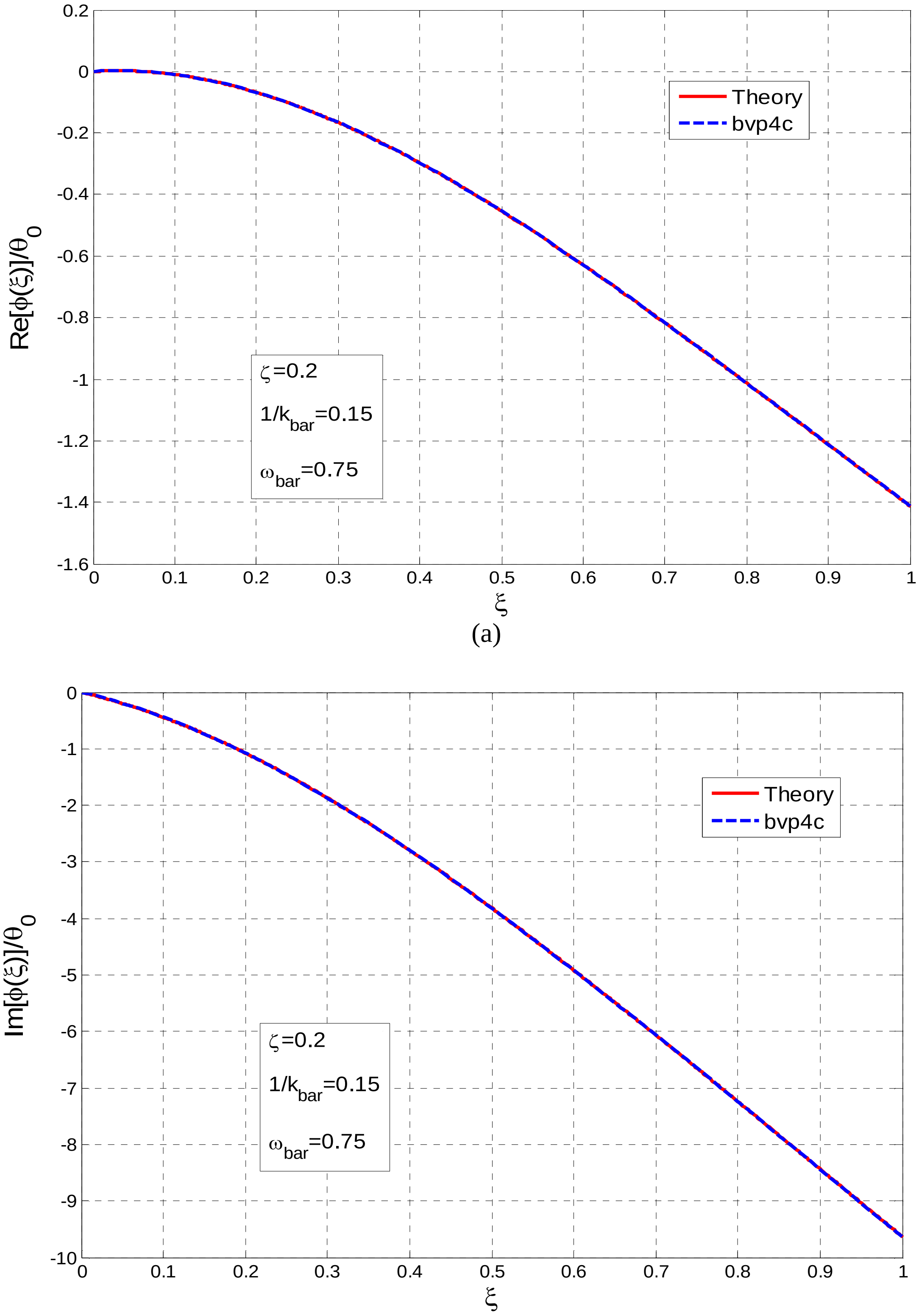

(a)

(b)

Figure 6-19: Vibrational shape for the lateral vibration of an elastically supported microcantilever in a viscous fluid due to an imposed relative harmonic rotation near the support: (a) real part; (b) imaginary part.

CHAPTER 7

APPLICATION OF RESULTS TO MICROCANTILEVER-BASED CHEMICAL SENSORS

7.1 Introductory Remarks

In Ch. 6 the results for resonant frequency and quality factor were presented and the impact of support compliance and fluid resistance on these resonant characteristics was studied. These results for resonant frequency and quality factor can be related to the performance metrics of microcantilever-based sensors – namely, mass sensitivity, chemical sensitivity, and limit of detection (LOD). In this chapter these sensor performance metrics are defined and related to the resonant characteristics, and the practical implications are discussed with the main focus being on impact of support compliance on sensor performance.

7.2 Mass Sensitivity

The resonant frequency of a microcantilever changes with the change in its mass and this change in resonant frequency can be monitored. The degree to which a resonant sensor changes its resonant frequency upon mass uptake is known as the mass sensitivity of the sensor. In general, the mass sensitivity is the ratio of the shift in resonant frequency to the change in mass of the sensor caused by analyte adsorption/absorption. Thus, the mass sensitivity can be defined mathematically as [Narducci et al., 2008]

$$S_m = \left| \frac{\partial f_{res}}{\partial m} \right|, \tag{7-1}$$

where f_{res} = the resonant frequency (Hz) and m = the total mass of the cantilever. Thus, the mass sensitivity as defined by Eq. (7-1) represents the rate of change of resonant frequency with respect to sorbed analyte mass.

Using Eq. (3-13) for the fundamental natural frequency in vacuum for a perfectly fixed lateral-mode cantilever, the dimensionless natural (circular) frequency for first resonance, given by Eq. (6-1), can be written in terms of resonant frequency (in units of Hz). Assuming that the resonant frequency may be approximated by the natural frequency, this gives

$$f_{res1} = \frac{\lambda_1^2}{2\pi}\frac{b}{L^2}\sqrt{\frac{E}{12\rho_b}}\left[1 - \frac{1.909}{\frac{L}{b}\frac{b}{h}\left(0.2088 + \frac{2.710}{(b/h)}\right)} + \frac{3.417}{\left(\frac{L}{b}\frac{b}{h}\left(0.2088 + \frac{2.710}{(b/h)}\right)\right)^2} - 0.7019\left(1 - \frac{1}{\frac{L}{b}\frac{b}{h}\left(0.2088 + \frac{2.710}{(b/h)}\right)}\right)\sqrt{\frac{L_0}{h}}\frac{L}{b}\sqrt{\frac{b}{h}}\right] . \tag{7-2}$$

Placing Eq. (7-2) into Eq. (7-1) results in the following expression for mass sensitivity, which is based on the assumption that the added mass is uniformly distributed along the length of the beam:

$$S_m = \sqrt{\frac{E}{\rho_b^3}}\frac{1}{h^4}\frac{1}{\left(\frac{L}{b}\right)^2\left(\frac{b}{h}\right)^{5/2}}\left|\frac{-0.0808}{\frac{L}{b}\sqrt{\frac{b}{h}}}\left(1 - \frac{1.909}{\frac{L}{b}\frac{b}{h}\left(0.2088 + \frac{2.710}{(b/h)}\right)} + \frac{3.417}{\left(\frac{L}{b}\frac{b}{h}\left(0.2088 + \frac{2.710}{(b/h)}\right)\right)^2}\right) + 0.1418\sqrt{\frac{L_0}{h}}\left(1 - \frac{1}{\frac{L}{b}\frac{b}{h}\left(0.2088 + \frac{2.710}{(b/h)}\right)}\right)\right| . \tag{7-3}$$

It is important to note that Eq. (7-2) and, thus, Eq. (7-3) are valid only if they satisfy the inequalities for L/b and b/h given by Eqs. (6-2) and (6-3), respectively. The expression (7-3) clearly shows that the mass sensitivity may be increased if the Young's modulus of beam material is increased or if the thickness of the beam or the density of the beam material is decreased. Moreover, the thickness of the beam has the greatest impact on mass sensitivity followed by the density of the beam material and then the Young's modulus of the beam material. Also, for a fixed thickness the first-order behavior of the mass sensitivity decreases with an increase in the L/b and b/h ratios. Note that it is clear from Eq. (7-3) that, to first order, the mass sensitivity increases by four orders of magnitude for every one order of magnitude for which the dimensions are scaled down. Equation (7-3) can be normalized by $\sqrt{\frac{E}{\rho_b{}^3}\frac{1}{h^4}}$ to obtain the following expression for normalized mass sensitivity in terms of the relative size of the cantilever dimensions and the characteristic material length:

$$\frac{S_m}{\sqrt{\frac{E}{\rho_b{}^3}\frac{1}{h^4}}} = \frac{1}{\left(\frac{L}{b}\right)^2\left(\frac{b}{h}\right)^{5/2}} \left| \frac{-0.0808}{\frac{L}{b}\sqrt{\frac{b}{h}}} \left(1-\frac{1.909}{\frac{L}{b}\frac{b}{h}\left(0.2088+\frac{2.710}{(b/h)}\right)}+\frac{3.417}{\left(\frac{L}{b}\frac{b}{h}\left(0.2088+\frac{2.710}{(b/h)}\right)\right)^2}\right) + 0.1418\sqrt{\frac{L_0}{h}}\left(1-\frac{1}{\frac{L}{b}\frac{b}{h}\left(0.2088+\frac{2.710}{(b/h)}\right)}\right)\right| . \tag{7-4}$$

As an illustrative example, consider the case in which the cantilever is made of silicon (E=169 GPa and $\rho_b = 2330$ kg/m^3), has a thickness $h \in [5,\ 20]\ \mu\text{m}$, and is operating in water ($\rho_f = 1000$ kg/m^3, $\eta = 0.001$ Pa·s). Then the value of $\sqrt{L_0/h}$ is very small ($\sqrt{L_0/h} = 0.0021$ for $h = 5$ μm) and, thus, for many geometries of practical interest the second term in Eq. (7-4) becomes negligible compared to the first term. This means that the mass sensitivity is insensitive to the effects of the surrounding liquid (water in this example). Ignoring this term, Eq. (7-4) can be simplified as

$$\frac{S_m}{\sqrt{\frac{E}{\rho_b{}^3}\frac{1}{h^4}}} = \left| \frac{-0.0808}{\left(\frac{L}{b}\right)^3\left(\frac{b}{h}\right)^3} \left(1 - \frac{1.909}{\frac{L}{b}\frac{b}{h}\left(0.2088 + \frac{2.710}{(b/h)}\right)} + \frac{3.417}{\left(\frac{L}{b}\frac{b}{h}\left(0.2088 + \frac{2.710}{(b/h)}\right)\right)^2} \right) \right| . \qquad (7\text{-}5)$$

This normalized mass sensitivity expression is now applicable for a silicon beam in water, provided that $h \geq 5$ μm and the parameter range constraints [Eqs. (6-2) and (6-3)] are not violated. (It should also be relevant for many other beam materials and liquids.) The normalized mass sensitivity for a perfectly fixed cantilever can be obtained by setting the term within large parentheses to unity, i.e.,

$$\frac{S_{m,\,fixed}}{\sqrt{\frac{E}{\rho_b{}^3}\frac{1}{h^4}}} \approx \frac{0.0808}{\left(\frac{L}{b}\right)^2\left(\frac{b}{h}\right)^3} . \qquad (7\text{-}6)$$

The normalized mass sensitivity for both the compliant-support case and the limiting case of a fixed support are plotted in Fig. 7-1 versus L/b for different b/h values. From the plot it can be seen that the normalized mass sensitivity is larger for the perfectly fixed case, as expected, due to its higher resonant frequency. At larger L/b ratios, the mass sensitivity decreases toward zero because the resonant frequency is becoming smaller as the beam becomes more flexible. At smaller L/b ratios, i.e., stiffer cantilevers, the mass sensitivity becomes larger as is evident from the figure and the associated analytical expression. Also, as evident from Eq. (7-5), the mass sensitivity

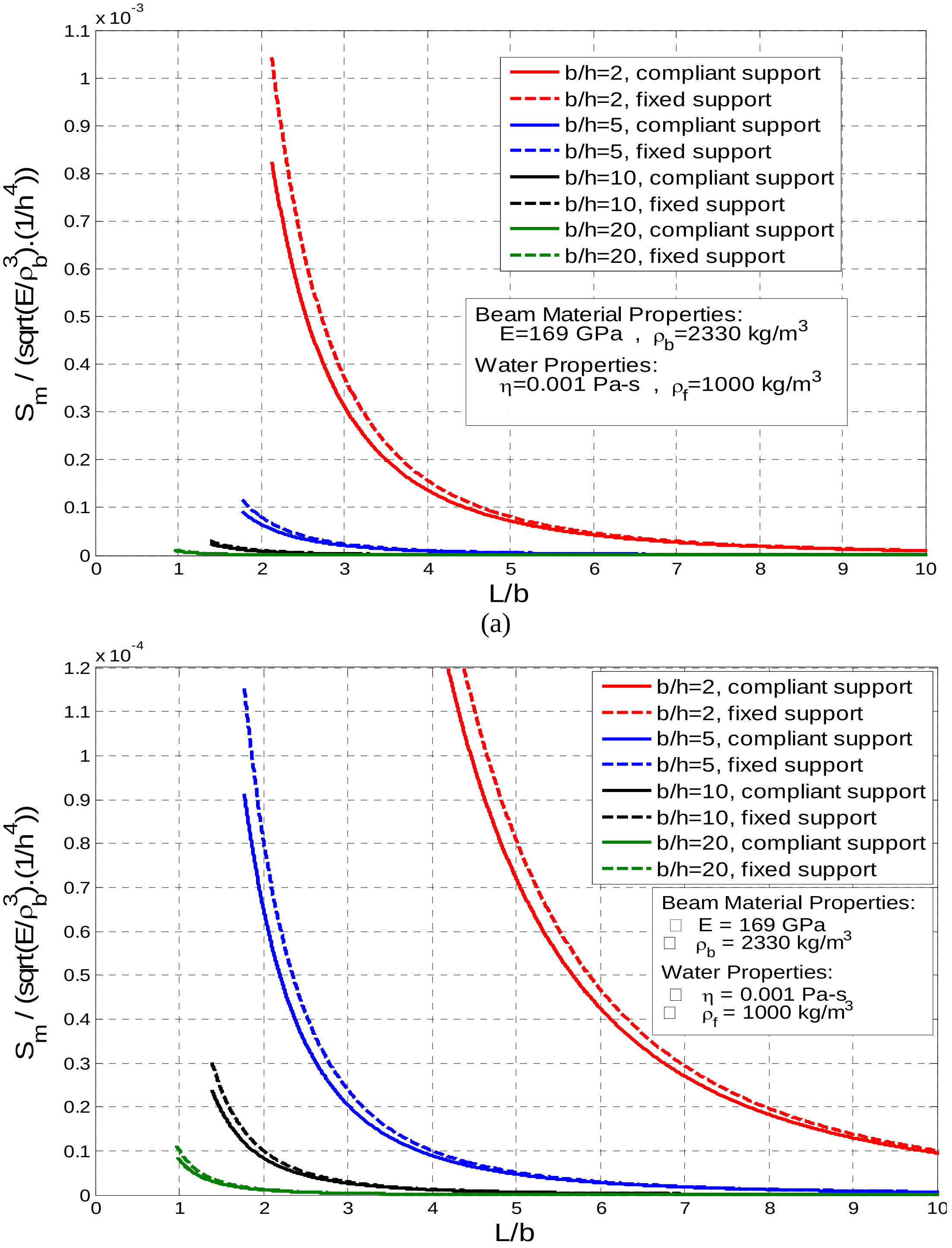

(a)

(b)

Figure 7-1: Normalized mass sensitivity of laterally vibrating silicon microcantilevers with $h > 5\,\mu\text{m}$ in water: (a) $S_m / \sqrt{\frac{E}{\rho_b^3}\frac{1}{h^4}} \in [0, 0.0011]$; (b) $S_m / \sqrt{\frac{E}{\rho_b^3}\frac{1}{h^4}} \in [0, 0.00012]$ (zoomed view). These figures should NOT be applied for L/b ratios in excess of the upper bound listed in Eq. (6-2).

decreases with an increase in the b/h ratio. Figure 7-2 shows the percent decrease in the mass sensitivity of silicon cantilevers operating in water having thickness $h \geq 5$ μm due to the support compliance effects, according to Eq. (7-5). The curves indicate a 21% decrease in mass sensitivity at the lower limits of L/b for all b/h ratios considered. The percent drop due to support compliance decreases with an increase in the b/h ratio. For the range of b/h considered, the difference in S_m between the fixed and compliant-support cases is less that 4% if $L/b > 15$. (This limiting value of L/b is governed by the results for $b/h = 2$.) It is also to be noted that for lower L/b values the Timoshenko beam effects, which have not been considered here, might play an important role. Even more complex effects associated with 2-D and 3-D deformations of the structure may come into play as the structure becomes so short that it may no longer behave as a "beam."

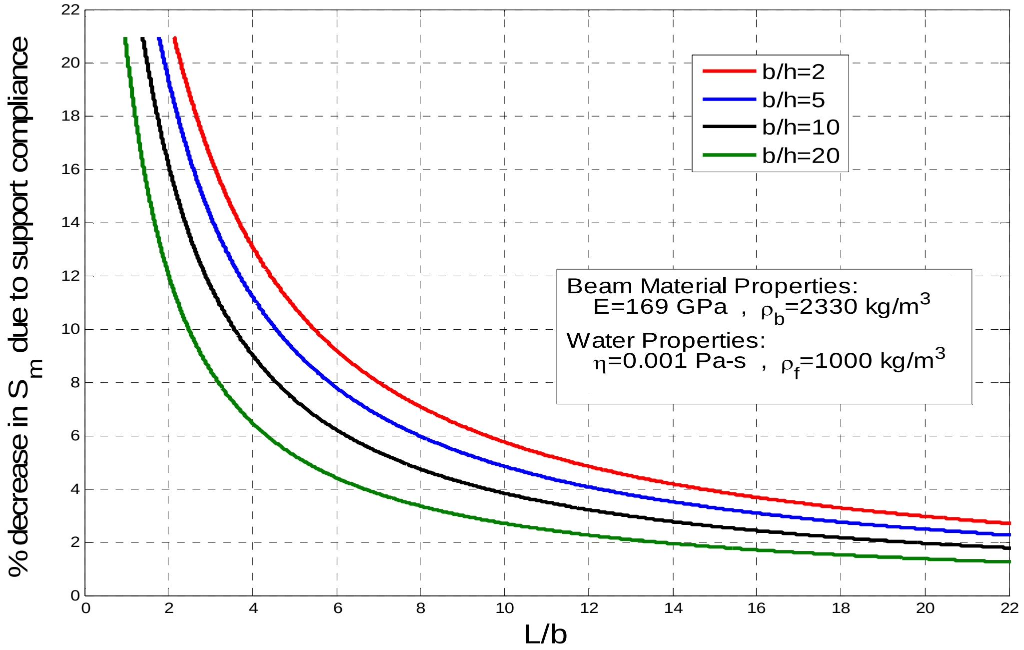

Figure 7-2: Percent decrease in mass sensitivity of laterally vibrating microcantilever-based sensors made of silicon operating in water due to the support compliance effect. This figure should NOT be applied for L/b ratios in excess of the upper bound listed in Eq. (6-2).

7.3 Chemical Sensitivity

Chemical sensitivity is another important sensor performance metric. It is the ratio of the change in resonant frequency to the change in analyte concentration in the surrounding environment. It can be defined as [e.g., Dufour et al., 2004; Cox, 2011, Schultz, 2012]

$$S_c = \left|\frac{\partial f_{res}}{\partial C_A}\right|, \tag{7-7}$$

where C_A is the ambient concentration of analyte.

The chemical sensitivity can be related to the mass sensitivity [e.g., Cox, 2011; Schultz, 2012] as

$$S_c = K V_c S_m, \tag{7-8}$$

where K is the partition coefficient of the particular coating/analyte combination in the particular operational medium, and V_c is the volume of the chemically sensitive layer. Thus, if K is known, then the expression for S_c can be obtained by multiplying Eq. (7-3) by KV_c. A similar study on the impact of beam parameters on S_c may be done as was illustrated in the previous section for S_m, but will not be performed here. It is important to note that V_c is dependent on cantilever geometry and, thus, the impact of the dimensions on chemical sensitivity will differ from that on mass sensitivity presented in Sect. 7-2.

7.4 Limit of Detection

Another important metric of sensor performance is the resolution of the sensor, i.e., its limit of detection (LOD). The limit of detection is defined as the ambient analyte concentration corresponding to a frequency shift equal to three times the frequency noise of the system measurement [e.g., Lochon et al., 2005]. Thus, LOD can be expressed as

$$LOD = \frac{3\Delta f_{noise}}{S_c}, \tag{7-9}$$

where Δf_{noise} is the frequency noise of the system. When operating in an oscillator feedback loop configuration, the frequency noise of the system is proportional to the ratio of the resonant frequency to the quality factor [e.g., Lochon et al., 2005; Cox, 2011; Schultz, 2012]:

$$\Delta f_{noise} \propto \frac{f_{res}}{Q}. \tag{7-10}$$

It follows from Eqs. (7-9) and (7-10) that the LOD is directly proportional to f_{res} and inversely proportional to Q and S_c :

$$LOD \propto \frac{f_{res}}{Q\, S_c} \frac{dy}{dx}. \tag{7-11}$$

Using Eq. (5-17) for Q, Eq. (7-2) for f_{res}, and Eq. (7-8) for S_c, an expression for the LOD dependence may be obtained and a parametric study performed. However, such a study is deemed outside the scope of the present work.

CHAPTER 8
SUMMARY, CONCLUSIONS AND RECOMMENDATIONS FOR FUTURE WORK

8.1 Summary

An improved continuous-system analytical model has been derived for the lateral (in-plane) vibration of a microcantilever beam in a viscous fluid, incorporating the effects of support compliance and fluid properties. This work was motivated by the fact that the there were discrepencies between the ideally clamped cantilever models and experimental measurements and these discrepancies were more pronounced for those geometries that have the most promise for sensing applications. Boundary value problems (BVPs) were formulated for the in-fluid free-vibration case and the in-fluid forced-vibration case in which the latter involved excitation caused by a harmonic relative rotation imposed near the support. This load type was considered as it simulates electrothermal excitation of the type that was employed in associated experimental testing. The fluid effects were incorporated in the model via a Stokes-type fluid-resistance assumption.

Exact solutions to the BVPs were obtained in analytical form and from these solutions approximate analytical expressions for the natural/resonant frequency and quality factor were derived. For the forced vibration case, the results were obtained by considering two methods of vibration detection – tip deflection and bending strain at the root of beam. Resonant frequencies were obtained from the frequency response curves as were the quality factors via the -3dB bandwidth. The practical utility of the solutions derived was enhanced by quantifying the rotational stiffness of the support in terms of system parameters by performing a combination of dimensional analysis, 3-D finite element analysis, and curve-fitting of the simulation results.

The impact of the fluid resistance and the beam geometry on the natural/resonant frequency and quality factor of the beam, including the influence of support compliance, was studied in detail. The theoretical frequency and quality factor predictions from the new model were compared to the previously derived models found in the literature and with experimental data spanning a broad range of microscale dimensions for laterally vibrating microcantilevers in water. The derived analytical results were also related to the performance metrics (mass sensitivity, chemical sensitivity and limit of detection) of laterally excited microcantilever-based liquid-phase sensors. An analytical expression was obtained for mass sensitivity, which clearly showed the impact of beam geometry, including the effects of support compliance and fluid resistance. Analogous expressions for chemical sensitivity and LOD may easily be obtained as noted at the end of Ch. 7.

8.2 Conclusions

The following conclusions may be drawn from the research work presented in this dissertation:

1) For the ranges of support compliance ($1/\bar{k} \in [0,\ 0.15]$) and fluid resistance parameter ($\zeta \in [0,\ 1]$) considered, the support compliance effects may cause up to a 21% decrease in the fundamental lateral-mode natural/resonant frequency, while the fluid resistance may cause up to a 25% decrease in the fundamental lateral-mode natural/resonant frequency. The magnitude of these decreases in natural frequency is reduced with an increase in the mode number. For

example, for the third mode the maximum drop in natural frequency was found to be only 12% due to support effects and 7% due to fluid effects. The model also shows that the quality factor increases with increasing mode number. Thus, if higher modes can be excited, the adverse effects of support compliance and fluid resistance will be less significant.

2) For the practical ranges of parameters given by $1/\bar{k} \in [0,\ 0.15]$, $\zeta \in [0,\ 0.6]$, $b/h = [2,\ 20]$, $h \in [5,\ 20]\ \mu\text{m}$, the model indicates that, at smaller L/b values, support compliance may reduce the lateral-mode quality factor Q by up to ~14% and the lateral-mode resonant frequency f_{res} by up to ~21% compared to the fixed cantilever model of Heinrich et al. (2010a). Both of these values occur at the smallest value of b/h considered, i.e., $b/h = 2$. Conversely, for $L/b > 15$ the support compliance effects may decrease Q by no more than 2% and f_{res} by no more than 4%. Thus, for $L/b > 15$, the support effects can be ignored and the fixed cantilever model can be used.

3) For small L/b values the support compliance effect is dominant while for large L/b values the fluid resistance effect is dominant. Due to the existence of these two regimes, the resonant frequency drop (due to the combined effects of support compliance and fluid resistance) acquires a local minimum at a particular L/b value while transitioning from one regime to another.

4) The fundamental lateral resonant frequency as detected by the maximum bending strain signal is nearly equal to that obtained via the tip displacement response for small-to-moderate values of fluid resistance parameter (less than 2% difference for $\zeta \in [0, 0.4]$), with the resonant frequency detected via the

bending strain response being greater than that for the tip displacement signal. Similarly, the quality factor obtained from the two detection methods are essentially the same over this range of ζ, with the tip displacement response yielding a slightly larger Q value.

5) Even though the two detection methods give similar lateral-mode resonant characteristics for small-to-moderate fluid resistance values, the frequency response curves are different for the two detection methods and the resonant peak amplitudes exhibit different trends. For the tip deflection response, the resonant peak amplitudes tend to decrease at higher resonances, thus indicating that the first resonant mode may be the most suitable of the lateral flexural modes for sensing applications that utilize a tip-deflection monitoring scheme. In contrast to the tip detection scheme, the model responses for strain-based detection methods show stronger signal amplitudes at higher modes, thus indicating that, if the higher modes can be excited, this method of detection may have advantages at higher modes in comparison to the fundamental lateral mode.
6) The fundamental lateral-mode resonant frequency obtained via both maximum bending strain detection at the root of the beam and the tip displacement closely resembles fundamental natural frequency for small values of ζ (less than 1% error for $\zeta \in [0, 0.3]$). The lateral-mode quality factor for the free vibration case also compares quite well with the forced vibration quality factors obtained via both detection methods. Thus, the analytical expressions for fundamental natural frequency and fundamental quality factor expressions

can be used to estimate the fundamental resonant frequency and fundamental quality factor for smaller values of ζ on which the present work is mainly focused.

7) The Euler-Bernoulli model with fixed support [Heinrich et al., 2010a, b] overestimates the lateral-mode resonant frequency and quality factor for wider and shorter cantilevers as compared to experimental data. Comparison with experimental measurements shows that the current model, which accounts for support compliance, predicts resonant frequency and quality factor better than the previous ideally clamped cantilever model for the cases of "stubbier" beam geometries.
8) The analytical expression derived for the lateral-mode mass sensitivity shows that it may be increased by increasing the Young's modulus of the beam and/or by decreasing any of the following (in order of decreasing effectiveness): thickness of beam, length-to-width or width-to-thickness ratio of the beam, and mass density of the beam.
9) For a silicon beam operating laterally in water with the thickness range of $h \in [5, 20]\ \mu\text{m}$ considered, the effect of water on mass sensitivity is negligible compared to the effect of support compliance. This is consistent with the fact that a change in stiffness will influence the natural/resonant frequency of a dynamic system more than a change in the damping coefficient.
10) The support compliance effect may cause a decrease of up to 21% in the mass sensitivity of a lateral-mode silicon microcantilever in water over the range $h \in [5, 20]\ \mu\text{m}$, with the larger influence occuring at smaller L/b ratios. For

increasing values of L/b, the influence of support compliance on mass sensitivity decreases; for $L/b > 15$, the drop in mass sensitivity is less than 4% compared to the fixed cantilever result.

It is important to emphasize that the above conclusions were based on a theoretical model that was based on (a) Bernoulli-Euler beam theory and (b) a Stokes-type fluid resistance model. Thus, the model does not account for Timoshenko beam effects (shear deformation and rotatory inertia), warping of cross sections or other three-dimensional deformation patterns in the cantilever, or the pressure and edge effects associated with the beam/fluid interaction. Because these neglected effects become more significant at lower L/b and b/h ratios, the above conclusions should not be used without regard for the limitations imposed by the model's underlying assumptions, i.e., they should be interpreted as "first-order guidelines" at the lower end of the L/b and b/h ranges considered.

8.3 Recommendations for Future Work

The following recommendations for future work are made to expand upon the present study:

1) While showing marked improvement over previous modeling efforts based on perfectly clamped cantilevers, the resonant frequency and quality factor predicted by the current model overpredict experimental measurements for shorter and wider beams. In addition to exhibiting support compliance effects, beams with these geometries tend to have larger shear deformation and rotational inertia effects, which were not considered in the present model. Thus, it is recommended that the support compliance expression derived herein

be incorporated into a Timoshenko beam model such as that recently developed by Schultz (Schultz, 2012; Schultz et al., 2013a, b). This will permit both support compliance and Timoshenko effects to be accounted for and the relative contributions of these effects to be determined.

2) In this study the fluid effects have been modeled via a Stokes-type fluid resistance assumption which ignores the pressure effects of the fluid on the smaller sides of the beam and edge effects in the fluid shear stress near the corners of the beam cross section. This assumption is expected to become less valid as the beam thickness increases (relative to the width) as is evident from the larger discrepencies for smaller b/h values between the analytical results and experimental measurements for resonant frequency and, to an even greater extent, for quality factor. Thus, incorporating more accurate hydrodynamic functions, such as those derived by Brumley et al. (2010) and Cox et al. (2012), to model the fluid effects on the beam will account for the fluid effects that have been neglected here and, thus, yield lower, more accurate resonant frequency and quality factor values in liquids for the geometries in question.
3) The increase in resonant peak amplitudes at higher modes based on use of a bending strain signal is of potential interest. This method of detection is used in piezoresistive read-out methods. Furthur investigation into higher lateral modes, especially experimental work to activate these modes, might give rise to some significant improvements in lateral–mode microcantilever-based sensor performance.

4) This dissertation included a derivation of a detailed expression showing the dependence of mass sensitivity on device geometry and system (beam and liquid) material properties. Similar expressions may be easily derived (following the roadmap suggested in Sect. 7.2) for chemical sensitivity and limit of detection in order to better understand the effects of support compliance and fluid resistance on these very important sensor performance metrics. These expressions, including that for mas sensitivity included here, would provide the basis for a through parametric study to be performed in order to provide more detailed guidelines for lateral-mode sensor design.

REFERENCES

ANSYS Version 13, ANSYS Inc., Canonsburg, PA, 2013.

Barnes, J., Stephenson, R., Welland, M., Gerber, C., and Gimzewski, J., "Photothermal Spectroscopy with Femtojoule Sensitivity Using a Micromechanical Device, *Nature*, Vol. 372, No. 6501, 1994, pp. 79-81.

Basak, S., Raman, A., and Garimella, S., "Hydrodynamic Loading of Microcantilevers Vibrating in Viscous Fluids," *Journal of Applied Physics*, Vol. 99, 2006, pp. 114906 – 114906-10.

Beardslee, L.A., Josse, F., Heinrich, S.M., Dufour, I., and Brand, O., "Geometrical Considerations for the Design of Liquid-Phase BioChemical Sensors Using a Cantilever's Fundamental In-Plane Mode," *Sensors and Actuators B*, 2012, pp. 7-14.

Beardslee, L.A., Truax, S., Su, J.-J., Heinrich, S.M., Josse, F., Brand, O., "On the Relative Sensitivity of Mass-Sensitive Chemical Microsensors," *Proc., Transducers '11, 16th International Conference on Solid-State Sensors, Actuators and Microsystems*, Beijing, China, June 5-9, 2011, 5 pp.

Beardslee, L.A., Addous, A.M., Demirci, K.S., Heinrich, S.M., Josse, F., and Brand, O., "Geometrical Optimization of Resonant Cantilevers Vibrating in In-Plane Bending Mode," *Proceedings, IEEE Sensors 2010 Conference*, Waikoloa, Hawaii, November 1-4, 2010a, pp. 1996-1999.

Beardslee, L., Addous, A., Heinrich, S., Josse, F., Dufour, I., and Brand, O., "Thermal Excitation and Piezoresistive Detection of Cantilever In-Plane Resonance Modes for Sensing Applications," *Journal of Microelectromechanical Systems*, Vol. 19, No. 4, 2010b, pp. 1015-1017.

Beardslee, L.A., Demirci, K.S., Luzinova, Y., Mizaikoff, B., Heinrich, S.M., Josse, F., and Brand, O., "Liquid-Phase Chemical Sensing Using Lateral Mode Resonant Cantilevers," *Analytical Chemistry*, Vol. 82, 2010c, pp. 7542-7549.

Beardslee, L.A., Demirci, K.S., Luzinova, Y., Su, J.J., Mizaikoff, B., Heinrich, S., Josse, F., and Brand, O., "In-Plane Mode Resonant Cantilevers as Liquid-Phase Chemical Sensors with PPB Range Limits of Detection," *Proc., Hilton Head Workshop 2010: A Solid-State Sensors, Actuators and Microsystems Workshop*, Hilton Head, SC, June 6-10, 2010d, 4 pages.

Beardslee, L.A. and Brand, O., "Personal Communication - Raw Data," 2010.

Binnig, G., Quate, C.F. and Gerber, C., “Atomic Force Microscope,” *Physics Review Letters,* Vol. 56, No. 9, March 1986, pp.930-933.

Boisen, A., Dohn, S., Keller, S. S., Schmid, S. and Tenje M., “Cantilever-like Micromechanical Sensors,” *Reports on Progress in Physics*, Vol. 74, February 2011, 30 pages.

Brumley, D., Willcox, M., and Sader, J., “Oscillation of Cylinders of Rectangular Cross Section Immersed in Fluid,” *Physics of Fluids*, Vol. 22, 2010, pp. 052001-052001-15.

Cai, T., Josse, F., Dufour, I., Heinrich, S.M., Nigro, N., Brand, O., “Resonant Characteristics of Rectangular Microcantilevers Vibrating Torsionally in Viscous Liquid Media,” *Frequency Control Symposium (FCS), 2012 IEEE International*, 21-24 May 2012, pp. 1-6.

Castille, C., Dufour, I., and Lucat, C., “Longitudinal Vibration Mode of Piezoelectric Thick-Film Cantilever-Based Sensors in Liquid Media,” *Applied Physics Letters,* Vol. 96, 2010, 3 pages.

Chon, J., Mulvaney, P., and Sader, J., “Experimental Validation of Theoretical Models for the Frequency Response of Atomic Force Microscope Cantilever Beams Immersed in Fluids,” *Journal of Applied Physics*, Vol. 87, No. 8, April 2000, pp. 3978-3988.

Clough, R.W., and Penzien, J., “Dynamics of Structures,” Thire Edition, Computers & Structures, Inc., 2003.

Cook, R.D., “Beam Cantilevered from Elastic Support: Finite Element Modeling,” *Communications in Applied Numerical Methods*, Vol. 7, 1991, pp. 621-623.

Cox, R., Josse, F., Heinrich, S., Brand, O., and Dufour, I., “Characteristics of Laterally Vibrating Resonant Microcantilevers in Viscous Liquid Media,” *Journal of Applied Physics*, Vol. 111, January, 2012, pp. 014907 - 014914.

Cox, R., “Theoretical Analysis of Laterally Vibrating Microcantilever Sensors in a Viscous Liquid Medium,” *Doctoral Dissertation*, May 2011, Marquette University, Wisconsin, USA.

Cox, R., Josse, F., Wenzel, M., Heinrich, S.M., and Dufour, I., “Generalized Model of Resonant Polymer-Coated Microcantilevers in Viscous Liquid Media,” *Analytical Chemistry*, Vol. 80, 2008, pp. 5760-5767.

Dufour, I., Josse, F., Heinrich, S., Lucat, C., Ayela, C., Menil, F., and Brand, O., “Unconventional Uses of Microcantilevers as Chemical Sensors in Gas and Liquid Media,” *Sensors and Actuators B*, Vol. 170, 2012, pp. 115-121.

Dufour, I., Josse, F., and Heinrich, S., “Theoretical Analysis of Strong-Axis Bending Mode Vibrations for Resonant Microcantilever (Bio) Chemical Sensors in Gas or Liquid Phase” *Journal of Micromechanical Systems*, Vol. 16, No. 1, 2007a, 44-49.

Dufour, I., Lochon, F., Heinrich, S.M., Josse, F., and Rebière, D., “Effect of Coating Viscoelasticity on Quality Factor and Limit of Detection of Microcantilever Chemical Sensors,” *IEEE Sensors Journal*, Vol. 7, No. 2, February, 2007b, pp. 230-236.

Dufour, I., Heinrich, S.M., and Josse, F., “Strong-Axis Bending Mode Vibrations for Resonant Microcantilever (Bio) Chemical Sensors in Gas or Liquid Phase,” *Proceedings, 2004 IEEE* 151 *International Ultrasonics, Ferroelectrics, and Frequency Control 50th Anniversary Joint Conference*, 6 pp., Montreal, Canada, August 24-27, 2004.

Fadel-Taris, L, Ayela, C., Josse, F., Heinrich, S.M., Brand, O., Saya, D., and Dufour, I., “Influence of Non-Ideal Clamping in Microcantilever Resonant Frequency Estimation,” *Proc., IEEE International Frequency Control Symposium*, San Francisco, CA, May 1-5, 2011, 5 pages.

Finot, E., Passian, A., and Thundat, T., “Measurement of Mechanical Properties of Cantilever Shaped Materials,” *Sensors*, Vol. 8, 2008, pp. 3497-3541.

Fox, R.W. and McDonald, A.T., “Introduction to Fluid Mechanics”, Inc., Fourth Edition, John Wiley and Sons, 1993.

Gere, J.M. and Timoshenko, S.P., “Mechanics of Materials,” Second Edition, Brooks/Cole Engineering, 1984.

Ghatkesar, M.K., Braun T., Barwich, V., Ramseyer, J., Gerber, C., Hegner, M., and Lang, H., “Resonating Modes of Vibrating Microcantilevers in Liquid” *Applied Physics Letters*, Vol. 92, 2008, pp. 92-94.

Green, C.P., and Sader, J.E., “Small Amplitude Oscillations of a Thin Beam Immersed in a Viscous Fluid Near a Solid Surface,” *Physics of Fluids*, Vol. 17, 2005, 12 pages.

Green, C. P., and Sader, J. E., “Torsional Frequency Response of Cantilever Beams Immersed in Viscous Fluids with Applications to the Atomic Force Microscope,” *Journal of Applied Physics*, Vol. 92, No. 10, 2002, pp. 6262-6274.

Guillon, S., Saya, D., Mazenq, L., Perisanu, S., Vincent, P., Lazarus, A., Thomas, O., and Nicu, L., “Effect of Non-Ideal Clamping Shape on the Resonance Frequencies of Silicon Nanocantilevers,” *Nanotechnology*, Vol. 22, 2011, 9 pp.

Heinrich, S.M., Maharjan, R., Beardslee, L., Brand, O., Dufour, I., and Josse, F., "An Analytical Model for In-Plane Flexural Vibrations of Thin Cantilever-Based Sensors in Viscous Fluids: Applications to Chemical Sensing in Liquids," *Proceedings, International Workshop on Nanomechanical Cantilever Sensors,* Banff, Canada, May 26-28, 2010a, 2 pages.

Heinrich, S.M., Maharjan, R., Dufour, I., Josse, F., Beardslee, L.A., and Brand, O., "An Analytical Model of a Thermally Excited Microcantilever Vibrating Laterally in a Viscous Fluid," *Proceedings and Poster Session, IEEE Sensors 2010 Conference,* Waikoloa, Hawaii, November 1-4, 2010b, pp. 1399-1404.

Johnson, B.N., and Mutharasan, R., "Persistence of Bending and Torsional Modes in Piezoelectric-Excited Millimeter-Sized Cantilever (PEMC) Sensors in Viscous Liquids - 1 to 10^3 cP," *Journal of Applied Physics,* Vol. 109, 2011, 3 pages.

Justine, T. and Krishnan, A., "Effect of Support Flexibility on Fundamental Frequency of Beams," *Journal of* Sound and Vibration, Vol. 68(2), 1980, pp. 310-312.

Lange, D., Hagleitner, C., Hierlemann, A., Brand, O., and Baltes, H., "Complementary Metal Oxide Semiconductor Cantilever Arrays on a Single Chip: Mass-Sensitive Detection of Volatile Organic Compounds," *Analytical Chemistry*, Vol. 74, 2002, pp. 3084-3095.

Lavrik, N. V., Sepaniak, M. J., and Datskos, P. G., "Cantilever Transducers as a Platform for Chemical and Biological Sensors" *Review of Scientific Instruments*, Vol. 75, No. 7, July 2004, pp. 2229-2253.

Li, S., Orona, L., Li, Z., and Cheng, Z.-Y., "Biosensor Based on Magnetostrictive Microcantilever," *Applied Physics Letters*, Vol. 88, No. 073507, 2006, pp 1-3.

Lochon, F., Dufour, I., Rebière, D., Sampath, U., Heinrich, S.M., and Josse, F., "Effect of Viscoelasticity on Quality Factor of Microcantilever Chemical Sensors: Optimal Coating Thickness for Minimum Limit of Detection" *Proceedings of IEEE Sensors 2005,* 2005, pp. 265-268.

Maali, A., Hurth, C., Boisgard, R., Jai, C., Cohen-Bouhacina, T., and Aimé, J.P., "Hydrodynamics of Oscillating Atomic Force Microscopy Cantilevers in Viscous Fluids," *Journal of Applied Physics*, Vol. 97, 2005, 6 pages.

MacBain, J.C. and Genin, J., "Natural Frequencies of a Beam Considering Support Characteristics," *Journal of Sound and Vibration*, Vol. 27(2), 1973a, pp. 197-206.

MacBain, J.C. and Genin, J., "Effect of Support Flexibility on the Fundamental Frequency of Vibrating Beams," *Journal of the Franklin Institute,* Vol. 296, Issue 4, October 1973b, pp. 259-273.

MATLAB Version 7.10.0 (R2010a), Mathworks Inc., 2010.

Meirovitch, L., “Fundamentals of Vibrations,” Third Edition, McGraw Hill, 2001.

Narducci, M., Figueras, E., Lopez, M. J., Gracia, I., Fonseca, L., and Santander, J., “A High Sensitivity Silicon Microcantilever Based Mass Sensor” *Proceedings of IEEE Sensors 2008*, 2008, pp. 1127-1130.

O'Donnell, W.J., “The Additional Deflection of a Cantilever due to the Elasticity of the Support,” *Journal of Applied Mechanics*, Vol. 27, 1960, pp. 461-464.

Rinaldi, G., Packirisamy, M., and Stiharu, I., “Quantitative Boundary Support Charactersitization for Cantilever MEMS,” *Sensors*, Vol. 7, 2007, pp. 2062-2079.

Rogers, B., Manning, L., Jones, M., Sulchek, T., Murray, K., Beneschott, B., Adams, J.D., Hu, Z., Thundat, T., Cavazos, H., and Minne, S.C., “Mercury Vapor Detection with a Self-Sensing, Resonating Piezoelectric Cantilever,” *Review of Scientific Instruments*, Vol. 74, No. 11, 2003, pp. 4899-4901.

Sader, J., “Frequency Response of Cantilever Beams Immersed in Viscous Fluids with Applications to the Atomic Force Microscope,” *Journal of Applied Physics*, Vol 84, No 1, 1998, pp. 64-76.

Sampath, U., Heinrich, S.M., Josse, F., Lochon, F., Dufour, I., and Rebière, D., “Study of Viscoelastic Effect on the Frequency Shift of Microcantilever Chemical Sensors,” *IEEE Transactions on Ultrasonics, Ferroelectrics, and Frequency Control*, Vol. 53, No. 11, 2006, pp. 2166-2173.

Schaffer, T., Cleveland, J., Ohnsorge, F., Wlaters, D, and Hansma, P., “Studies of Vibrating Atomic Force Microscope Cantilevers in Liquid,” *Journal of Applied Physics*, Vol. 80, 7, 1996, pp. 3622-3627.

Schultz, J.A., Heinrich, S., Josse, F., Dufour, I., Nigro, N., Beardslee, L., and Brand, O., “Timoshenko Beam Model for Lateral Vibration of Liquid-Phase Microcantilever-Based Sensors,” *Proceedings, 14th International Symposium on MEMS and Nanotechnology, SEM 2013 Annual Conference & Exposition on Experimental and Applied Mechanics*, Lombard, IL, June 3-6, 2013a.

Schultz, J.A., Heinrich, S., Josse, F., Dufour, I., Nigro, N., Beardslee, L., and Brand, O., “Timoshenko Beam Effectsin Lateral-Mode Microcantilever-Based Sensors in Liquids,” *Proceedings, Nanomechanical Sensing Workshop*, Stanford University, Stanford, CA, 2013b.

Schultz, J.A., “Lateral-Mode Vibration of Microcantilever-Based Sensors in Viscous Fluids Using Timoshenko Beam Theory,” *Doctoral Dissertation*, December 2012, Marquette University, Wisconsin, USA.

Sharos, L. B., Raman, A., Crittenden, S., and Reifenberger, R., “Enhanced Mass Sensing using Torsional and Lateral Resonances in Microcantilevers” *Applied Physics Letters*, Vol. 84, No. 23, 2004, pp. 4638-4640.

Spletzer, M., Raman, A., Sumali, H., and Sullivan, J.P., “Highly Sensitive Mass Detection and Identification Using Vibration Localization in Coupled Microcantilever Arrays,” *Applied Physics Letters*, Vol. 92, 2008, 3 pages.

Spletzer, M., Raman, A., Wu, A.Q., and Xu, X., “Ultrasensitive Mass Sensing Using Mode Localization in Coupled Microcantilevers,” *Applied Physics Letters*, Vol. 88, 2006, 3 pages.

Stevens, K.K., “Deflcetion of Beams with Integral Elastic Support,” *Proceedings of the 11th Conference,* Fort Lauderdale, FL, May 19-22, 1996, pp. 343-346.

Stokes, G., “On the Effects of the Internal Friction of Fluids on the Motion of Pendulums,” *Transactions of the Cambridge Philosophical Society*, Vol. 9, 1851, pp 8-106.

Tamayo, J., Humphris, A. D. L., Malloy, A. M. and Miles, M. J., “Chemical Sensors and Biosensors in Liquid Environment Based on Microcantilevers with Amplified Quality Factor,” *Ultramicroscopy*, Vol. 86, 2001, pp. 167-173.

Tanno, K., Kawai, Y., and Ono, T., “Experimental and Modeling Analysis on Entrainment Condition of Submicrometer Thick Si Micro Mechanical Resonators with Nonlinear Coupling Element,” *Micro Electro Mechanical Systems (MEMS), 2012 IEEE 25th International Conference,* Jan. 29 2012-Feb. 2 2012, pp. 563 – 566.

Tedesco J.W., McDougal W.G., and Ross C.A, “Structural Dynamics: Theory and Applications”, First Edition, Addison Wesley Longman, 1999.

Tetin, S., Caillard, B., Menil, F., Debeda, H., Lucat, C., Pellet, C., and Dufour, I., "Modeling and performance of uncoated microcantilever-based chemical sensors", *Sensors and Actuators B*, 143, 2010, pp. 555-560.

Thundat, T., Wachter, E., Sharp, S., and Warmack, R., “Detection of Mercury Vapor Using Resonating Microcantilevers,” *Applied Physics Letters*, Vol. 66, No. 13, 1995, pp. 1695-1697.

Thundat, T., Warmack, R., Chen G., and Allison, D., “Thermal and Ambient-Induced Deflections of Scanning Force Microscope Cantilevers,” *Applied Physics Letters*, Vol. 64, No. 21, 1994, pp. 2894-2896.

Van Eysden, C and Sader, J., “Frequency Response of Cantilever Beams Immersed in Viscous Fluids with Applications to the Atomic Force Microscope: Arbitrary Mode Order,” *Journal of Applied Physics*, Vol. 101, 2007, 11 pages.

Vancura, C., Dufour, I., Heinrich, S., Josse, F., and Hierlemann, A., “Analysis of Resonating Microcantilevers Operating in a Viscous Liquid Environment,” *Sensors and Actuators A*, Vol. 141, No. 1, January 2008, pp. 43-51.

Vancura, C., Ruegg, M., Li, Y., Hagleitner, C., Hierlemann, A., “Magnetically Actuated Complementary Metal Oxide Semiconductor Resonant Cantilever Gas Sensor Systems,” *Analytical Chemistry*, Vol. 77, 2005, pp. 2690-2699.

Vancura, C., Ruegg, M., Li, Y., Lange, D., Hagleitner, C., Brand, O., Hierlemann, A., and Baltes, H., “Magnetically Actuated CMOS Resonant Cantilever Gas Sensor for Volatile Organic Compounds,” *Transducers '03, 12th International Conference on Solid- State Sensors, Actuators and Microsystems*, Vol. 2, 2003, pp. 1355-1358.

APPENDIX A
ADDED MASS AND DAMPING COEFFICIENT, DUE TO FLUID RESISTANCE, ON FINITELY WIDE PLATE VIBRATING FREELY IN VISCOUS FLUID

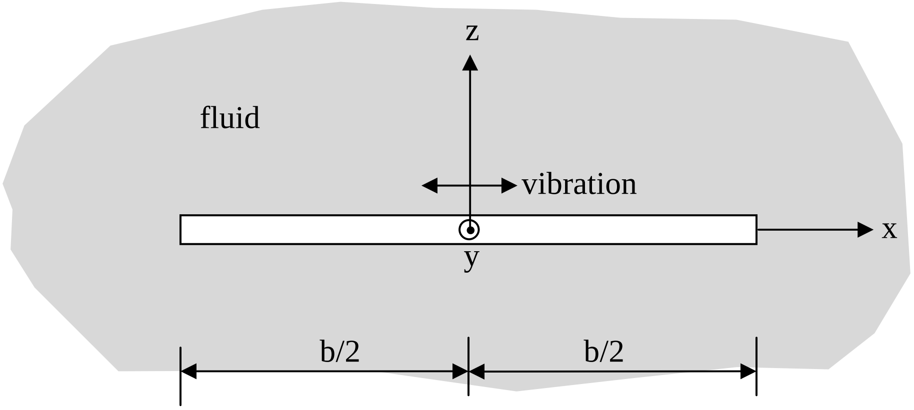

Figure A-1: Schematic of thin, infinitely long beam of finite width *b* oscillating along *x*-direction.

The plate with width *b* is vibrating along *x*-axis as shown in Fig. A-1. It will be assumed that the displacement of the fluid due to a beam of finite width is the same as that obtained with a beam of infinite width.

The Navier-Stokes equation for incompressible flow $\left(\nabla . \vec{u}_f = 0\right)$ is

$$\rho_f \frac{d\vec{u}_f}{dt} = -\nabla P + \eta \nabla^2 \vec{u}_f \frac{dy}{dx}, \tag{A-1}$$

where

$$\vec{u}_f = u_{x,f}\hat{i} + u_{y,f}\hat{j} + u_{z,f}\hat{k} \tag{A-2}$$

is the velocity field of the fluid at all points, *P* is the pressure, and ρ_f and η are the density and dynamic viscosity of the fluid, respectively. Equation (A-1) can be written as

$$\rho_f \frac{d}{dt}\left(u_{x,f}\hat{i} + u_{y,f}\hat{j} + u_{z,f}\hat{k}\right) = -\left(\frac{\partial P}{\partial x}\hat{i} + \frac{\partial P}{\partial y}\hat{j} + \frac{\partial P}{\partial z}\hat{k}\right) + \eta\left[\left(\nabla^2 u_{x,f}\right)\hat{i} + \left(\nabla^2 u_{y,f}\right)\hat{j} + \left(\nabla^2 u_{z,f}\right)\hat{k}\right]. \tag{A-3}$$

Comparing the same unit vectors in left hand side and right hand side, Eq. (A-3) can be written into following three different equations:

$$\rho_f \frac{du_{x,f}}{dt} = -\frac{\partial P}{\partial x} + \eta \left(\frac{\partial^2 u_{x,f}}{\partial x^2} + \frac{\partial^2 u_{x,f}}{\partial y^2} + \frac{\partial^2 u_{x,f}}{\partial z^2} \right) \quad , \qquad \text{(A-4a)}$$

$$\rho_f \frac{du_{y,f}}{dt} = -\frac{\partial P}{\partial y} + \eta \left(\frac{\partial^2 u_{y,f}}{\partial x^2} + \frac{\partial^2 u_{y,f}}{\partial y^2} + \frac{\partial^2 u_{y,f}}{\partial z^2} \right) , \qquad \text{(A-4b)}$$

$$\rho_f \frac{du_{z,f}}{dt} = -\frac{\partial P}{\partial z} + \eta \left(\frac{\partial^2 u_{z,f}}{\partial x^2} + \frac{\partial^2 u_{z,f}}{\partial y^2} + \frac{\partial^2 u_{z,f}}{\partial z^2} \right) \quad . \qquad \text{(A4-c)}$$

The Boundary Conditions

Let the plate is vibrating in *x*-direction with velocity

$$u_{x,plate} = U_0 e^{i\Omega t} = U_0 e^{-dt} e^{i\omega t} , \qquad \text{(A-5)}$$

where, U_0 is the amplitude of plate excitation velocity in *x*-direction, $\Omega = \omega + id$ is the complex frequency with real part ω and imaginary part *d*. At surface of plate, *z* = 0, the boundary conditions are:

$$u_{x,f}(z=0) = u_{x,plate} = U_0 e^{-dt} e^{i\omega t} , \qquad \text{(A-6a)}$$

$$u_{y,f}(z=0) = 0 \quad , \qquad \text{(A-6b)}$$

$$u_{z,f}(z=0) = 0 \quad . \qquad \text{(A-6c)}$$

It has been assumed that fluid in contact with the plate will have the same velocity as the plate because of nonslip condition. At $z \to \infty$, the boundary conditions are:

$$u_{x,f}(z \to \infty) = u_{y,f}(z \to \infty) = u_{z,f}(z \to \infty) = 0 , \qquad \text{(A-6d)}$$

$$P(z \to \infty) = P_0 \ . \qquad \text{(A-6e)}$$

Assume that the velocity of fluid and pressure are independent of *x* and y direction. Then,

$$u_{x,f} = u_{x,f}(z,t),$$
$$u_{y,f} = u_{z,f} = 0, \qquad \text{(A-7a-c)}$$
$$P = P(z,t).$$

Using Eqs. (A-7a-c) in Eq. (A-4a-c) gives

$$\rho_f \frac{du_{x,f}(z,t)}{dt} = \eta \frac{\partial^2 u_{x,f}(z,t)}{\partial x^2}, \qquad \text{(A-8a)}$$

$$0 = 0 \quad , \qquad \text{(A-8b)}$$

$$\begin{array}{l} \dfrac{\partial P(z,t)}{\partial z} = 0 \Rightarrow P(z,t) = P(t) \\ \qquad\qquad P(\infty,t) = P(t) = P_0 \end{array} \quad , \qquad \text{(A-8c)}$$

where P_0 is the atmospheric pressure.

Solution for $u_{x,f}$

$$u_{x,f}(z,t) = f(z)\, e^{i\Omega t} = f(z)\, e^{-d\,t} e^{i\,\omega t} \qquad \text{(A-9)}$$

Substituting Eq. (A-9) in to Eq.(A-8a) results in

$$\frac{\partial^2 f(z)}{\partial z^2} - a^2 f(z) = 0 \quad , \qquad \text{(A-10)}$$

with

$$a = \sqrt{(i\omega - d)\frac{\rho_f}{\eta}}\ , \qquad \text{(A-11)}$$

where a is the square root of $(i\omega - d)\dfrac{\rho_f}{\eta}$ with positive real part.

The general solution of Eq. (A-10) is:

$$f(z) = C_1 e^{a z} + C_2 e^{-a z} \quad . \tag{A-12}$$

Now the boundary conditions are:

$$\begin{aligned} f(0) &= U_0 \ , \\ f(\infty) &= 0 \ . \end{aligned} \tag{A-13a-b}$$

Substituting Eq. (A-13a,b) in to Eq. (A-12) gives $C_1 = 0$ and $C_2 = U_0$.

Therefore, Eq. (A-12) reduces to

$$f(z) = U_0 e^{-a z} \ . \tag{A-14}$$

Substituting Eq. (A-14) in to Eq. (A-9) results in

$$u_{x,f}(z,t) = U_0 e^{-a z} \ e^{-d t} \ e^{i \omega t} \quad . \tag{A-15}$$

Substituting Eq. (A-11) in to Eq. (A-15) gives

$$u_{x,f}(z,t) = U_0 e^{-\sqrt{i(\omega + id)\frac{\rho_f}{\eta}} \ z} \ e^{-d t} \ e^{i \omega t} . \tag{A-16}$$

Using $\sqrt{i} = \frac{1+i}{\sqrt{2}}$ in Eq. (A-16) gives

$$u_{x,f}(z,t) = U_0 \ e^{-d t} \ e^{i \omega t} \ e^{-\sqrt{(\omega + id)\frac{\rho_f}{2\eta}} \ (1+i) z} \quad . \tag{A-17}$$

Shear stress at the surface of plate

Shear stress at a distance *z* from plate is

$$\tau(z) = \eta \frac{du_{x,t}(z,t)}{dz} = -\eta \, U_0 \ e^{-d t} \ e^{i \omega t} \sqrt{(\omega + id)\frac{\rho_f}{2\eta}} \ (1+i) \ e^{-\sqrt{(\omega+id)\frac{\rho_f}{2\eta}} \ (1+i) z} \quad . \tag{A-18}$$

At *z*=0, i.e., shear stress on the surface of the plate is

$$\tau_0 = \tau(0) = -\eta \, U_0 \ e^{-d t} \ e^{i \omega t} \sqrt{(\omega + id)\frac{\rho_f}{2\eta}} \ (1+i) \quad . \tag{A-19}$$

Shear force acting on the surface of the plate

Shear force per unit length acting on plate can be obtained by integrating shear stress over the width of plate as

$$F_s(t) = 2\int_{-b/2}^{b/2} \tau_0 dx = -U_0\, e^{-d\,t}\, e^{i\,\omega\,t} \sqrt{2\eta\rho_f b^2(\omega + id)}\,(1+i)\ . \tag{A-20}$$

Using $\sqrt{i} = \dfrac{1+i}{\sqrt{2}}$ in Eq. (A-20) gives

$$F_s(t) = -2U_0 e^{-d\,t}\, e^{i\,\omega\,t} \sqrt{\eta\rho_f b^2}\,\sqrt{(i\omega - d)}\,. \tag{A-21}$$

Let $\sqrt{i\omega - d} = p + iq$, then,

$$p = \frac{1}{\sqrt{2}}\sqrt{\sqrt{(-d)^2 + \omega^2} + (-d)} = \frac{1}{\sqrt{2}}\sqrt{\sqrt{d^2 + \omega^2} - d}\quad , \tag{A-22a}$$

$$q = \frac{1}{\sqrt{2}}\sqrt{\sqrt{(-d)^2 + \omega^2} - (-d)} = \frac{1}{\sqrt{2}}\sqrt{\sqrt{d^2 + \omega^2} + d}\quad . \tag{A-22b}$$

Therefore, Eq. (A-21) becomes

$$F_s(t) = \left(-\sqrt{2}\,U_0\ \sqrt{\eta\rho_f b^2}\ \sqrt{\sqrt{d^2+\omega^2} - d} - i\sqrt{2}\,U_0\ \sqrt{\eta\rho_f b^2}\sqrt{\sqrt{d^2+\omega^2} + d}\right) e^{-d\,t}\, e^{i\,\omega\,t}. \tag{A-23}$$

This shear force can also be written as

$$F_s(t) = -\overline{m}_f\, \frac{du_{x,f}(0,t)}{dt} - \overline{c}_f u_{x,f}(0,t)\,. \tag{A-24}$$

Substituting Eq. (A-17) in to Eq. (A-24) results in

$$F_s(t) = \left[U_0\left(d\overline{m}_f - \overline{c}_f\right) - i\,U_0\omega\overline{m}_f\right] e^{-d\,t}\, e^{i\,\omega\,t}\,. \tag{A-25}$$

Here $\overline{m}_f$ and $\overline{c}_f$ are real.

Comparing Eq. (23) and Eq. (24) results in

$$\bar{m}_f = \frac{\sqrt{2\eta\rho_f b^2}}{\sqrt{\omega}} \sqrt{\sqrt{\frac{d^2}{\omega^2}+1}+\frac{d}{\omega}}\,, \tag{A-26a}$$

$$\bar{c}_f = \sqrt{2\eta\rho_f b^2}\sqrt{\omega}\left(\frac{d}{\omega}\sqrt{\sqrt{\frac{d^2}{\omega^2}+1}+\frac{d}{\omega}}+\sqrt{\sqrt{\frac{d^2}{\omega^2}+1}-\frac{d}{\omega}}\right). \tag{A-26b}$$

Eqs. (A-26a, b) are the exact results for added mass and added damping coefficient for infinitely wide plate vibrating under harmonically decaying excitation on viscous fluid. If there is no decaying of oscillation, then *d*=0 and Eqs. (A-26a, b) reduce to

$$\bar{m}_f = \frac{\sqrt{2\eta\rho_f b^2}}{\sqrt{\omega}}\,, \tag{A-27a}$$

$$\bar{c}_f = \sqrt{2\eta\rho_f b^2}\sqrt{\omega}\,. \tag{A-27b}$$

APPENDIX B
DIMENSIONAL ANALYSIS TO OBTAIN THE POSSIBLE DIMENSIONLESS RELATIONSHIPS BETWEEN ROTATIONAL SUPPORT STIFFNESS AND THE PROBLEM PARAMETERS

The dimensional analysis is performed using Buckingham Pi Theorem [e.g., Fox and McDonald, 1993]. The theorem states that if there are *n* parameters in a problem and these parameters contain *m* primary dimensions (for example *F*, *L*, *T*) the equation relating all the variables will have (*n*-*m*) independent dimensionless ratios (Π parameters), expressible in functional form as

$$\begin{aligned} & f\left(\Pi_1,\Pi_2,........,\Pi_{n-m}\right)=0 \\ & \text{or} \\ & \Pi_1=f_1\left(\Pi_2,\Pi_3,........,\Pi_{n-m}\right)=0 \end{aligned} \quad . \qquad \text{(B-1)}$$

The rotational stiffness of support k can be assumed to be the function of material properties *E*, ν and beam cross-sectional dimension *b*, *h* and can be written in the form of Eq. (B-1) as

$$k=f\left(E,b,h,\nu\right). \qquad \text{(B-2)}$$

There are five problem parameters involved $k, E, b, h,$ and ν .Therefore, *m* is 5. If *F*, *L*, *T* are primary dimensions for force, length and time, the dimensions of each parameter are

$$k=FL \ , \quad E=F/L^2 \ , \quad b=L \ , \quad h=L \ , \quad \nu=1 . \qquad \text{(B-3)}$$

Therefore, the number of primary dimensions *m* is 2. So the number of dimensionless groups (Πparameters) is 3 (*n*-*m*=5-2=3). Parameters *E* and *b* are chosen as repeating parameters. Now setting up dimensional equations

$$\Pi_1=E^a b^b k=\left(\frac{F}{L^2}\right)^a (L)^b (FL)=F^0L^0T^0 \ , \qquad \text{(B-4a)}$$

$$\Pi_2 = E^c b^d h = \left(\frac{F}{L^2}\right)^c (L)^d (L) = F^0 L^0 T^0 \,, \tag{B-4b}$$

$$\Pi_3 = E^e b^f \nu = \left(\frac{F}{L^2}\right)^e (L)^f (1) = F^0 L^0 T^0 \,, \tag{B-4c}$$

and equating the exponents of *F*, *L* , and *T* in Eqs. (B-4a-c) results in *a*=-1, *b*=-3, *c*=0, *d*=-1, *e*=0, and *f*=0. Therefore, the Pi functions become

$$\Pi_1 = \frac{k}{Eb^3} \,, \tag{B-5a}$$

$$\Pi_2 = \frac{h}{b} \,, \tag{B-5b}$$

$$\Pi_3 = \nu \,. \tag{B-5c}$$

Now the functional relationship in Eq. (B-1) becomes

$$\frac{k}{Eb^3} = f_1\left(\frac{h}{b}, \nu\right). \tag{B-6a}$$

But the Π parameters are not unique, so the functional relationship could also have following forms:

$$\frac{k}{Eh^3} = f_2\left(\frac{h}{b}, \nu\right); \tag{B-6b}$$

$$\frac{k}{Ehb^2} = f_3\left(\frac{h}{b}, \nu\right); \tag{B-6c}$$

$$\frac{k}{Eh^2 b} = f_4\left(\frac{h}{b}, \nu\right). \tag{B-6d}$$

APPENDIX C
DETERMINATION OF EFFECTIVE MODULUS OF ELASTICITY

The effective Young's modulus $E_{eff.}$ is determined by fitting the in-vacuum results for perfectly fixed case to in-air experimental data based on least squared error method. Recall that the in-vacuum natural frequency is given by Eq. (3-13) as

$$\omega_0 = \lambda_1^{\ 2} \frac{b}{L^2} \sqrt{\frac{E_{eff.}}{12\rho_b}} \ . \qquad \text{(C-1)}$$

Converting the circular frequency in radians to natural frequency in Hz results in

$$f_0 = \frac{\omega_0}{2\pi} = \frac{\lambda_1^{\ 2}}{2\pi} \frac{b}{L^2} \sqrt{\frac{E_{eff.}}{12\rho_b}} \ . \qquad \text{(C-2)}$$

If f_{air} is the experimental frequency data in air then the sum of squared error *e* between the this frequency and in-vacuum frequency is

$$e = \sum_i^N \left(f_{air,i} - f_{0,i} \right)^2 , \qquad \text{(C-3)}$$

where

N = number of data point,

i = 1, 2, 3,….,N .

Substituting Eq. (C-2) into Eq. (C-3) results in

$$e = \sum_i^N \left(f_{air,i} - \frac{\lambda_1^{\ 2}}{2\pi} \frac{b_i}{L_i^{\ 2}} \sqrt{\frac{1}{12\rho_b}} \sqrt{E_{eff.}} \right)^2 . \qquad \text{(C-4)}$$

The minimization of the total squared error requires that the derivative of *e* with respect to $E_{eff.}$ be zero, i.e.,

$$\frac{de}{dE_{eff.}} = 0 \, . \qquad \text{(C-5)}$$

Substituting Eq. (C-4) into Eq. (C-5) results in

$$\frac{d\sum_{i}^{N}\left(f_{air,i}-\frac{\lambda_1^{2}}{2\pi}\frac{b_i}{L_i^{2}}\sqrt{\frac{1}{12\rho_b}}\sqrt{E_{eff.}}\right)^{2}}{dE_{eff.}}=0\,. \tag{C-6}$$

Differentiating and simplifying Eq. (C-6) gives

$$\sum\nolimits_{i}^{N}\left(f_{air,i}\,\frac{b_i}{L_i^{2}}\right)\frac{1}{\sqrt{E_{eff.}}}-\frac{\lambda_1^{2}}{2\pi}\sqrt{\frac{1}{12\rho_b}}\sum_{i}^{N}\left(\frac{b_i}{L_i^{2}}\right)^{2}=0\,, \tag{C-7}$$

$$E_{eff.}=\left[\frac{\sum\nolimits_{i}^{N}\left(f_{air,i}\,\frac{b_i}{L_i^{2}}\right)}{\frac{\lambda_1^{2}}{2\pi}\sqrt{\frac{1}{12\rho_b}}\sum_{i}^{N}\left(\frac{b_i}{L_i^{2}}\right)^{2}}\right]^{2} \tag{C-8}$$

Equation (C-8) is used to determine the effective modulus of elasticity of a composite microcantilever. Only *L*= (800, 1000) µm experimental data set are used since for these lengths the support compliance effects and Timoshenko beam effects are negligible.

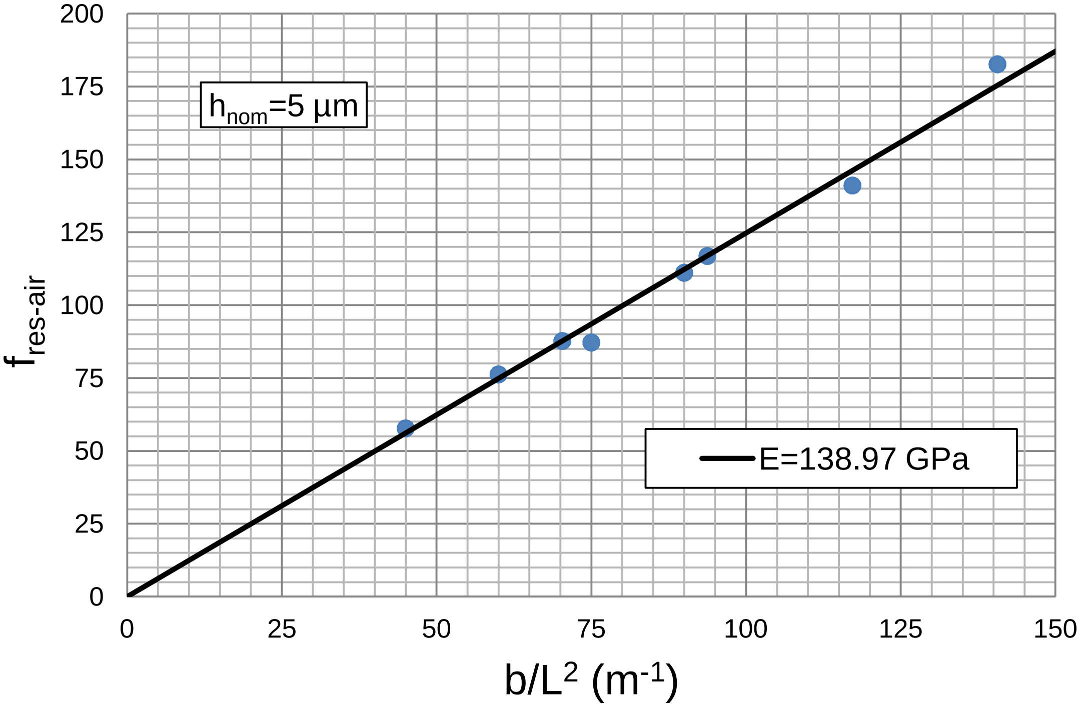

h_{nom}=5 µm
E=138.97 GPa
$f_{res\text{-}air}$
b/L^2 (m^{-1})
0
25
50
75
100
125
150
175
200
0
25
50
75
100
125
150

(a)

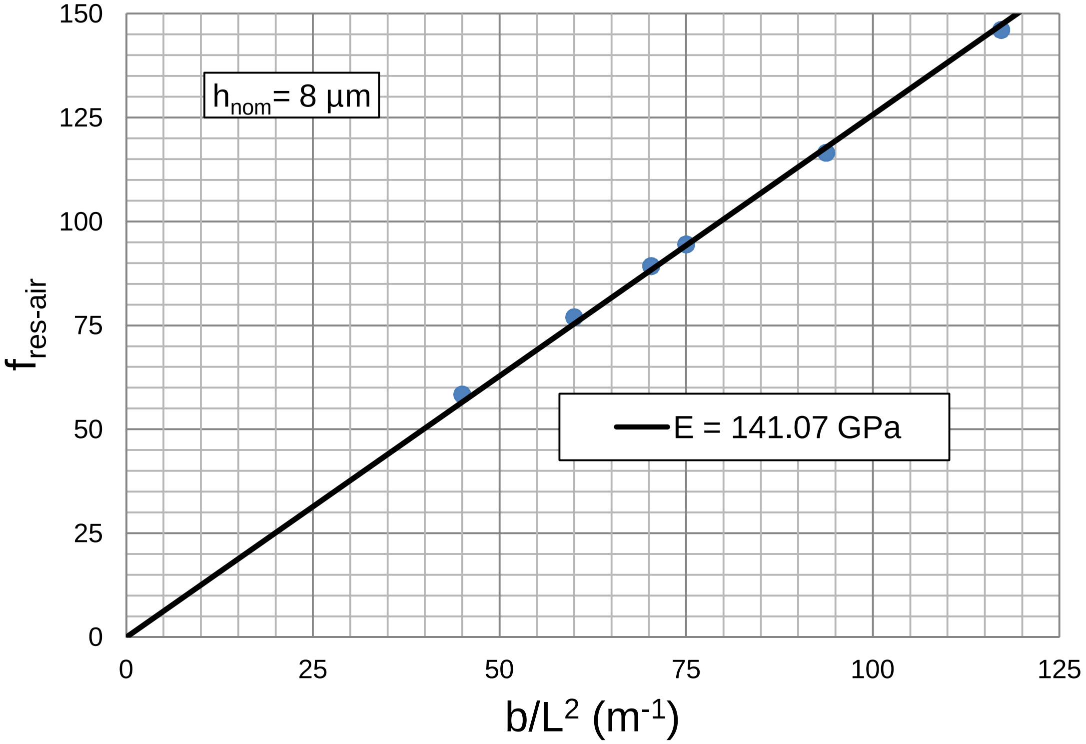

h_{nom}= 8 µm
E = 141.07 GPa
$f_{res\text{-}air}$
b/L^2 (m^{-1})
0
25
50
75
100
125
150
0
25
50
75
100
125

(b)

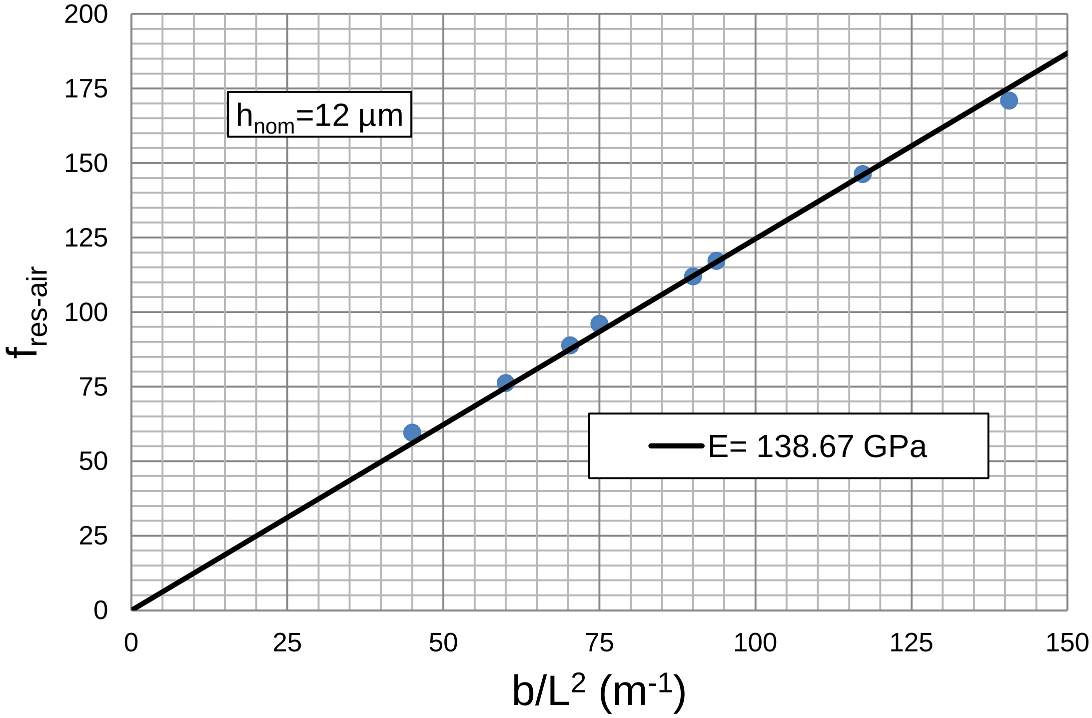

(c)

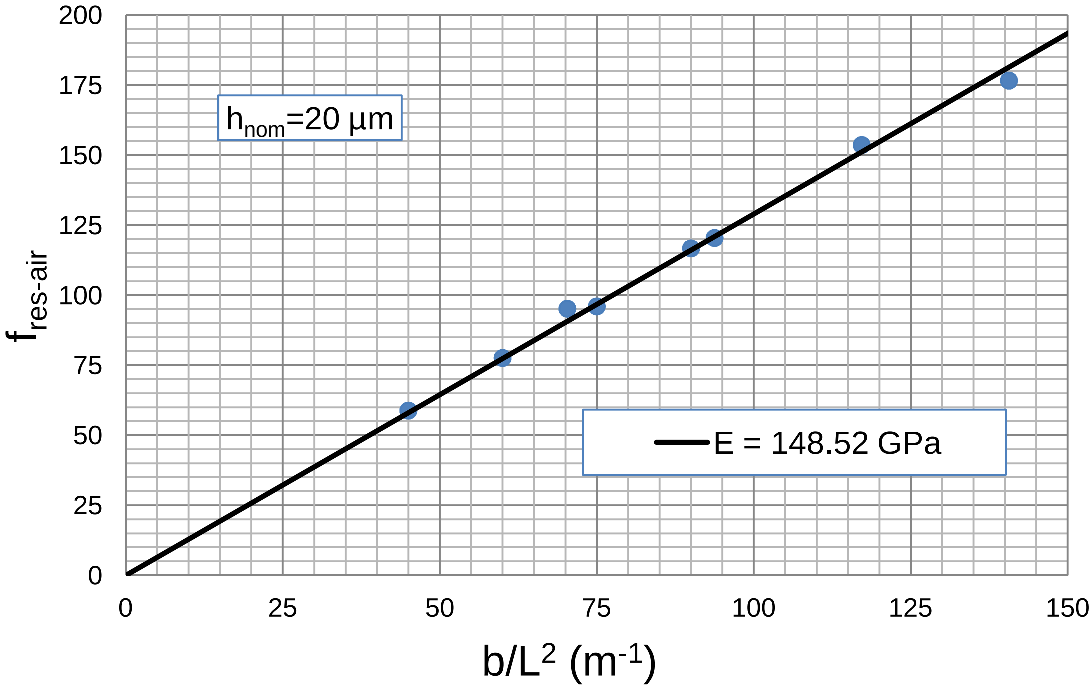

(d)

Figure C-1: Best curve fit of experimental fundamental lateral frequency data in air for L= (800, 1000) μm: (a) h_{nom}= 5 μm, (b) h_{nom}= 8 μm, (c) h_{nom}= 12 μm, (d) h_{nom}= 20 μm.

APPENDIX D
MATLAB CODES USING BVP4C SOLVER

Free Vibration

```
%This program provides the solution for eigenvalue problem of cantileverbeam with
%elastic support in fluid

function bvp4free
%Specify nodes of the mesh and initial guess for the solution
solinit = bvpinit(linspace(0,1,10000),[1 0 0 0]);
%Solution using bvp4c
sol = bvp4c(@bvp4ode,@bvp4bc,solinit);
x = linspace(0,1);
y = deval(sol,x);
ymax=max(abs(y(1,:)));
ybar=(y(1,:)/ymax);
plot(x,ybar,'-r','LineWidth',2.5);
xlabel('\xi')
ylabel('\phi_{bar}(\xi)')

%Differential Equation Definition and Evaluation
function dxdy = bvp4ode(x,y)

%calculation of eigenvalue(root for alpha from characteristic equation)
% specify 1/kbar value
K=0.15;                    %%% K=1/kbar

%specify range of alpha based on mode to be solved
%calculate root of alpha for first mode
alphamin=0;
alphamax=2;
nalphainc=101;
alpha=linspace(alphamin,alphamax,nalphainc);
% Now  insert "for loop" here to calculate f at all alpha values.
for jalpha=1:nalphainc;
    ALPHA=alpha(jalpha);
    f(jalpha)=1+cosh(ALPHA)*cos(ALPHA)-
(K*ALPHA*((cosh(ALPHA)*sin(ALPHA))-(sinh(ALPHA)*cos(ALPHA))));
    fFixed(jalpha)=(1+cosh(ALPHA)*cos(ALPHA));
end;
%Next find the root for alpha.
for jalpha=1:nalphainc
     if (jalpha==1);
        continue
```

```
        else
% Now we will will omit the roots for perfectly fixed cantilever.
            if (f(jalpha)*f(jalpha-1)<=0);
%   If a sign change has occurred, determine which alpha value corresponds to the f value
%   that is closer to zero.
                fmagprevious=abs(f(jalpha-1));
                fmagcurrent=abs(f(jalpha));
                fmaglocal=[fmagcurrent fmagprevious];
                [fmagmin,Iminlocal]=min(fmaglocal);
%   Note that if Iminlocal equals 1, then the index for alpharoot is jalpha; if Iminlocal is
%   2, then the index for alpharoot is jalpha-1. So, in general, the index for alpharoot may
%   be written as jalpha+1-Iminlocal.
                 alpharoot=alpha(jalpha+1-Iminlocal);
            end
        end
end
dxdy=[y(2) y(3) y(4) alpharoot^4*y(1)];

% Boundary Condition
function res = bvp4bc(ya,yb)
K=0.15;                              %%%% K=1/k_bar
res=[ya(1) ya(2)-ya(3)*K yb(3) yb(4)];
```

Forced Vibration

```
%This program provides the solution for boundary value problem of cantileverbeam with
%elastic support in fluid excited via relative harmonic rotation near support

function bvp4forced
% Specify nodes of the mesh and initial guess for the solution
solinit = bvpinit(linspace(0,1,10000),[1 0 0 0]);
%Solution using bvp4c
sol = bvp4c(@bvp4ode,@bvp4bc,solinit);
x = linspace(0,1);
y = deval(sol,x);
figure(1)
plot(x,real(y(1,:)),'--b','LineWidth',2.5);
xlabel('\xi')
ylabel('Re[\phi(\xi)]/\theta_0')

figure(2)
plot(x,imag(y(1,:)),'--b','LineWidth',2.5);
xlabel('\xi')
ylabel('Im[\phi(\xi)]/\theta_0')
 %Differential Equation Definition and Evaluation
function dxdy = bvp4ode(x,y)
```

```
%Specify known parameters
zeta=0.2;        % fluid resistance parameter
omegabar=0.75;   % omegabar near first resonance
lambda1=1.875104;
alpha=(lambda1^4*(1+(zeta/(lambda1*sqrt(omegabar))))*omegabar^2-
1i*lambda1^3*zeta*omegabar^1.5)^0.25;
dxdy=[y(2) y(3) y(4) alpha^4*y(1)];

% Boundary Condition
function res = bvp4bc(ya,yb)
K=0.15;                          %%%% K=1/k_bar is support compliance
res=[ya(1) ya(2)-ya(3)*K-1 yb(3) yb(4)];
```